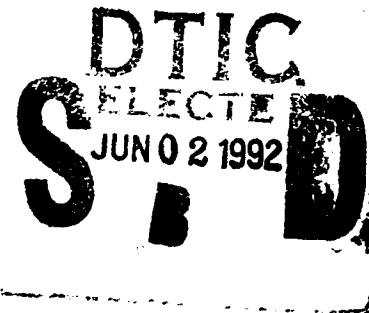AD-A251 258

‖‖‖‖‖‖‖‖‖‖‖‖‖‖‖‖‖‖‖‖‖‖‖

WL-TR-91-2061

EFFECT OF INTERFACIAL FORCES ON EVAPORATIVE
HEAT TRANSFER IN A MENISCUS

Peter C. Wayner, Jr.
Sunando DasGupta
Jeffrey A. Schonberg

Rensselaer Polytechnic Institute
The Isermann Department of Chemical Engineering
Troy, New York   12180-3590

September 1991

DTIC
ELECTE
JUN 0 2 1992
S   B   D

Final Report for Period Apr 88 - Jul 91

AERO PROPULSION AND POWER DIRECTORATE
WRIGHT LABORATORY
AIR FORCE SYSTEMS COMMAND
WRIGHT-PATTERSON AIR FORCE BASE, OHIO   45433-6563

92-14392

‖‖‖‖‖‖‖‖‖‖‖‖‖‖‖‖‖‖‖‖‖

92 6 01   061

NOTICE

When Government drawings, specifications, or other data are used for any purpose other than in connection with a definitely Government-related procurement, the United States Government incurs no responsibility or any obligation whatsoever. The fact that the government may have formulated or in any way supplied the said drawings, specifications, or other data, is not to be regarded by implication, or otherwise in any manner construed, as licensing the holder, or any other person or corporation; or as conveying any rights or permission to manufacture, use, or sell any patented invention that may in any way be related thereto.

This report is releasable to the National Technical Information Service (NTIS). At NTIS, it will be available to the general public, including foreign nations.
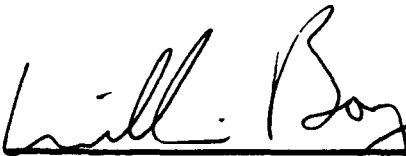
This technical report has been reviewed and is approved for publication.

WON S. CHANG
Project Engineer

JERRY E. BEAM, TAM
Power Technology Branch
Aerospace Power Division
Aero Propulsion and Power Laboratory

WILLIAM U. BORGER
Chief, Aerospace Power Division
Aero Propulsion & Power Laboratory

If your address has changed, if you wish to be removed from our mailing list, or if the addressee is no longer employed by your organization please notify WL/POOS-3, WPAFB, OH 45433-6563 to help us maintain a current mailing list.

Copies of this report should not be returned unless return is required by security considerations, contractual obligations, or notice on a specific document.

REPORT DOCUMENTATION PAGE

Form Approved
OMB No. 0704-0188

1a. REPORT SECURITY CLASSIFICATION	1b. RESTRICTIVE MARKINGS
Unclassified	

2a. SECURITY CLASSIFICATION AUTHORITY	3. DISTRIBUTION / AVAILABILITY OF REPORT
	Approved for public release; distribution is unlimited.
2b. DECLASSIFICATION / DOWNGRADING SCHEDULE	

4. PERFORMING ORGANIZATION REPORT NUMBER(S)	5. MONITORING ORGANIZATION REPORT NUMBER(S)
RPI-CHE/PCW-91-01	WL-TR-91-2061

6a. NAME OF PERFORMING ORGANIZATION	6b. OFFICE SYMBOL (If applicable)	7a. NAME OF MONITORING ORGANIZATION
Rensselaer Polytechnic Institute		Aero-Propulsion Power Directorate (WL/POOS) Wright Laboratory

6c. ADDRESS (City, State, and ZIP Code)	7b. ADDRESS (City, State, and ZIP Code)
Department of Chemical Engineering Troy, NY 12180-3590	Wright-Patterson AFB, OH 45433-6563

8a. NAME OF FUNDING / SPONSORING ORGANIZATION	8b. OFFICE SYMBOL (If applicable)	9. PROCUREMENT INSTRUMENT IDENTIFICATION NUMBER
		F33615-88-C-2821

8c. ADDRESS (City, State, and ZIP Code)	10. SOURCE OF FUNDING NUMBERS			
	PROGRAM ELEMENT. NO.	PROJECT NO.	TASK NO.	WORK UNIT ACCESSION NO.
	63221C	0581	20	11

11. TITLE (Include Security Classification)

EFFECT OF INTERFACIAL FORCES ON EVAPORATIVE HEAT TRANSFER IN A MENISCUS

12. PERSONAL AUTHOR(S)

Wayner, Peter C., Jr., DasGupta, Sunando and Schonberg, Jeffrey

13a. TYPE OF REPORT	13b. TIME COVERED	14. DATE OF REPORT (Year, Month, Day)	15. PAGE COUNT
Final	FROM 88 April TO 91 July	1991, September 27	152

16. SUPPLEMENTARY NOTATION

17. COSATI CODES			18. SUBJECT TERMS (Continue on reverse if necessary and identify by block number)
FIELD	GROUP	SUB-GROUP	Capillary pressure, evaporation, disjoining pressure, heat transfer, thin liquid film, interfacial phenomena, heat pipe, meniscus, image processing, interferometry

19. ABSTRACT (Continue on reverse if necessary and identify by block number)

A circular capillary fed heat transfer cell was used to study fluid flow and change-of-phase heat transfer in the contact line region of an evaporating meniscus. Using ellipsometry and microcomputer enhanced video microscopy (based on interferometry), the film thickness profile was measured as a function of the evaporation rate for polar and nonpolar fluids. This profile gives the pressure field. The experimental results confirmed a theoretical model that included the effects of capillarity, disjoining pressure, and conduction on fluid flow and evaporation. The combined results demonstrated that there are significant resistances to heat transfer in a small meniscus due to interfacial forces, viscous stresses and conduction. Therefore, the ideal evaporative heat flux based on kinetic theory cannot be obtained in an evaporating meniscus.

20. DISTRIBUTION / AVAILABILITY OF ABSTRACT	21. ABSTRACT SECURITY CLASSIFICATION
☒ UNCLASSIFIED/UNLIMITED ☐ SAME AS RPT. ☒ DTIC USERS	Unclassified

22a. NAME OF RESPONSIBLE INDIVIDUAL	22b. TELEPHONE (Include Area Code)	22c. OFFICE SYMBOL
Dr. Won S. Chang	513-255-2922	WL/POOS

DD Form 1473, JUN 86   *Previous editions are obsolete.*   SECURITY CLASSIFICATION OF THIS PAGE

PREFACE

Accession For

NTIS CRA&I	☑	
DTIC TAB	☐	
Unannounced	☐	
Justification		

By

Distribution/

Availability Codes

Dist	Avail and/or Special
A-1	

TABLE OF CONTENTS

vi

LIST OF FIGURES

vii

LIST OF TABLES

SYMBOLS AND ABBREVIATIONS

A $= 6\pi\bar{A}$ Hamaker constant, area

a coefficient defined by Eq. (4.6)

b coefficient defined by Eq.(4.7)

B modified Hamaker constant

C_l evaporation coefficient (equal to 2)

d reference thickness defined in Figure (1), pore diameter

E energy per unit surface energy (see Eq. A.5)

F potential energy per unit volume due to intermolecular forces

g gravitational acceleration

Δh_m heat of vaporization per unit mass,

Δh heat of vaporizatioin per unit volume

K curvature (see Eq. 2.3)

K' curvature gradient

k thermal conductivity of the liquid film

l characteristic length (see Eq. 4.18)

$\dot{m}$ evaporative mass flux

$\dot{m}^{id}$ $= a \, (T_s - T_v)$, ideal evaporative mass flux

M molecular weight

$\dot{M}$ dimensionless interfacial heat or mass flux (see Eq. 1.4)

P_v reference vapor pressure

P_l liquid pressure

P_{lv} vapor pressure at liquid-vapor interface

Q   Power input setting; also, integral heat sink defined by Eq. B.6

Q_δ integral evaporative heat sink for the region where the thickness is less than δ (see Eq. 1.1)

Q_T experimentally measured integral evaporative heat sink for the toatal meniscus based on liquid flow rate (see Eq. 3.4)

Q_{ev} experimentally measured integral evaporative heat sink for the total meniscus based on the temperature profiles (see Eq. 3.3)

Q^* dimensionless integral heat sink based on disjoining pressure only (see Eq. B7)

$\bar{Q}$ dimensionless integral heat sink including disjoining pressure and capillarity (see Eq. 1.2)

R   universal gas constant; radial distance

s   thickness of silicon substrate

t   time

ΔT characteristic temperature difference between solid and vapor, (see Eq. 4.12)

T_{lv} temperature of the liquid-vapor interface

T_s substrate temperature, which is taken to be constant in Section 4

T_v temperature of the vapor, which is taken to be a constant

u   velocity in the "x" direction

V_l molar volume of the liquid

W   a mathematical convenience (see Eq. B.4)

x   coordinate distance along the solid substrate

β See Eq. 4.32

Γ theoretical mass flow rate (see Eq. 2.5)

Γ_r measured macroscopic liquid input rate

δ_o reference film thickness (see Eq. 4.15)

δ thickness of the liquid film

Δ difference

ε dimensionless parameter (see Eq. 4.24)

η dimensionless film thickness, δ/δ_o

Θ angle of inclination, apparent contact angle

κ dimensionless parameter (see Eq. 4.23)

λ dimensionless length (see Eq. 4.29)

ν kinematic viscosity

ξ dimensionless distance (see Eq. 4.19)

Π disjoining pressure (see Eq. 2.4)

Π_o characteristic pressure (see Eq. 4.16)

ρ density

σ surface tension

ϕ dimensionless pressure difference, $(P_l - P_v)/\Pi_o$, (see Eq. 4.17)

subscripts

e   effective

l liquid

lv   liquid-vapor

m   meniscus

s   solid

v   vapor

superscripts

id   ideal, based on kinetic theory

'   derivative

SECTION 1

SUMMARY

The long-range objectives of this research program are to identify, evaluate, and correlate important characteristics of the heat transfer process in evaporating thin liquid films that can be subsequently used to optimize their performance as heat sinks. Herein, a thin liquid film in the shape of a meniscus is emphasized. In the macroscopic experimental part of the study, a relatively large extended meniscus was studied at low evaporation rates. However, we believe that the characteristics obtained for low evaporation rates and relatively large systems should also represent the phenomena in smaller systems with higher evaporation rates. In the microscopic experimental and theoretical part of the study, the contact line region of the meniscus, which is a small (in general, thickness less than the order of 5 μ) but critical part of the extended meniscus, was studied. As the meniscus decreases in size, the contact line region would represent a larger portion of the total heat sink. In the latter case, the stability of the system would increase because of the closer proximity of the solid surface which (along with the liquid properties) passively controls the shape of the meniscus. Therefore, the experimental approach is to study the characteristics of the evaporating meniscus in a sufficiently large system that allows the measurements and subsequent modeling of the results. Using the kinetic theory ideal interfacial heat flux as a reference, the relative effects of temperature, pressure, and conduction on the interfacial heat flux are determined. Having obtained an experimental confirmation of the modeling, the model can then be used to predict the performance of smaller size but higher flux systems. We find that the characteristics of an

1

evaporating thin film which are controlled by interfacial phenomena are extremely complicated but tractable.

Initially, we proposed to emphasize the "interline heat flow parameter." Because of the theoretical results of the research, this objective has been expanded to include the "capillary pumping parameter" for completeness. The interline heat flow parameter is important in ultra-thin films where the liquid-solid interfacial force field predominates, whereas the "capillary pumping parameter" is important in thicker films. In the transition region, they are both important. In the theoretical modeling of the complete meniscus, we then found it convenient to replace these two dimensional parameters with a single dimensionless group, ε. Although the analysis is restricted by the lubrication approximation to the small slope region of the meniscus, this dimensionless group has many facets which enhance the characterization of the entire meniscus. The liquid-solid interfacial force field and temperature difference fix the characteristic contact line thickness, δ_0, which is of critical importance because it controls the rest of the meniscus. The measured profile gives δ_0 and ε. Finally, we added the effect of thermal conduction in the liquid to the model.

The integral evaporative heat sink for the region where the thickness is less than δ, Q_δ, can be obtained by evaluating Eq. (1.1) at δ.

$$Q_\delta = \left(\frac{\sigma \Delta h_m}{v}\right)\frac{\delta^3 K'}{3} + \left(\frac{\bar{A}\Delta h_m}{v}\right)\frac{\delta'}{\delta} \qquad (1.1)$$

where

$\dfrac{\sigma \Delta h_m}{v}$ is the capillary pumping parameter,

$\dfrac{\bar{A}\Delta h_m}{v}$ is the interline heat flow parameter,

2

The corresponding dimensionless equation for the integral heat sink evaluated at η is

$$\bar{Q} = -\frac{\eta^3}{3}\frac{d\phi}{d\xi} \qquad (1.2)$$

where

$$\bar{Q} = -Q_\delta x_0 v / \bar{A}\Delta h_m, \quad \phi = -(\eta^{-3} + \varepsilon\eta''), \quad \varepsilon = (\sigma\,\delta_0\, v\, b)/(-\bar{A}),$$

$$\eta = \delta / \delta_0, \quad \xi = x/l$$

Equation (1.1) demonstrates that, if the physical properties of the system are known, the experimentally measured film thickness profile can be used to calculate the integral evaporative heat sink. Therefore, one of the major experimental objectives of the research was to determine the film thickness profile as a function of the experimentally varied integral evaporation rate. In addition the unknown modified Hamaker constant, $\bar{A}$, had to be determined *in situ* because it is a strong function of the surface history of the system. We note that, although the Hamaker constant is a basic constant which can be theoretically calculated for ideal surfaces, most engineering surfaces are not ideal. Therefore the Hamaker constant has to be experimentally obtained.

There are two main aspects of the research: experimental and theoretical. We will present the experimental results in Section 3. This will be followed by a presentation of the theoretical results in Section 4 where the data are successfully used to evaluate the theoretical model. A primer on surface physics which is germane to the research and an example demonstrating the use of the results of the modeling is given in the Appendices A and B. Because of experimental necessities, there are also microscopic and macroscopic aspects of the research.

1.1 Experimental

At the microscopic level, using ellipsometry and microcomputer enhanced video microscopy (based on interferometry), the film thickness profile was measured as a function of the evaporation rate for polar and nonpolar fluids. These measurements were made in the contact line region where the thickness was less than 3 μ. Therefore, the integral evaporative heat sink, Q_δ, could be obtained for this region using Eq. (1.1). We note that the important characteristic thickness at the contact line, δ_0, was experimentally measured. We also note that a portion of the line tension at the contact line (force/length), which keeps the meniscus from dewetting, is given by $\overline{A}/\delta_0{}^2$. Experimental limitations did not allow the full potential of the evaporating meniscus to be measured since the smallest value of δ_0 achieved was 2.7 nm, which is substantially larger than the presumed limit of a monolayer.

At the macroscopic level, a heat balance was obtained by comparing the total integral evaporation rate for the entire meniscus based on the integral input mass flow rate, Q_T, with that based on the temperature profile. The above was achieved using a circular heat transfer cell with a capillary feeder which was designed and developed for this project.

1.2 Theoretical

As described in Section 4, the following theoretical equation was derived to model the interfacial mass flux associated with fluid flow in an evaporating thin film.

$$\frac{1}{3} \frac{d}{d\xi} \left(\eta^3 \frac{d\phi}{d\xi} \right) = \frac{1}{1 + \kappa\eta} (1 + \phi) \tag{1.3}$$

4

where the parameter κ is

$$\kappa = \frac{a\Delta h_m \delta_o}{k}$$

This fourth order nonlinear differential equation for the dimensionless thickness has two parameters, ϵ and κ. The parameter ϵ represents the effects of intermolecular forces and κ represents the resistance to thermal conduction in the meniscus. The only unknown in the parameter κ was obtained by measuring δ_o. The experimentally measured thin film thickness profile data was successfully fitted with the model equation to obtain the important dimensionless parameter, ϵ, which includes both the surface tension and the Hamaker constant. This number combines the properties of the capillary pumping parameter and the interline heat flow parameter. Knowing the classical properties of the system, the Hamaker constant is obtained from ϵ. Once the parameter ϵ and the contact line film thickness, δ_o, are known, the ideal heat flux, q^{id}, and the liquid-vapor and solid-vapor interfacial temperature differences can be calculated. The interfacial temperature difference cannot be measured directly because of the exceptionally small thickness of the liquid-vapor interface across which the density changes from that of the liquid to that of the vapor and because the temperature difference is extremely small.

The right-hand side of Eq.(1.3) is both the dimensionless interfacial mass flux, $\dot{M}$, and the dimensionless interfacial heat flux:

$$\dot{M} = \frac{\dot{m}}{\dot{m}^{id}} = \frac{1}{1 + \kappa\eta}(1 + \phi) \qquad (1.4)$$

The ideal interfacial mass flux based on kinetic theory, $\dot{m}^{id}$, is a convenient reference flux. We find that, because the interfacial

force field (represented by ϕ which has a negative value) lowers the vapor pressure and conduction in the liquid (represented by $\kappa\eta$) lowers the temperature at the liquid-vapor interface, the ideal heat flux based on kinetic theory and the solid-vapor interfacial temperature difference, ΔT, is greater than the maximum heat flux in the evaporating meniscus. We note that the results demonstrate that these effects are large. The results also indicate that high interfacial mass (heat) fluxes can be obtained in small systems (small $\kappa\eta$) if they are stable. We note that stability should increase in small wetting systems because the relative importance of the solid substrate increases. However, this complex question has not been addressed and the experimental system was relatively large.

The resulting theoretical fit of the data is also used to obtain the experimental integral heat sink, Q_δ, and the heat flux distribution. However, since the model differential equation was derived using the lubrication approximation, it can only be accurately used in the region where $(\delta')^2 \ll 1$. This region represents only a portion of the complete macroscopic evaporating meniscus. As a result of the difference in areas, a gap remains between the macroscopically measured Q_T and the microscopically obtained Q_δ. We note that this does not detract from the main conclusion of the research: the experimental results are in agreement with the proposed model of the evaporating meniscus. Although considerable additional research needs to be accomplished concerning various fluids, surface preparation, smaller constrained systems, stability, and higher heat fluxes, the basic characteristics of the evaporating meniscus have been experimentally measured and theoretically modeled.

1.3   Application and Surface Physics

In the Appendix B, an example of the use of some of the model equations to evaluate the effect of the contact line heat sink at the exit of a capillary tube on the capillary pressure drop for fluid flow is presented. Only the effect of the disjoining portion of the evaporating meniscus on the capillary pressure is evaluated in the application section. We note that the dimensionless group ε is needed to relate the size of the heat sink in the example with that in the experimental portion of the research. The importance of the parameters ε and κ is demonstrated.

Since the use of the Hamaker constant to model evaporating ultra-thin films is relatively new, a primer on surface physics which is germane to the research is also included in the Appendix A.

1.4   Major Conclusions

I) The experimental results obtained for the relatively low heat fluxes studied generally confirm the basic model presented. Therefore, the model can be used to predict the performance of other systems and/or operating conditions.

II) We find that there are significant resistances to heat transfer in a small meniscus due to interfacial forces, viscous stresses, and thermal conduction. Therefore, the ideal heat flux based on kinetics theory cannot be obtained.

7

SECTION 2

INTRODUCTION

When a completely wetting liquid film spreads on an inclined solid substrate a "contact line" region is formed where the vapor, liquid and solid (with an adsorbed film) phases are in close proximity. At equilibrium on a horizontal surface a uniform film of constant thickness would form. Alternatively, a partially spreading fluid would form an apparent finite contact angle. We currently focus on completely wetting systems for experimental and theoretical advantages, and their basic importance. The transport processes and interfacial phenomena occurring in the microscopic contact line region [thickness $\delta < 10^{-5}$ m] are controlled by surface forces and involve a delicate balance of temperature and of capillary, dispersion and hydrostatic forces. On the other hand, large stresses are present in this interfacial region which includes the varying force fields associated with both the liquid-vapor and the liquid-solid interfaces. The stress field in the contact line region controls the rest of the meniscus. The technical applications of this generic region are legion.

2.1 Literature review

2.1.1 General

Although considerable theoretical progress [e.g.,1-26] and exciting experimental developments [e.g.,27-42] have been reported, a complete and consistent understanding of the complex physicochemical phenomena in the contact line region is still to be achieved. The primary obstacles to this endeavor are the smallness of the region under study, the large stress gradients, and its extreme

8

sensitivity to the thickness profile, the temperature gradient and to contamination. Although these factors are difficult to include in theoretical analyses and vary greatly from one experimental study to another, a general understanding of the contact line is evolving.

Consider Fig. 2.1 which represents an inclined flat plate immersed in a liquid at an angle θ to the horizontal. The plate is in a closed cell and a spreading liquid in equilibrium with its own vapor forms a zero contact angle with the plate. Except for the inclined support plate, the liquid is not constrained by solid surfaces and the liquid-vapor interface is free to adjust to the "pressure jump" at the liquid-vapor interface. Therefore, the thickness profile, δ, is a function of the pressure jump at the interface and a measurement of this profile gives the pressure field. At equilibrium, the pressure field is hydrostatic. With evaporation, the change in the profile causes a change in the pressure field that, in turn, causes fluid flow to replenish that evaporated. Since the pressure field depends on the intermolecular force field, extremely large pressure gradients are possible without cavitation. A steady state evaporating meniscus has been experimentally observed [e.g., 32, 33]. At high evaporative fluxes, an oscillating meniscus has also been observed. At very high fluxes, the meniscus becomes unstable.

We note that, due to the concept of internal pressure, the concept of pressure jump at the liquid-vapor interface is not straightforward. In addition the internal pressure is modified by the presence of the solid substrate. However, as discussed below, models have been developed and experimentally verified for the pressure jump under some conditions [e.g.,1,2,8,9,18,22,27,32,36]. Past theoretical [e.g.,1,5,10,11,16,36] and experimental [e.g.,36,40,41,42] work demonstrated that there is a narrow

9
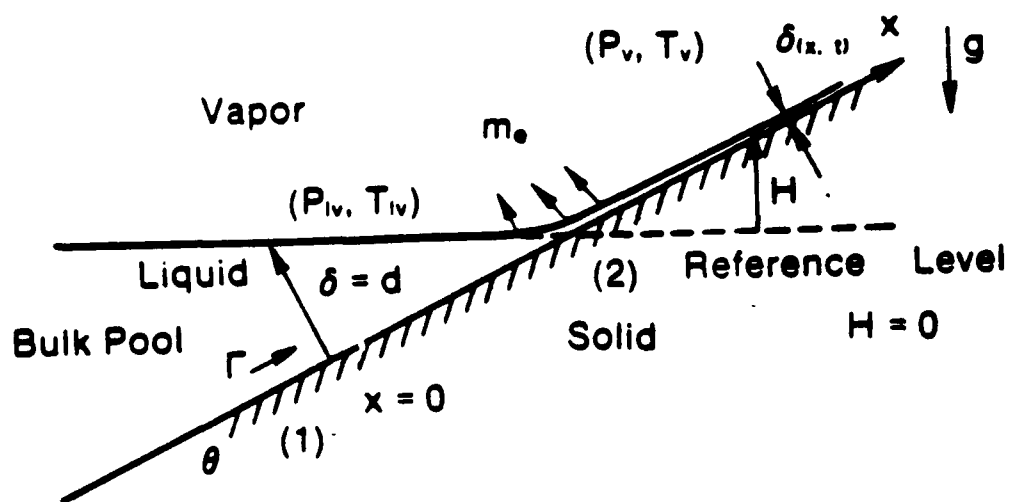
Figure 2.1   An Inclined Flat Plate Immersed in a Liquid
              at an Angle θ to the Horizontal.

10

transition region between the region dominated by capillary pressure and that dominated by disjoining pressure.

2.1.2 Equilibrium Systems (Theoretical)

Mechanical equilibrium requires a balance of dispersion, capillary and hydrostatic forces. Hence the following form of the chemical potential (per unit volume) is zero at the liquid-vapor interface [e.g., 8,19,22,36].

$$\Pi + \sigma K - \rho_l gH = 0 \tag{2.1}$$

ΔP (Pressure Jump at Liquid-Vapor Interface) =

$$P_l - P_v = -\sigma K - \Pi \tag{2.2}$$

$$K \text{ (Curvature)} = \frac{d^2\delta}{dx^2}[1 + \left(\frac{d\delta}{dx}\right)^2]^{-3/2} \tag{2.3}$$

$$\Pi \text{ (Disjoining Pressure)} = \frac{-B}{\delta^n} \tag{2.4}$$

In these equations, δ represents the film thickness, ρ_l represents the density, σ represents the surface tension and B a modified Hamaker constant (B<0 for completely wetting systems). In the limit of a very thin film of a pure simple fluid (nonretarded region) n=3 and B=A/6π = $\bar{A}$, in which A is the classical Hamaker constant; while in the thick film region (retarded region) n=4 and B is a dispersion constant. Calculations of the van der Waals interaction between different materials show that these are approximate models since the constants are weak functions of the film thickness [e.g.,2,36]. The effect of buoyancy is neglected as experimental conditions are far from the critical point (ρ_l >> ρ_v). Knowing the surface tension, a measurement of the thickness profile gives the constant B and, therefore, the characteristics of the system at the start of an

1 1

experiment [36]. For simple clean ideal systems the measured value of the Hamaker constant can be compared with the theoretical value calculated using the frequency dependent dielectric susceptibilities of the three phases. For more complicated real systems, the value of the Hamaker constant can be determined in a closed cell in situ at the start of an experiment.

We note that, if the extended meniscus is formed at the exit of a small capillary, the pressure jump can be extremely large. In the capillary case, the constraint of the solid can be used to reduce the size of the system and increase the relative importance of the interfacial force terms. This would increase the stability of the meniscus and the attainable heat flux. Because of the current experimental state of the art, a relatively large meniscus at the exit of a circular gap was studied herein using a newly designed circular capillary feeder.

2.1.3 Nonequilibrium Systems (Theoretical)

For general situations, Equations (2.6-2.10) have been derived using the lubrication approximation to the one-dimensional Navier-Stokes equations while ignoring surface tension gradients [e.g., 8,9,11,18,19,24,26,33]. A more complete description and derivation of the equations used herein are presented in Section 4.

Γ (Mass Flow Rate per Unit Width) =

$$\rho_1 \int_0^\delta u \, dy = \frac{-\delta^3}{3v} \frac{d}{dx} [\Delta P_g] \tag{2.5}$$

$$\Delta P_g = \Delta P + \rho_1 gx \sin\theta + \rho_1 g(\delta-d) \cos\theta \tag{2.6}$$

d = Film thickness at pool, where x = 0.

In the following equation for the conservation of mass, $\overset{\bullet}{m}$ represents the interfacial mass flux and t represents the time.

$$\rho_1 \frac{\partial \delta(x,t)}{\partial t} = -\frac{\partial \Gamma}{\partial x} - \overset{\bullet}{m} \qquad (2.7)$$

$$\Gamma' = \frac{\partial \Gamma}{\partial x} = -\frac{\delta^3}{3v}\left(\frac{d^2\Delta P_g}{dx^2}\right) + \frac{3\Gamma\delta'}{\delta} \qquad (2.8)$$

Using kinetic theory and interfacial thermodynamics with combined Clapeyron and Kelvin equations, the mass flux of vapor leaving the liquid vapor interface, $\overset{\bullet}{m}$, was modeled as a function of the temperature and pressure jumps at the interface in [e.g.,8,9, 11,19,44]. The resulting equation can be called either an extended Kelvin equation or an extended Clapeyron equation.

$$\overset{\bullet}{m} = a(T_{lv} - T_v) + b(\Delta P_g) \qquad (2.9)$$

$$b = C_l\left(\frac{M}{2\pi RT_{lv}}\right)^{1/2}\left(\frac{V_lP_v}{RT_{lv}}\right) ; \quad a = b\left(\frac{\Delta h}{T_v}\right) \qquad (2.10)$$

where C_l is the evaporation coefficient, Δh is the enthalpy of vaporization per unit volume, M is the molecular weight, P_v is the reference vapor pressure, V_l is the molar volume of the liquid and $(T_{lv} - T_v)$ is the characteristic temperature jump at the liquid-vapor interface. These equations demonstrate that the processes of fluid flow and phase change both depend on the intermolecular force field and are strongly coupled. We note that the extended effusion equation, Eq. (2.9), predicts that extremely large evaporative heat fluxes are possible if the system does not cavitate. Very little is known about this generic area. We also note that, as the system shrinks in size with evaporation, extremely large shear stresses occur because of flow in very thin films. Therefore, in order to

13

obtain a complete understanding of the transport processes in an evaporating extended meniscus, it is important to evaluate equilibrium systems (to calibrate the system at the start of the experiments and evaluate the interfacial force field), near-equilibrium systems (to evaluate models at low fluxes where the system does not oscillate) and high flux systems (to evaluate the system when the system oscillates and cavitation occurs). The first two are addressed herein.

An examination of the relevant physical properties of many fluids shows that these systems are extremely sensitive to a small ΔT. On the other hand, we can theoretically demonstrate that a small change in ΔT is equivalent to a large change in the stress field. Herein we are primarily concerned with spreading systems. Thus, Π and σK are both positive and the vapor pressure of these films is less than that of a bulk liquid at the same temperature. The above equations model the evaporative flux as a function of both temperature and pressure (film thickness and curvature). Derjaguin and Zorin [27] experimentally demonstrated that thin superheated (relative to a bulk liquid phase) flat adsorbed liquid films of a particular thickness on a solid substrate can exist in equilibrium ($\dot{m}$ = 0) with the saturated vapor of the bulk liquid phase. Thicker films at the elevated temperature would have a higher vapor pressure and therefore evaporate until they reach the equilibrium thickness at which the additional liquid-solid interfacial force field reduces the vapor pressure. Using Eq. (2.9) for an adsorbed film on a flat solid surface above in the vapor space but not in contact with the bulk liquid ($K = 0$ and $H \Rightarrow 0$) we find this thickness to be

$$\delta_0 = \left(\frac{-BT_v}{\Delta h \Delta T}\right)^{1/n} \tag{2.11}$$

We note that, in this region, $\Delta T = T_{lv} - T_v = T_s - T_v$. This thickness is also used to define the characteristic pressure difference (disjoining pressure at δ_0, Π_0).

$$\Pi_0 \equiv \frac{-B}{\delta_0^n} = \frac{\Delta h \; \Delta T}{T_v}$$

(2.12)

Using an example from Ref. [19], the equivalent effect of a $\Delta T = 0.1$ K for Octane on SiO_2 at 298 K with $B \equiv A/6\pi = -4.35 \times 10^{-22}$ J, n = 3, is given by $\Pi_0 = 8.5 \times 10^4$ N/m^2 ($\delta_0 = 1.72$ nm, H = 0); $K_0 = 4 \times 10^6$ m^{-1} (large δ_0, H = 0); or H = 12.4 m (K=0,$\Delta T = 0$). It is evident from these preliminary calculations and confirmed herein that small temperature differences cause extremely thin films and/or large curvatures and large pressure gradients. The thickness δ_0 is important because this is the boundary condition for an evaporating meniscus at the contact line [e.g., 9, 19]. The upper limit on ΔT for this boundary condition is unknown. However, it can be sufficiently large to allow very high heat fluxes. We note that Ref.[19] was written under the auspices of this contract. Herein, we use experimental data to confirm the characteristics predicted by this model.

2.1.4 Equilibrium Systems (Experimental)

Essentially, three different experimental techniques have been used to study the equilibrium disjoining pressure of a simple system like an alkane on a wetting substrate: I.) Derjaguin and Zorin [27], Zorin et al. [34] and Gee et al. [37] studied the adsorption of alkanes on substrates at high disjoining pressures (i.e., very thin adsorbed films which were thinner than those studied herein). Derjaguin and Zorin varied the substrate temperature whereas Gee et al. varied the vapor pressure; II.) Blake [30] measured the disjoining pressure of

alkanes on α-alumina by pressing a gas bubble against the substrate at low disjoining pressures which are not easily attainable by vapor adsorption; III.) Ingram [29] studied very low disjoining pressures by measuring the thicknesses of alkane films which remained on a silica plate after draining. Truong and Wayner [36] and Sujanani and Wayner [40] used the set-up presented in Figure 2.1 to measure the profile in both the low disjoining pressure region just above the transition region and the capillary pressure region. The results presented in [27,34,36,37] agree that the DLP theory [2] correctly predicts the value of the Hamaker constant. Ingram found that octane and higher alkanes gave much thinner films after drainage than predicted whereas the lower alkanes gave the thicker films expected [29]. He attributed this discrepancy to either contamination (possibly adsorbed water), temperature gradients and/or to a microporous substrate. The final thickness obtained in the study of a draining film of octane on silicon by Sujanani and Wayner [40] agreed with the results of Ingram. They concluded that their relatively large cell became contaminated over the long time period required for the study of drainage and that nonisothermal zones were present in the cell. Using SF_6, Kayser et al. [35] experimentally confirmed that small temperature gradients have a large effect on the adsorbed film thickness. Truong and Wayner found the same effect in heat transfer studies [41]. In a recent study by Sujanani and Wayner [42] on the near equilibrium thickness profile of an extended meniscus, the DLP theory and the extreme sensitivity of the system to small temperature changes were experimentally confirmed and analyzed. The DLP theory has also been confirmed by Sabisky and Anderson for Helium [31]. The DLP theory for alcohols and water has also been confirmed. Therefore, we find ample experimental evidence for "thick"

adsorbed wetting films which are very sensitive to small
temperature differences. Herein, we confirm this observation using
a unique nonequilibrium system.

2.1.5 Nonequilibrium Systems (Experimental)

The isothermal and the evaporating meniscus thickness profiles
in the region controlled by capillarity have been measured as a
function of heat flux using interferometry [e.g., 15,32,33,39,41]. The
profile of a wetting liquid near the transition region, where both
capillary and van der Waals dispersion forces are equally important,
has also been measured using interferometry and ellipsometry
[28,36,40,42]. In these cases, the thickness in the capillary region was
determined as a function of position by measuring the locations of the
interference fringes. The thickness in the flat portion of the adsorbed
film was measured using ellipsometry. In [42] additional physical
insights concerning the stability of the profile were obtained using
microcomputer enhanced video microscopy, wherein each pixel was a
photometer, to obtain a continuous profile down to the thickness of the
adsorbed film and then by using ellipsometry to confirm the thickness
in the flat region. The resulting equilibrium and near equilibrium
characteristics confirmed past theoretical predictions concerning the
thickness of the adsorbed film [e.g., 2,36], the width of the transition
region [e.g., 10,11], and the effect of heat transfer on the film thickness
profile [e.g., 8,9,11]. As demonstrated in this research, the advantages
of previously developed optical techniques to study the details of
interfacial processes are significantly enhanced when coupled with the
convenience of video image processing. Beaglehole has used
microscopic imaging ellipsometry to measure the profiles of the
precursor of spreading drops of a low vapor pressure fluid (siloxane)
on various substrates [38]. Previously, Bascom et al. measured the

17

profile of the leading edge of a spreading drop using ellipsometry [28].
Herein, using a new heat transfer cell we present experimental and
theoretical results that confirm the modeling represented by Eqs.(2.5 -
2.11) and presented in Section 4.

SECTION 3

EXPERIMENTAL

A cross-sectional diagram of the circular capillary feeder system is shown in Fig. 3.1. Liquid flows from a reservoir (maintained at a constant level) as a result of a difference in capillary pressure, hydrostatic head and disjoining pressure (caused by intermolecular forces) and forms a meniscus at the edge of the thinner gap at position 2. The contact line region, area 3, governs the critical initial condition for the stability and behavior of the evaporating meniscus and hence the performance of the capillary feeder system. Liquid evaporated from this region is replenished by fluid flow from the reservoir. In the thinnest portion of the meniscus represented by δ_0 evaporation does not occur.

The first objective of this study was to determine the film thickness profile in the absence of external perturbations. This "isothermal" profile gives the pressure field and the interfacial properties (i.e., $\bar{A}$ by measuring δ_0) and yields information on sensitivity to evaporation/condensation. The capillary feeder system was designed to provide a stable meniscus with the center of the silicon wafer heated to induce evaporation. The change in the pressure field was manifested as a change in shape of the film thickness profile which was measured. This data coupled with the interfacial characteristics and the macroscopic temperature profile allowed the evaluation of transport processes. Using the capillary feeder system, the amount of fluid evaporated from the entire meniscus was also obtained. Although the main objective of this study was the evaluation of the theoretical model at low

19
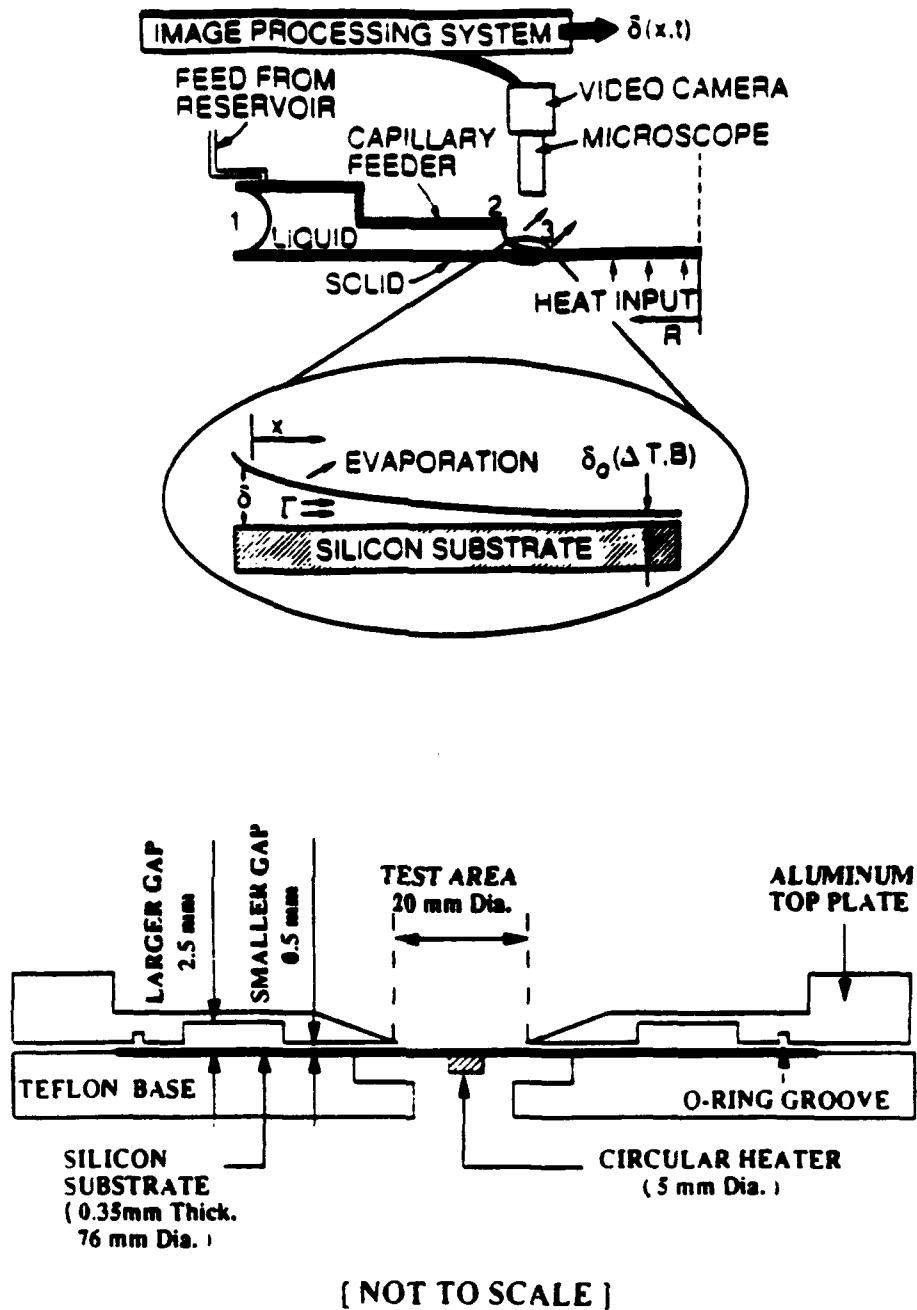
Figure 3.1   Cross Sectional View of Capillary Feeder.

20

evaporation rates, oscillating meniscus profiles at higher power inputs were also observed.

3.1 Heat Transfer Cell

An aluminum trapezoidal cell chamber was fabricated to enclose the circular capillary feeder system, which allowed for measurable continuous liquid feed with simultaneous interferometric and ellipsometric measurements of film thicknesses. A photograph of the system is presented in Figure 3.2. Two wide circular grooves with different channel depths as shown in Figure 3.1 were made by a milled aluminum washer pressing against a smooth silicon wafer with a Teflon encapsulated O-ring in between. The difference in groove depths maintained a steady flow of liquid towards the center of the silicon plate by capillary pumping to replenish the amount evaporated. The circular test area and a circular heat source, made by baking a platinum compound, naturally eliminated edge effects. Small (0.3 mm) chromel-alumel thermocouples (not shown) were attached 1.5 mm apart on the bottom of the silicon substrate to measure the temperature. Special optical windows were made at 70° angles with the base for maximum ellipsometric sensitivity. The capillary feeder was connected to an outside reservoir (a graduated cylinder which contained pure test liquid) by means of a very thin capillary tube which supplied fresh liquid by capillary suction to replenish the liquid evaporated in the test area. It was very important to manually keep the liquid levels nearly the same in the reservoir and the feeder. A small change in the hydrostatic head could overflow or empty the feeder. For the large dimensions used in the experimental cell, we found the system very sensitive to small

21
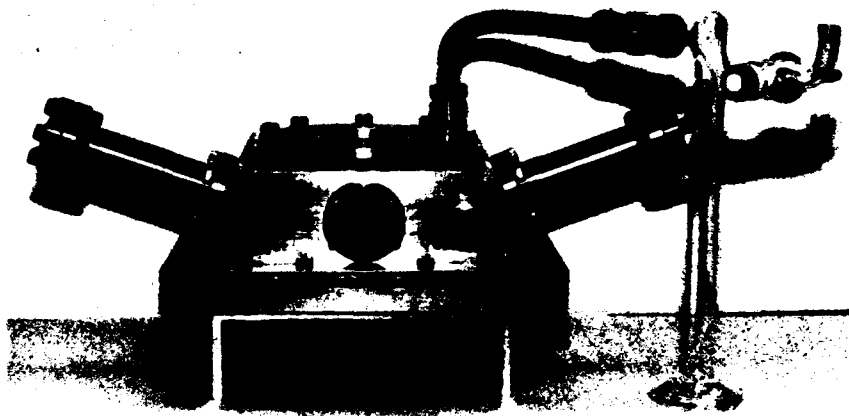
Figure 3.2   Photograph of the Heat Transfer Cell.

22

changes in pressure. The total rate of evaporation was calculated by measuring the amount of liquid added to the outside reservoir.

3.2 Macroscopic Heat Transfer

Representative temperature profiles for two input power settings with and without fluid in the cell are presented in Figure 3.3. From the macroscopic temperature profiles, the total rate of heat loss (conductive, convective and evaporative), Q_L, from the whole extended meniscus between R_1 and R_2 was calculated for the dry and wet cases using:

$$Q_L = 2\pi ks \left(R_1 \frac{dT}{dR} \Big|_{R_1} - R_2 \frac{dT}{dR} \Big|_{R_2} \right) \tag{3.1}$$

Here R_1 is chosen as $R = 10$ mm, beyond which the evaporation rate is small. R_2 is chosen as $R = 7$ mm, because for $R < 7$ mm only a thin adsorbed film exists where evaporation is presumed to be negligible. For the dry case $Q_{L,dry}$ is equal to Q_{LC}, where Q_{LC} is only the conductive and convective losses. But for the wet (with liquid) case $Q_{L,wet}$ is related to Q_{LC} by the following relation:

$$Q_{L,wet} = Q_{LC} + Q_{ev} \tag{3.2}$$

Where Q_{ev} is the evaporative heat loss. If we assume that the heat loss due to conduction and convection mechanisms does not vary significantly between the cases when the plate is dry and when the liquid is introduced to form a meniscus, the evaporative heat losses may be calculated as:

$$Q_{ev} = 2\pi ks \left(R_1 \left(\frac{dT}{dR} \Big|_{R_1,wet} - \frac{dT}{dR} \Big|_{R_1,dry} \right) \right.$$

$$\left. - R_2 \left(\frac{dT}{dR} \Big|_{R_2,wet} - \frac{dT}{dR} \Big|_{R_2,dry} \right) \right) \tag{3.3}$$

23
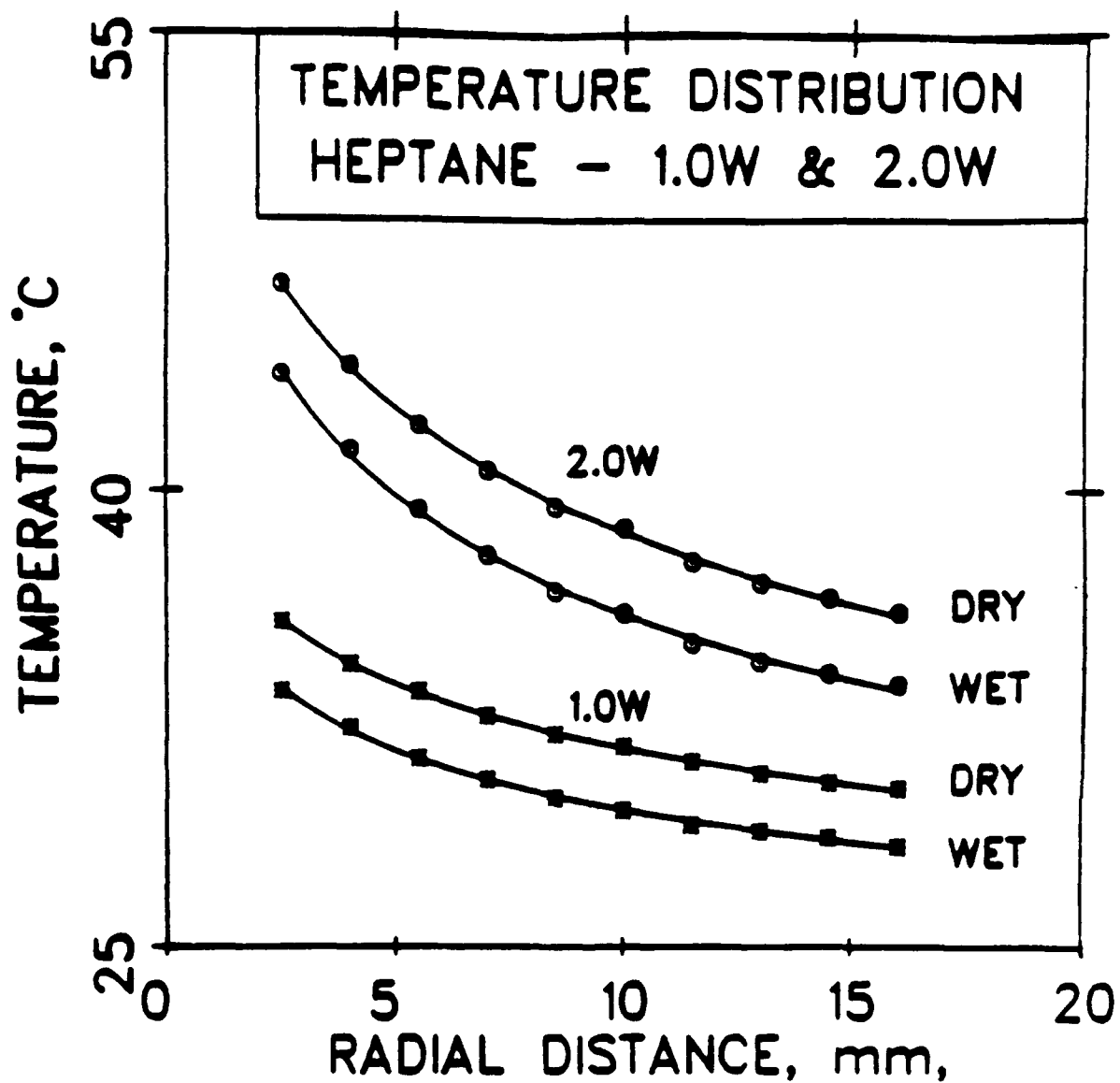
Figure 3.3   Temperature Distribution in the Substrate.

This evaporative heat loss was successfully compared to the one calculated using the measured macroscopic liquid input rate at the reservoir, Γ_r:

$$Q_T = \Gamma_r h_{fg} \qquad\qquad (3.4)$$

The temperatures obtained from the thermocouples were plotted against the radial distance, R, to construct the temperature profiles for different power inputs for both dry and wet plates. The finite difference Levenberg-Marquardt algorithm was used to fit the temperature data with radial distance. The functional relationship was then differentiated to find dT/dR at different R values. Finally, using Eq. (3.3), Q_{ev}, the integral value of the evaporation rate for different power inputs was obtained. The evaporative heat required was also determined from the amount of liquid supplied to the reservoir using Eq. (3.4). In Table 1 the values of Q_{ev} obtained using these different methods are presented. The slightly higher value of Q_{ev}, predicted at the highest power inputs by the model, may be a result of our assumption that Q_{LC} is the same for both dry and wet cases. Conceivably, $Q_{LC,wet}$ is higher than $Q_{LC,dry}$ because of the presence of vapor. Hence the left hand side of Eq. (3.3) should be $Q_{ev} + (Q_{LC,wet} - Q_{LC,dry})$.

Table3.1. Integral Evaporation Rate as a Function of the Heat Input Rate

Power (watts)	Q_T (watts)[1]	Q_{ev} (watts)[2]
Liquid: Heptane		
1.0	0.041	0.042
2.0	0.075	0.060
3.5	0.126	0.120
4.0	0.170	0.190
Liquid: R113		
0.25	0.033	0.030
0.35	0.038	0.041
0.50	0.045	0.049

[1]Eq. (3.4);   [2]Eq. (3.3)

25

We conclude that a heat balance was obtained since Q_T agrees reasonably well with Q_{ev}. This confirms that substantial evaporation was present. Only a small percentage of the input power is used to evaporate the liquid because of the substantial values of the convective and conductive terms.

3.3 Optical Measurements

3.3.1 Ellipsometry

Ellipsometry uses the interference of elliptically polarized monochromatic light to analyze and measure the film thickness of thin films. It is a very powerful yet sensitive method, and is applicable to a wide variety of situations. In ellipsometry, the change in state of polarization due to reflection is measured in terms of properties of the reflecting surface. From a clean, film-free surface, the analysis of elliptically polarized reflection can be used to determine the optical constants of the surface, namely the refractive index and the extinction coefficient. For a surface having a thin film, given the properties of the substrate, one can determine the film thickness and if the film is thick enough ($\delta > 30$ nm), the refractive index of the thin film.

A schematic diagram of the experimental set-up for the ellipsometer is shown in Figure 3.4. A conventional null ellipsometer with the configuration of light source, polarizer, fixed compensator, sample, analyzer, microscope objective lenses and a photodetector was used to determine the film thickness of the flat adsorbed film which forms ahead of the meniscus. The light source was a Hughes Model 3022H He-Ne laser of 5 mW power which

A: Analyzer   M: Microscope
C.   Compensator   MUL: Monochromatic
CPL. Circularly Polarized Light   Unpolarized Light
D: Detector   P: Polarizer
F: Filter   PM: Photomultiplier
FCG: Frame Code Generator   PPL: Plane Polarized Light
HRV: Image Resolution VCR   VA: Variable Aperture
IPM: Image Processing   SS: Scanning Stage
        Microcomputer   VC: CCD Video Camera
L: Helium-Neon Laser
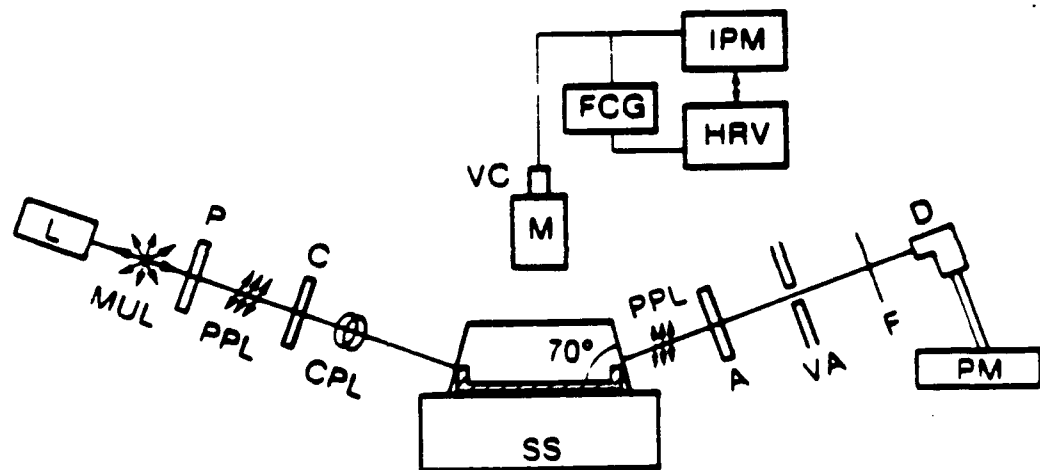
Figure 3.4   Schematic Diagram of Experimental Set-up.

emitted unpolarized, monochromatic light at a fixed wavelength of
6328Å When plane polarized light is incident on a solid surface, the
reflectr l light becomes elliptically polarized. The changes in
polarization, i.e., the relative amplitude (Ψ) and phase angle (θ),
depend on the optical constants of the solid, the angle of incidence and
the wavelength of light. If there is a thin film adsorbed on the
surface, Ψ and θ will also depend on the optical constants and
thickness of the film. A computer program based on the algorithm of
McCrackin was used to calculate the film thickness from Ψ and θ which
were measured in two optical zones and zone averaged [36,51]. The
measuring precision of our ellipsometry system was checked prior to
the experiment by measuring the optical constants (refractive index)
of a bare silicon wafer. (Measured optical constants for silicon n_S=3.85
$\pm$ 0.01, k_S=0.05 $\pm$ 0.02; literature values n_S=3.882, k_S=0.019 [36].)

3.3.2   Interferometry

The interference phenomena associated with monochromatic
light reflected from a tapered film were used to determine the
profile of the capillary meniscus in the thickness range $\delta \geq 0.1$ μm.
Alternating constructive and destructive interference occur when
coherent light is reflected from the two interfaces of the thin liquid
film and recombine. Destructive interference occurs when the optical
paths of the two reflected beams are such that they are out of phase
by π. In our case $n_v < n_l < n_s$; therefore, there is a phase shift equal
to π at each interface. The relevant equation for the film thickness
associated with the minima is:

$$\delta = \frac{(2L + 1)\lambda}{4n_l} \qquad L = 0,1,2,... \qquad (3.5)$$

where n is the refractive index, subscripts l, v and s denote liquid,
vapor and solid respectively, λ is the wavelength of the

28

monochromatic light and L is the order of the destructive (dark) fringes. We used a high power, long working distance microscope (Wild Model M420) to view the naturally occurring interference fringes in the thicker portion of the thin film. A picture showing representative sample is presented in Figure 3.5. Coherent light ($\lambda = 525$ nm) was used at normal incidence and the reflected interference patterns were captured using a CCD camera (Sony HVM200).

3.4 Image Processing

To automate data acquisition, improve data resolution and enhance data analysis, we analyzed the interferometric images using an image processing system. The first step in digital image processing is the conversion of the optical image into a form that can be stored in computer memory. This conversion is performed by a light sensitive system known as an optical digitizer, which produces coded numbers that are a measure of light intensity in the optical image. This process is called digitizing, and the stored numerical representation of the original optical image is called a digital image. The digital image can be manipulated like any other data stored in computer memory. All such manipulations can be placed in one of two general categories: image analysis or image enhancement. The term image analysis refers to the use of digital computers to derive numerical information regarding selected image features, such as lengths, areas, intensity distribution, etc. Image enhancement, on the other hand, is a procedure for manipulating the video signal to sharpen or otherwise improve the video picture. Routines for image enhancement differ from those of image analysis in that the object of the processing is not to produce descriptive information about the image, but rather to manipulate

29

125 μm
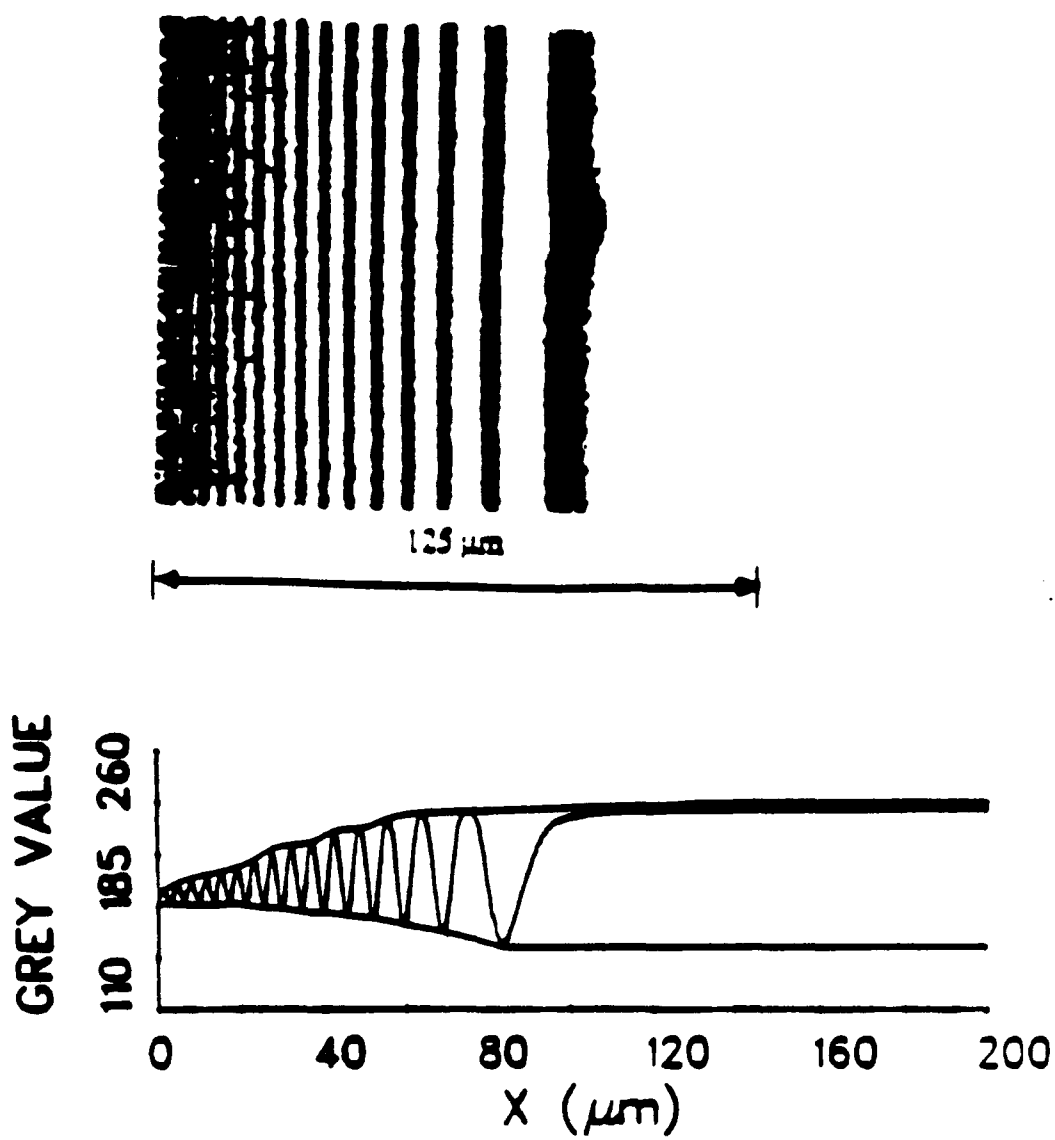
Figure 3.5   Interference Bands and Reflectivity Profile.

the image in such a way that it is more useful to a human observer. We used both the techniques in our work.

Briefly, the system consisted of a 16 MHz IBM-PC286 clone computer equipped with real-time frame grabber and frame processor boards (DT-2851 and DT-2858 from Data Translation Inc.). The image captured from the microscope through a CCD camera was digitized into 490 (vertical) x 512 (horizontal) space pixels and assigned one of 256 possible grey values representing an intensity from 0 (black) to 255 (white). Thus the image area, already magnified considerably by the microscope, was divided into microscopic pixels which acted as individual, simultaneous light sensors. Each picture provided data on one frame; i.e., 1/30th of a second in real time. The interferometric fringes formed were parallel because the radial distance from the center [~8.8 mm] was large compared to the meniscus width [~0.2 mm]. When viewed at high magnification, [area viewed ~0.3 mm x 0.3 mm] the fringes were almost invariant in a direction perpendicular to the radius and could therefore be averaged spatially to improve the signal/noise ratio. The light level was optimized to prevent pixel saturation (excessive light) and to ensure linearity of the analog to digital conversion. Light below a certain level drastically increased the signal/noise ratio. For our system the best combination of resolution, light level, signal/noise ratio and magnification was found by adding a 4.0 X effective magnification in the tube. Each pixel represented a diameter of 0.625 μm. Transient data were captured by continuously recording on a high quality U-Matic Sony VO-9600 VCR. The VCR had a B/W resolution of more than 300 lines and was connected through a Sony FCG-700 Frame Counter,

which superimposed each frame with a permanent identification
number.

3.5   System   Operation

Silicon was used as the substrate because of its reflective,
polished, smooth, easily available and reproducible surface. We
note that a native oxide about 3~5 nm thick is always present on
the surface. The exact composition of this layer depends on the
prior history of the wafer. All cleaning procedures were done inside
a class-100 clean hood. The cell was first immersed in pure ethanol
(absolute-200 proof) for 6 to 7 hours. The cell parts were again
rinsed with fresh alcohol and then dried in an oven at 180°C.
Extreme care was taken to ensure that no dust particles or
impurities could come in contact with the silicon wafer. After
drying, the cell parts were rinsed with pure test fluid and blow
dried with extra-dry grade nitrogen. The assembled cell was
mounted on the stage of a high power long working distance WILD
microscope. The system was left to equilibrate with the
surroundings for about 3 hours before taking data. An optical
interference pattern representing the thickness profile was readily
observed: an example is given in Figure 3.5. The pattern was then
analyzed to determine the film thickness profile as detailed in the
next section. The temperature distribution along the wafer and the
macroscopic liquid flow rate were also noted.

3.6 Image   Analysis

From a picture a plot of the pixel grey value versus distance
was extracted. The grey value at each pixel is a measure of the
reflectivity which changes with film thickness. In particular for a

32

thin liquid film of refractive index, n_l, on a solid surface of refractive index, n_s,

$$RL \ (\text{Reflectivity}) = \frac{\alpha + \beta \cos 2\theta_1}{\kappa + \beta \cos 2\theta_1};$$

$$\theta_1 = 2\pi n_l \delta / \lambda; \quad \alpha = r_1^2 + r_2^2; \quad \beta = 2r_1 r_2; \quad\quad (3.6)$$

$$\kappa = 1 + r_1^2 r_2^2; \quad r_1 = \frac{n_l - n_v}{n_l + n_v}; \quad r_2 = \frac{n_s - n_l}{n_s + n_l}$$

where n_v is the refractive index of vapor and λ is the wavelength of light in vacuum. As is evident from Eq. (3.6), the reflectivity undergoes a cyclic change with increase in film thickness.

$$RL_{max} = \left(\frac{r_1 + r_2}{1 + r_1 r_2}\right)^2 = \frac{\alpha + \beta}{\kappa + \beta}; \quad \theta_1 = 0, L\pi \quad\quad (3.7)$$

$$RL_{min} = \left(\frac{r_1 - r_2}{1 - r_1 r_2}\right)^2 = \frac{\alpha - \beta}{\kappa - \beta}; \quad \theta_1 = \frac{\pi}{2}, (L + \frac{1}{2})\pi \quad\quad (3.8)$$

The computer program scanned the peaks and valleys and filtered the noise from the real peaks/valleys. It then interpolated peak/valley envelopes and by analyzing the relative reflectivity of any given pixel with respect to these (dark and light pixel envelopes), determined a film thickness at every pixel. Thus,

$$\bar{G}(x) = \frac{G(x) - G_{min}(x)}{G_{max}(x) - G_{min}(x)} \quad\quad (3.9)$$

$$2\theta_1 = \text{Cos}^{-1}\left(\frac{\beta + \kappa \ \{1 - 2 \ \bar{G}(x)\}}{\beta \ \{2\bar{G}(x) - 1\} - \kappa}\right) \quad\quad (3.10)$$

where $G_{min}(x)$ and $G_{max}(x)$ are the interpolatory envelopes to the various order minima and maxima (except for the first dark fringe,

33

where linear extrapolation and matching with ellipsometric data were done). By knowing θ_1 and the order 'L' of the fringe, δ was found.

3.7 Experimental Results

Two examples of the measured thickness profiles are shown in Fig. 3.6. The profiles were shifted on the x axis to the same relative position at a fixed thickness. The adsorbed film thicknesses in the flat region were $\delta_0 = 7.5$ nm and $\delta_0 = 15$ nm. The profile for $\delta_0 = 15$nm can be termed as a "_very near_ equilibrium case with _very small_ evaporation," whereas $\delta_0 = 7.5$ nm is a "_near_ equilibrium case with _small_ evaporation." Subsequent analysis and discussion in this report will clarify these terminologies. Figure 3.7 shows thickness profiles obtained during evaporation with controlled rates of energy input, Q. These two figures clearly show that the isothermal profiles are more spread out and that the thickness of the adsorbed film, δ_0, decreases with an increase in power input (surface temperature). In an isothermal horizontal system of spreading liquid on a solid substrate at the exit of a capillary the curvature should remain constant in the region where dispersion forces can be neglected. So the film profile in this range approximates a parabola and a plot of $\delta^{1/2}$ vs x is a straight line. If the curvature is constant, it is related to the slope of this line as $K_c = 2(d\delta^{1/2}/dx)^2$. The experimental values of $\delta^{1/2}$ are also given in Figs. 3.6 and 3.8. For the case where $\delta_0 = 15$ nm, $\delta^{1/2}$ vs x is nearly a straight line which means the system was very close to isothermality, but for $\delta_0 = 7.5$ nm the line bends downward, showing the presence of a curvature gradient and hence some evaporation. Although the heater was off, Q = 0, a small amount of heat conduction from the surroundings caused the
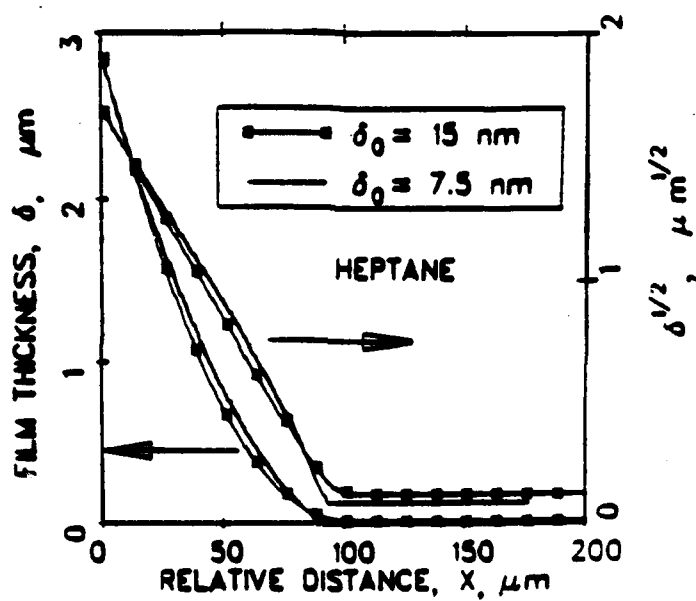
Figure 3.6 Film Thickness Profile for Heptane on Silicon with a Native Surface Oxide. (Very near equilibrium with very small evaporation, $Q = 0.0W$, $\delta_0 = 15$ nm and near equilibrium with small evaporation, $Q = 0.0W$, $\delta_0 = 7.5$ nm).

35
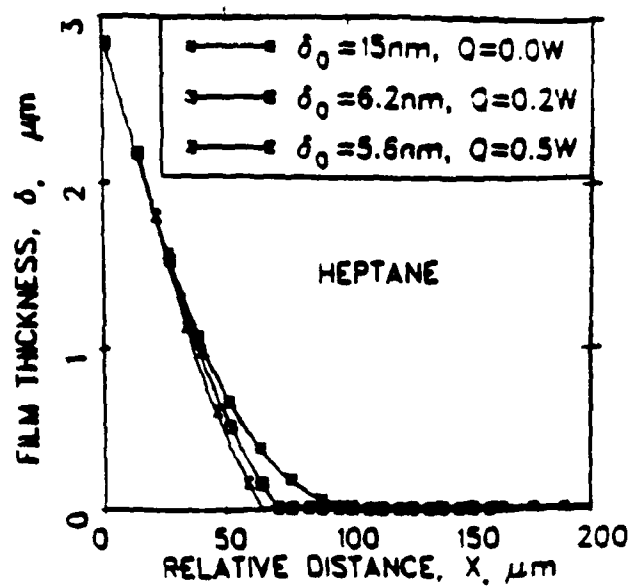
Figure 3.7   Film Thickness Profiles for Heptane on Silicon with a Native Surface Oxide. (Very near equilibrium with very small evaporation. $\delta_0 = 15$ nm and evaporation with controlled rate of heat inputs. $\delta_0 = 6.2$ nm and 5.6 nm).
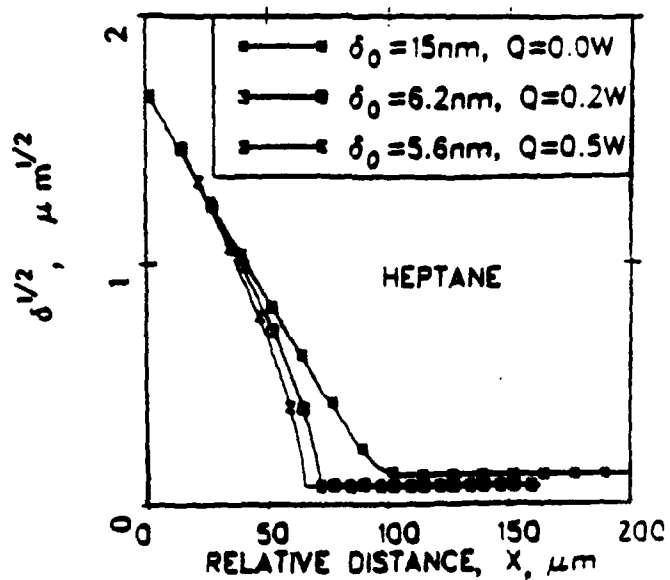
Figure 3.8 $\delta^{1/2}$ vs. X.

phase change. Other film thickness profiles are presented in Figs 3.9-3.22.

To compute the meniscus curvature, the profile data need to be differentiated twice, but magnifications of experimental errors need to be controlled at every differentiation step. In References [42,52], the process of cubic spline fitting and numerical differentiation was used. Herein, we fit the data with a theoretical model as described in Section 4. The current procedure seems to be more accurate because of the location of the maximum curvature and the effect of surface tension. Further, the comparison between the theoretical and experimental thickness profiles is easy to evaluate.
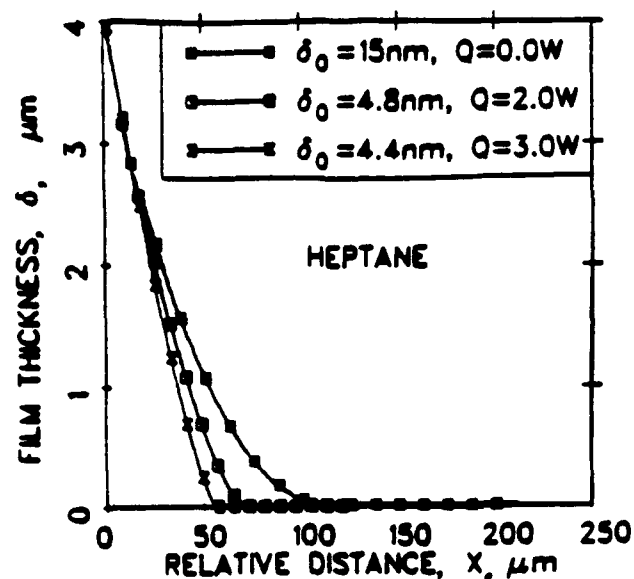
Figure 3.9   Film Thickness Profiles of Heptane on Silicon with a Native Surface Oxide. (Very near equilibrium with very small evaporation, δ_0 = 15 nm and evaporation with controlled rate of heat inputs, δ_0 = 4.8 nm and 4.4 nm).

Figure 3.10 $\delta^{1/2}$ vs. X.
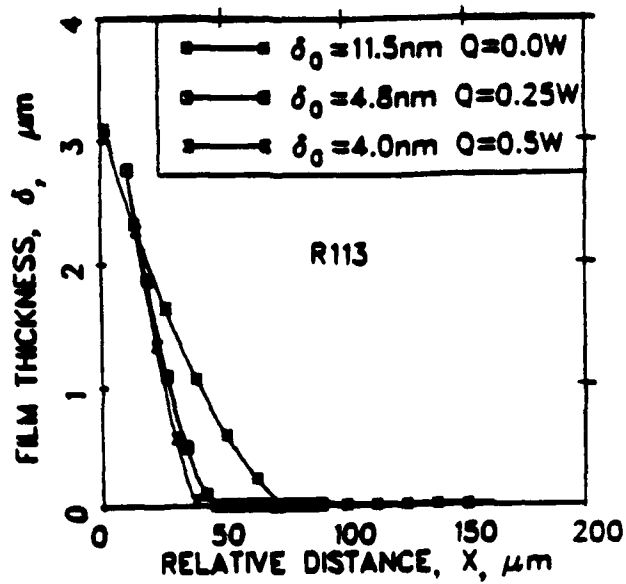
Figure 3.11　Film Thickness Profiles of R113 on Silicon with a Native Surface Oxide. (With no heat input, $\delta_0 = 11.5$ nm and evaporation with controlled rate of heat inputs, $\delta_0 = 4.8$ nm and 4.0 nm).

Figure 3.12　$\delta^{1/2}$ vs. X.

39
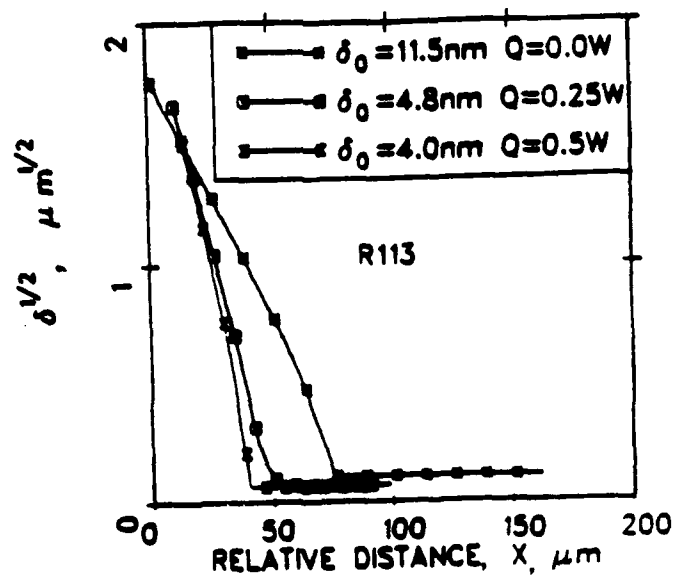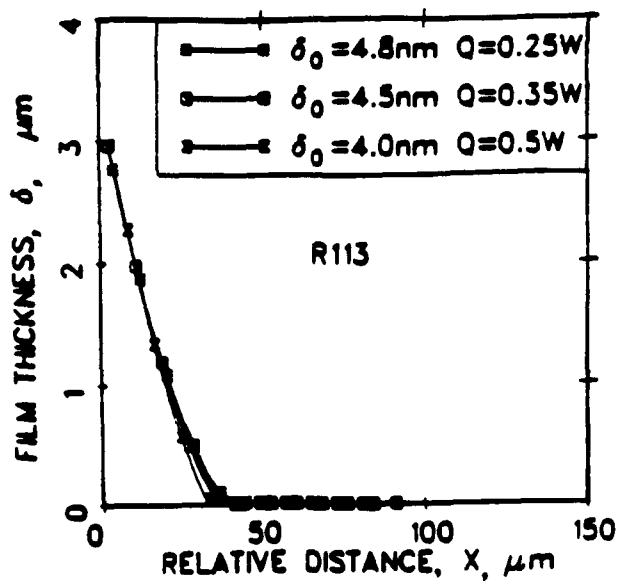
Figure 3.13   Film Thickness Profiles of R113 on Silicon
with a Native Surface Oxide. (Evaporation
with controlled rate of heat inputs, $\delta_0 =$
4.8 nm, 4.5 nm and 4.0 nm).

Figure 3.14 $\delta^{1/2}$ vs. X.

40
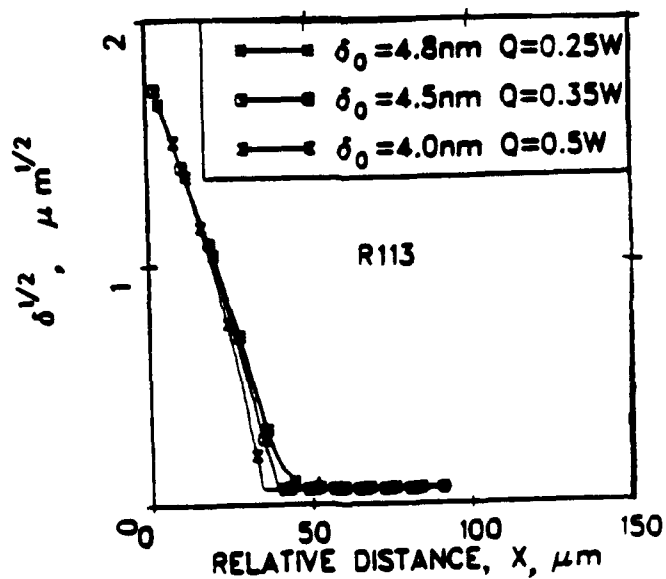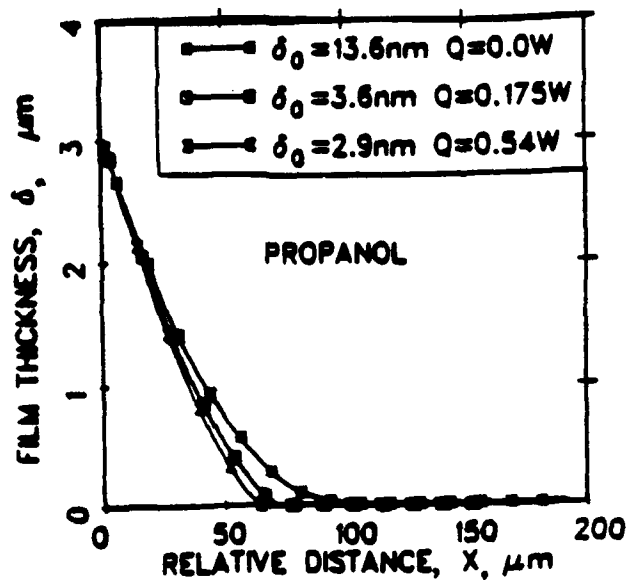
Figure 3.15   Film Thickness Profiles of Propanol on
Silicon with a Native Surface Oxide. (With no
heat input, δ_0 = 13.6 nm and evaporation
with controlled rate of heat inputs,
δ_0 = 3.6 nm and 2.9 nm).
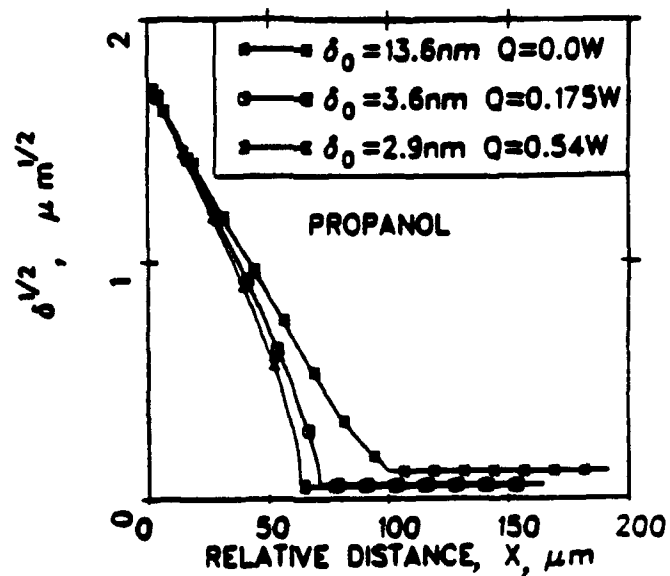
Figure 3.16 $\delta^{1/2}$ vs. X.
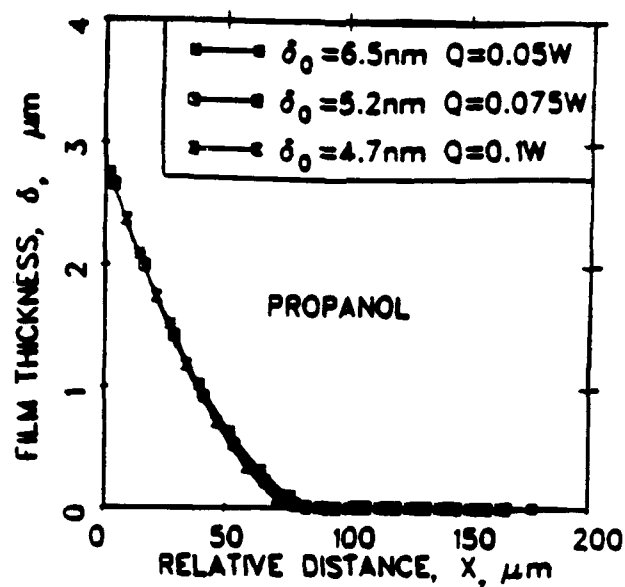
Figure 3.17   Film Thickness Profiles of Propanol on
Silicon with a Native Surface Oxide.
(Evaporation with controlled rate of heat
inputs, δ_0 = 6.5 nm, 5.2 nm and 4.7 nm).

Figure 3.18 $\delta^{1/2}$ vs. X

42
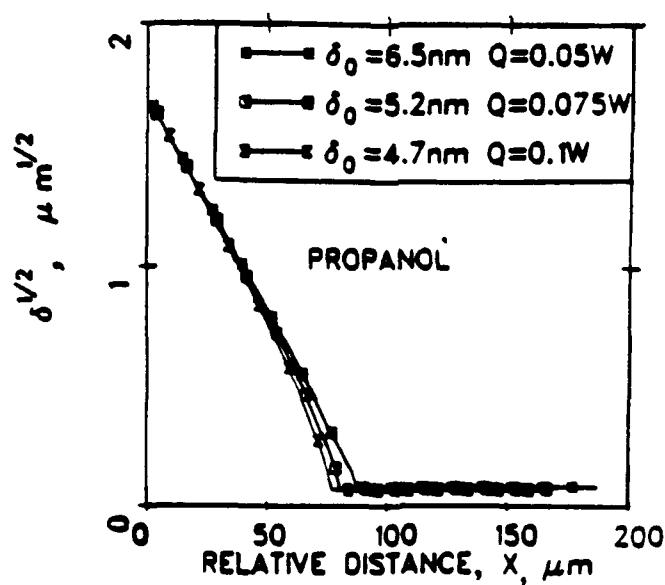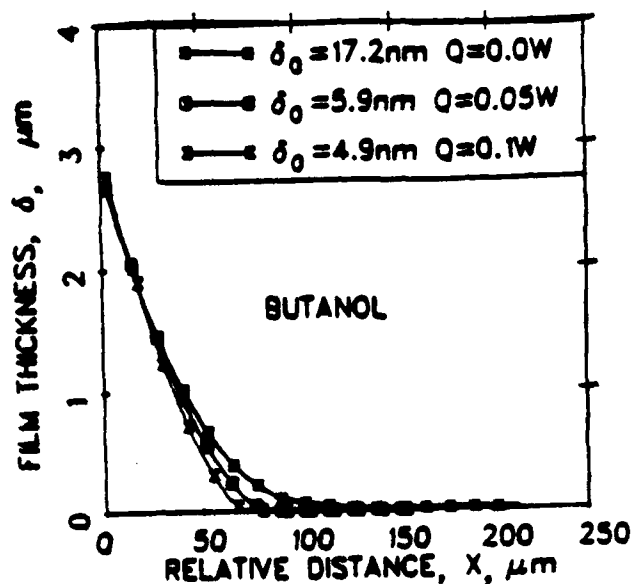
Figure 3.19   Film Thickness Profiles of Butanol on Silicon with a Native Surface Oxide. (With no heat input, δ_0 = 17.2 nm and evaporation with controlled rate of heat inputs, δ_0 = 5.9 nm and 4.9 nm).

Figure 3.20 $\delta^{1/2}$ vs. X.

43
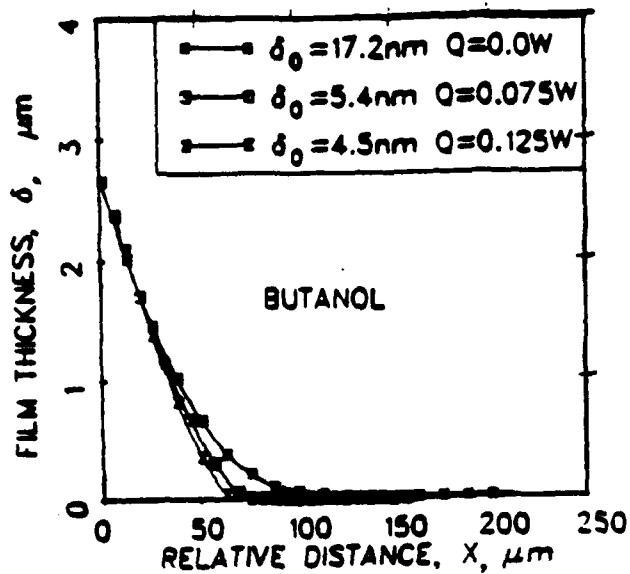
Figure 3.21   Film Thickness Profiles of Butanol on
Silicon with a Native Surface Oxide. (With
no heat input, $\delta_0 = 17.2$ nm and evaporation
with controlled rate of heat inputs,
$\delta_0 = 5.4$ nm and 4.5 nm).
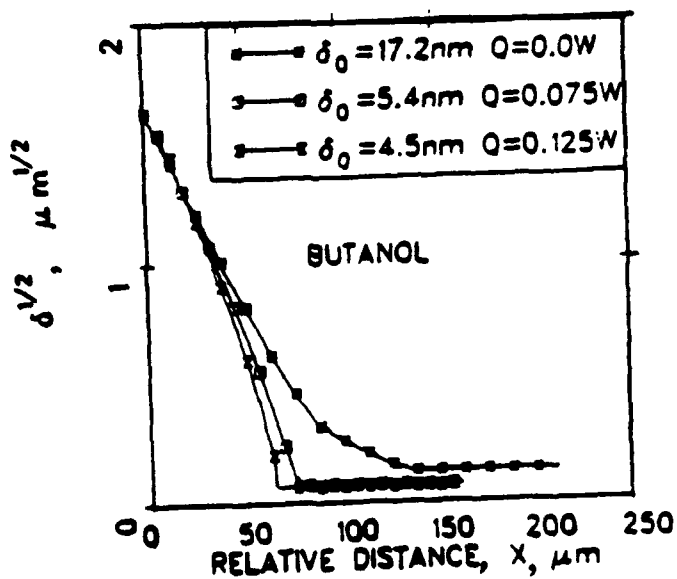
Figure 3.22 $\delta^{1/2}$ vs. X.

SECTION 4

THEORETICAL

The immediate theoretical precursors to this work are the studies of Wayner, et al. [9], Moosman and Homsy [11], and Wayner [19]. A substantial portion of the material in the initial theoretical paper associated with this project [19], which developed the connection between the film tension and the following equations, will not be included herein. It was included in the interim report (WRDC-TR-90-2008). The current work includes all of the effects considered by Wayner, et al. [9,19] and Moosman and Homsy [11] but the nonlinearity of the combined effects is dealt with numerically. Consider a stationary thin film at the leading edge of a thicker pool of a pure liquid (also stationary) on a horizontal substrate. The liquid wets the solid substrate and therefore at steady state the thin film extends a large distance from the bulk pool. This configuration is shown in Figure 4.1. Because the film is thin it is strongly influenced by capillary effects and by adsorption forces. In this study the adsorption forces are restricted to the London-van der Waals dispersion force and the film is assumed to be flat enough that the hydrodynamics are governed by lubrication phenomena. Thus the pressure in the liquid does not vary in the direction perpendicular to the substrate.

Liquid flows in the steady film because of evaporation resulting from superheating. The local evaporation rate is affected by the local superheat and the local film pressure. The film pressure reflects the adhesion of the liquid to the solid substrate and the capillary pressure. The tendency of the liquid to evaporate is reduced by adhesion and a negative capillary pressure. (A negative capillary pressure is caused by a thin film which is concave
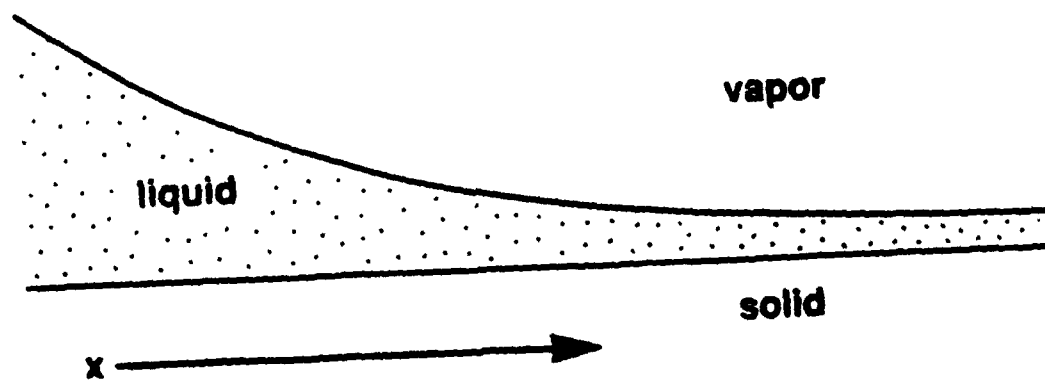
Figure 4.1   Theoretical Configuration.

towards the vapor phase.) The local superheat is the temperature difference between the liquid-vapor interface and the vapor phase. The vapor phase is assumed to be isothermal and pure.

Heat flows from the substrate through the film to the liquid-vapor interface where evaporation occurs. Since the substrate is assumed to be isothermal, and the film has a resistance to heat conduction, we expect that the liquid-vapor interface of the thicker portions of the film will be less superheated than the thinner portions.We assume that the film extends an infinite distance from the pool. If the film is thin enough, the liquid-solid intermolecular force field is sufficiently strong to keep the film from evaporating even though it is superheated. Therefore, we expect the evaporation rate to be highest where the film thickness is moderate. Far from the liquid pool the film does not evaporate at all. The variation of surface tension with temperature is neglected.

The literature provides relationships which are the building blocks of the model of the horizontal evaporating thin film [e.g., 9,11,19]. The film thickness is defined to be δ, and the coordinate along the solid substrate is x as shown in Figure (4.1). The liquid pressure, P_l, is related to the vapor phase pressure, P_v, by:

$$P_l - P_v = \frac{\bar{A}}{\delta^3} - \sigma \frac{d^2\delta}{dx^2} \qquad (4.1)$$

where $6\pi\bar{A}$ is the Hamaker constant which is negative for a spreading liquid, and σ is the surface tension. The first term in Eq. (4.1) is called the disjoining pressure and represents the body force on the liquid due to van der Waals dispersion phenomena. According to Eq. (4.1), the adhesion effect is larger for a thinner film. The expression used for disjoining pressure is for a flat film, so we

47

require the film to be fairly flat. According to a two-dimensional-force balance for a nonevaporating static film by Kralchevsky and Ivanov [53], the surface tension in a thin film is not constant. Applying their analysis to a fairly flat film we find the variation of the surface tension to be inconsequential. The simplified form of curvature is used because the film is assumed to be fairly flat. The precise curvature is:

$$K = \frac{\frac{d^2\delta}{dx^2}}{[1 + (\frac{d\delta}{dx})^2]^{3/2}} \tag{4.2}$$

therefore, the approximate form used is only valid if:

$$\left(\frac{d\delta}{dx}\right)^2 \ll 1 \tag{4.3}$$

Lubrication theory, which is valid only if Equation (4.3) is satisfied, relates the mass flow rate in the thin film to the pressure gradient in the direction of flow:

$$\Gamma(x) = \frac{-1}{3v} \delta^3 \frac{d}{dx} P_l \tag{4.4}$$

where $\Gamma(x)$ is the mass flow rate and v is the kinematic viscosity. Equations (4.1) and (4.4) show that a given thin film shape, $\delta(x)$, gives rise to a given mass flow rate, $\Gamma(x)$.

Following Wayner [19], the evaporative flux is modelled according to the expression:

$$\dot{m} = a(T_{lv} - T_v) + b(P_l - P_v) \tag{4.5}$$

where

$\dot{m}$ is the evaporative flux, defined in the direction away from the film:

T_{lv} is the temperature of the liquid-vapor interface, and

T_v is the temperature of the vapor:

a and b are functions of the system temperature and physical properties and are defined as:

$$a = C\left(\frac{M}{2\pi RT_{lv}}\right)^{1/2}\left(\frac{P_v M \Delta h_m}{RT_v T_{lv}}\right) \tag{4.6}$$

$$b = C\left(\frac{M}{2\pi RT_{lv}}\right)^{1/2}\left(\frac{V_l P_v}{RT_{lv}}\right) \tag{4.7}$$

where

C is the accommodation coefficient taken to be 2.0;

M is the molecular weight of the evaporating material;

R is the universal gas constant;

P_v is the bulk vapor pressure of the evaporating material (e.g., uninfluenced by disjoining pressure, surface tension, etc.) at temperature T_v;

V_l is the molar volume of the bulk material at temperature T_{lv};

Δh_m is the enthalpy of vaporization of the material per unit mass, at temperature T_{lv}.

In practice the temperature T_{lv} is unknown; however, if the temperature differences between the substrate, vapor, and interface are small compared to the absolute temperature of the substrate, then the known substrate temperature, T_s, may be substituted for the unknown T_{lv}. Equation (4.5) says that evaporation is promoted by a superheat and hindered by low liquid film pressures. This model implies that the vapor phase does not present a significant

49

resistance to evaporation. The temperature of the liquid-vapor interface is related to the temperature of the substrate through the one-dimensional-conduction heat transfer solution for the film, valid if Equation (4.3) is satisfied.

$$\frac{k}{\delta} (T_s - T_{lv}) = \dot{m} \Delta h_m \qquad (4.8)$$

where k is the thermal conductivity of the liquid in the film. Following Moosman and Homsy [11], Equation (4.8) may be combined with (4.5) to eliminate T_{lv} in favor of T_s:

$$\dot{m} = \frac{1}{1 + \dfrac{a \Delta h_m}{k} \delta} [a(T_s - T_v) + b(P_l - P_v)] \qquad (4.9)$$

This equation clearly demonstrates the direct effect of film thickness on the evaporation rate. A recent numerical study by Stephan and Busse also demonstrated the importance of conductive resistance [58].

The local evaporation rate is linked to the flow rate in the film through a material balance:

$$\frac{d\Gamma}{dx} = -\dot{m} \qquad (4.10)$$

The coupled differential equations are thus Eq. (4.1) and:

$$\frac{1}{3v} \frac{d}{dx} \left(\delta^3 \frac{dP_l}{dx} \right) = \frac{1}{1 + \dfrac{a \Delta h_m}{k} \delta} [a\Delta T + b(P_l - P_v)] \qquad (4.11)$$

where:

$$\Delta T = T_s - T_v \qquad (4.12)$$

The variables are nondimensionalized in the following way. For reference, consider a strictly flat film:

$$\delta(x,t) = \delta_0 \qquad (4.13)$$

There is no pressure gradient in such a film according to Equation (4.1). Therefore the right-hand side of Equation (4.11) must be zero. Hence,

$$b(P_l - P_v) = -a\Delta T \qquad (4.14)$$

Combining this result with Equations (4.1) and (4.13) we find:

$$\frac{\dot{A}}{\delta_0^3} = -\frac{a}{b} \Delta T \qquad (4.15)$$

If δ_0 is so chosen, the flat film is a solution to the governing Equations (4.1, 4.11). The reference thickness is thus fixed and the reference pressure is the magnitude of the pressure of such a film. This pressure is given by (4.14) as:

$$\Pi_0 = \left(\frac{a}{b}\right) \Delta T \qquad (4.16)$$

The dimensionless pressure is defined as:

$$\phi = (P_l - P_v)/\Pi_0 \qquad (4.17)$$

The scaling of x is now stipulated by Equation (4.11) as:

$$l = \sqrt{\frac{-\dot{A}}{va\Delta T}} \qquad (4.18)$$

(Note: $\dot{A}$ is negative for a spreading film and $\dot{m}^{id} = a(T_s - T_v) = a\Delta T$, the ideal evaporative mass flux.)

The dimensionless position and film thickness are:

$$\xi \equiv x/l \qquad (4.19)$$

and:

$$\eta \equiv \delta/\delta_0 \qquad (4.20)$$

51

The dimensionless form of Equations (4.11) and (4.1) is:

$$\frac{1}{3} \frac{d}{d\xi} \left(\eta^3 \frac{d\phi}{d\xi} \right) = \frac{1}{1 + \kappa \eta} (1 + \phi) \qquad (4.21)$$

and:

$$\phi = -\frac{1}{\eta^3} - \varepsilon \frac{d^2\eta}{d\xi^2} \qquad (4.22)$$

where the parameters κ and ε are:

$$\kappa \equiv \frac{a\Delta h_m \delta_o}{k} \qquad (4.23)$$

and:

$$\varepsilon \equiv \frac{\sigma \delta_o b v}{-\dot{A}} \qquad (4.24)$$

The parameter κ is a measure of the importance of the resistance of the film to thermal conduction. The parameter ε is a measure of the importance of capillary pressure effects relative to disjoining pressure effects.

We impose two far field conditions . The first condition is for $\xi \rightarrow \infty$:

$$\eta \rightarrow 1 \qquad (4.25)$$

$$\phi \rightarrow -1 \qquad (4.26)$$

The film thickness is assumed to asymptotically approach the non-evaporating thin film thickness mentioned previously. The second condition is for $\xi \rightarrow -\infty$:

$$\eta \rightarrow \infty \qquad (4.27)$$

$$\phi \rightarrow -\phi_m \qquad (4.28)$$

52

NUMERICAL SOLUTION

The governing equations (4.21, 4.22) were transformed with the substitution:

$$\lambda \equiv \frac{\xi}{\sqrt{\varepsilon}} \tag{4.29}$$

to yield:

$$\frac{1}{3} \frac{d}{d\lambda} \left(\eta^3 \frac{d\phi}{d\lambda} \right) = \varepsilon \frac{1 + \phi}{1 + \kappa \eta} \tag{4.30}$$

and:

$$\phi = -\frac{1}{\eta^3} - \frac{d^2\eta}{d\lambda^2} \tag{4.31}$$

The far-field behavior described by Equations (4.25) and (4.26) may be further described by analysis of Equations (4.30) and (4.31) for η near 1 and ϕ near -1. The result is:

$$\eta \rightarrow 1 + \beta_0 \exp \left(-\lambda \sqrt{\frac{3\varepsilon}{\kappa + 1}} \right) + \beta_1 \exp \left(-\lambda\sqrt{3} \right) \tag{4.32}$$

and:

$$\phi \rightarrow -1 + 3\beta_0 \left(1 - \frac{\varepsilon}{\kappa + 1} \right) \exp \left(-\lambda \sqrt{\frac{3\varepsilon}{\kappa + 1}} \right) \tag{4.33}$$

as $\lambda \rightarrow \infty$.

This result provides four initial conditions to the Adams method NAG routine DO2CBF. As written these are more like "final conditions" than initial conditions; however, the independent variable in the code is actually $-\lambda$ and so Equations (4.32) and (4.33) provide initial conditions. A value of $-\lambda$ was chosen (typically -2.8),

53

$\eta, -\dfrac{d\eta}{d\lambda}, \phi$ and $-\dfrac{d\phi}{d\lambda}$ were calculated, and the routine was called. The value of $-\lambda$ must be sufficiently negative so that η is close enough to 1 and ϕ to -1 that the expressions (4.32) and (4.33) are a valid approximation of η and ϕ. The analytical expressions for $\dfrac{d\eta}{d\lambda}$ and $\dfrac{d\phi}{d\lambda}$ are simply the derivatives of η and ϕ. Therefore, the solutions η and ϕ are functions of ϵ, κ, β_0, and β_1.

The numerical solution was compared to the experimental results in the following way. The flat portion of the film, δ_0, was measured with Ellipsometry. Using the measurement of δ_0, κ was calculated with Equation (4.23). A value of ϵ was selected and then the ratio of β_0 to β_1 was varied while one of them (typically β_1) was held constant. This ratio β_0/β_1 was varied until the two end points of the data were matched by the numerical result. If the value of ϵ was too large the numerical solution curved too much relative to the data (the points between the end points), lagging below. If the value of ϵ was too small the numerical solution was too straight and the data between the end points lagged below the solution. In this way the "best" value of ϵ was selected. The reason β_1 was held constant is that the solutions η and ϕ are invariant with respect to translation of λ, as shown by Equations (4.30) and (4.31). That is if $\phi(\lambda)$ satisfies (4.30, 4.31) so does $\phi(\lambda + c)$ where c is any constant. The computer program is given in Appendix C. The comparison between data and model was performed on a dimensional basis and is pictured in Figures 4.2 to 4.24. In these results, Q is the power input setting, δ_0 is the measured value, κ depends on δ_0, and ϵ is the value of the unknown being determined.

54
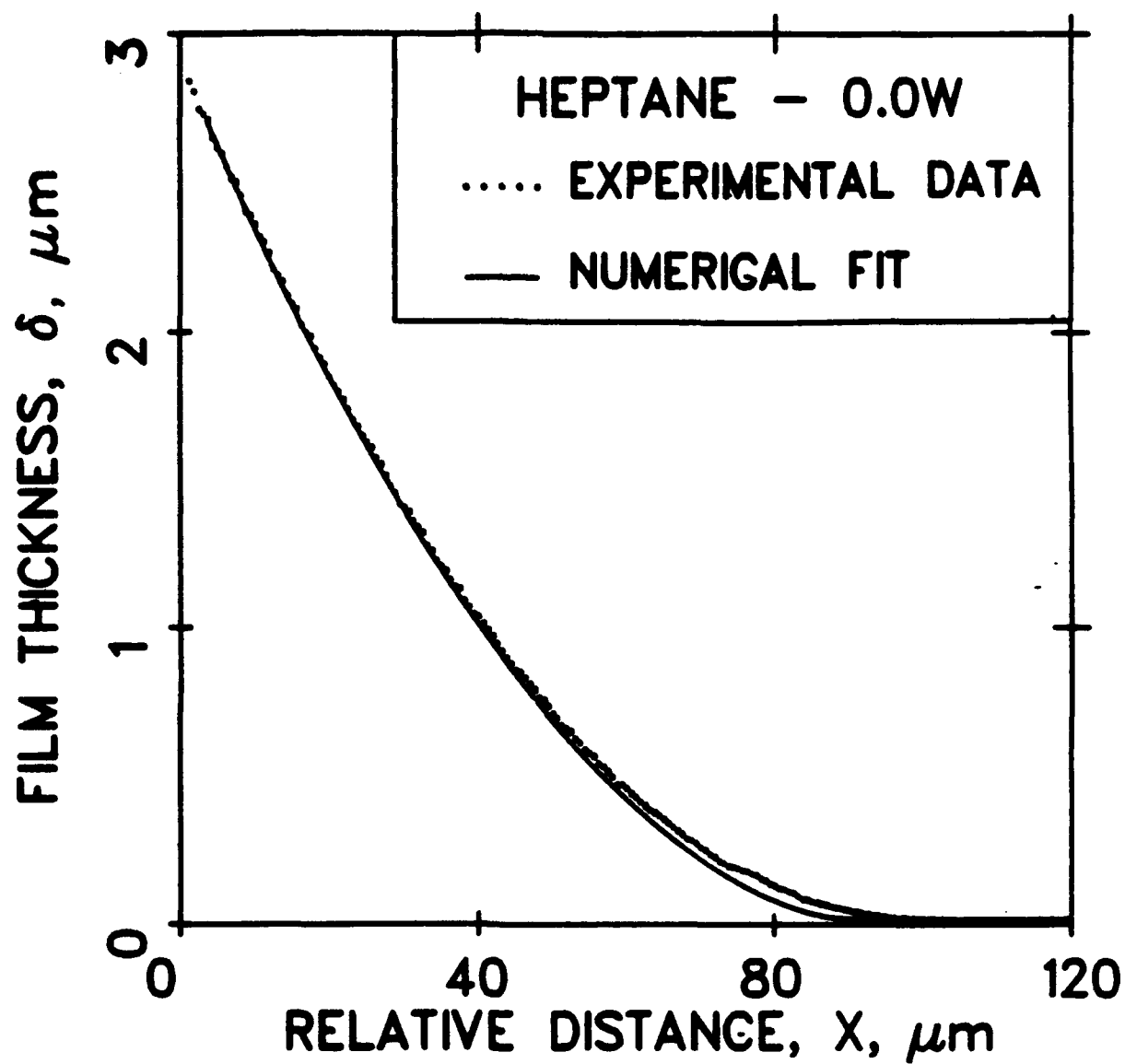
Figure 4.2   Comparison of Theory and Experiments
(Q = 0.0W, δ_0 = 15 nm, κ = 6.48 x 10^{-2}, ε = 2.5,
β_0 = -1.800 X 10^{-4}, β_1 = 1..0 X 10^{-2}).
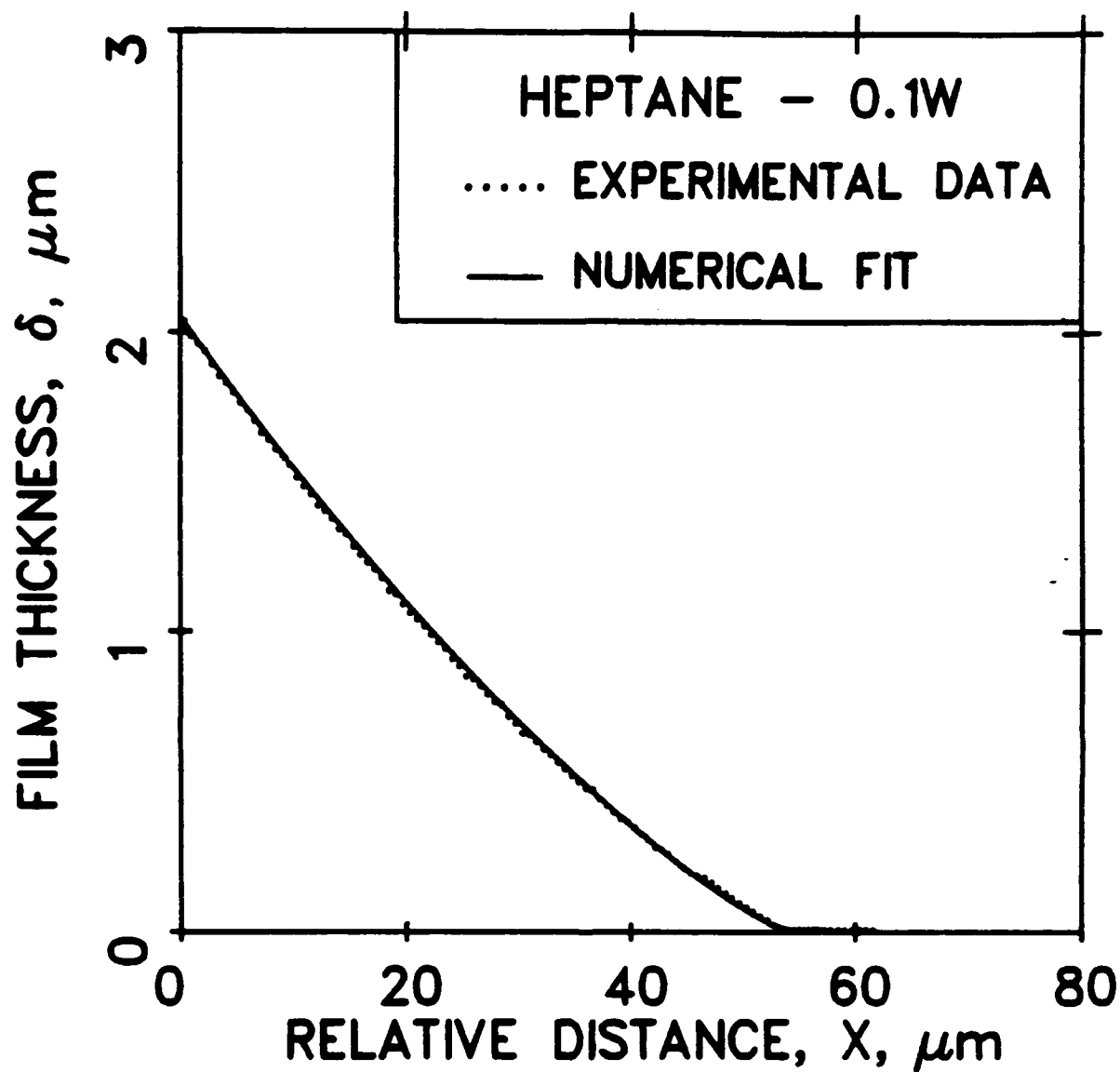
Figure 4.3   Comparison of Theory and Experiments
(Q = 0.1W, δ_0 = 6.4 nm, κ = 2.771 x 10^{-2}, ε = 1.1,
β_0 = -6.930 X 10^{-3}, β_1 = 1.0 X 10^{-2}).

56

Figure 4.4   Comparison of Theory and Experiments
(Q = 0.2W, δ_0 = 6.2 nm, κ = 2.678 x 10^{-2}, ε = 1.5,
β_0 = -1.712 X 10^{-3}, β_1 = 1.0 X 10^{-2}).

Figure 4.5   Comparison of Theory and Experiments
(Q = 0.3W, δ_o = 5.9 nm, κ = 2.554 x 10^{-2}, ε = 1.1,
β_o = -6.858 X 10^{-3}, β_1 = 1.0 X 10^{-2}).

Figure 4.6   Comparison of Theory and Experiments
($Q = 0.5W$, $\delta_0 = 5.65$ nm, $\kappa = 2.440 \times 10^{-2}$, $\varepsilon = 1.05$,
$\beta_0 = -8.645 \times 10^{-3}$, $\beta_1 = 1.0 \times 10^{-2}$).
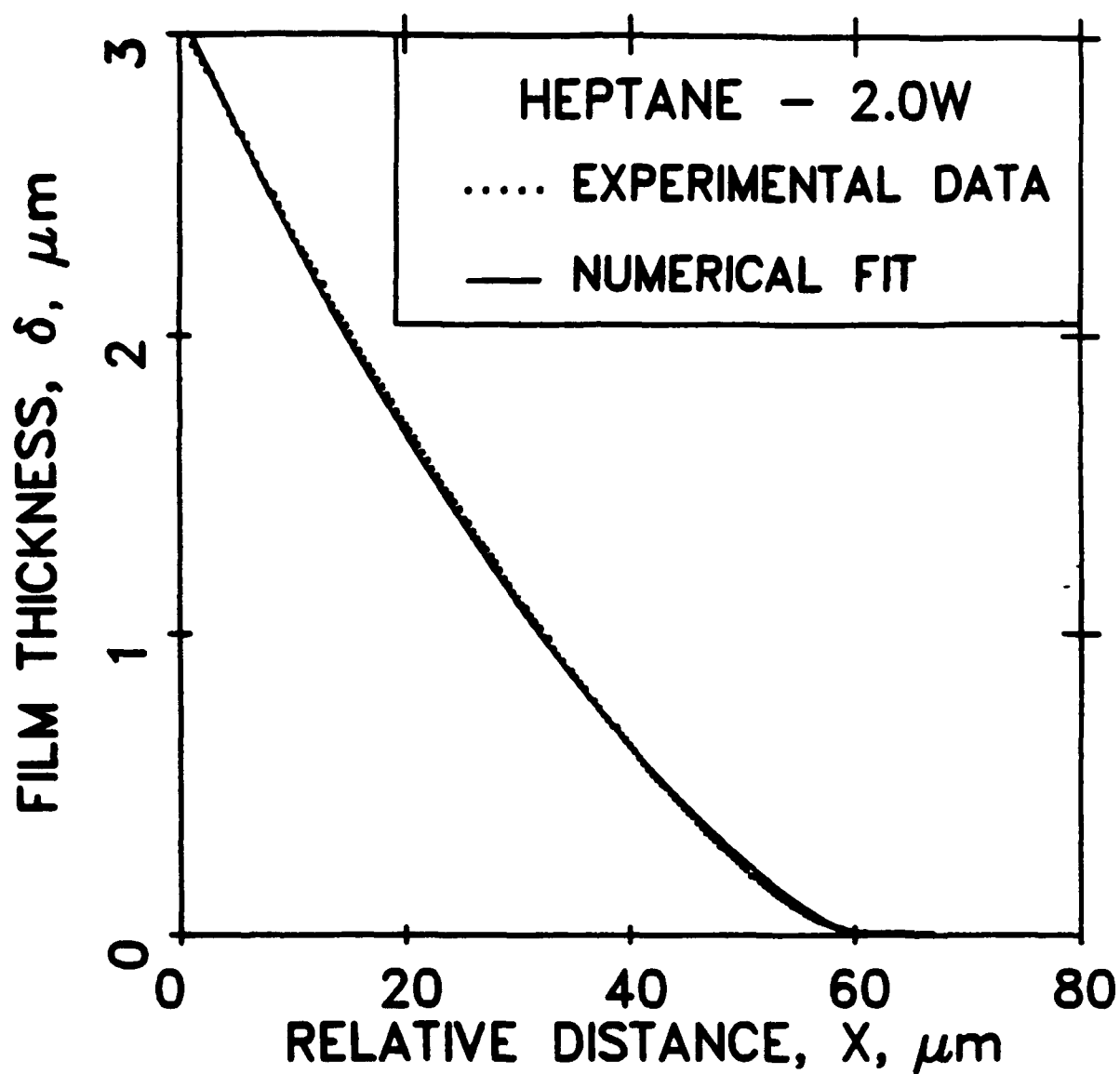
Figure 4.7   Comparison of Theory and Experiments
(Q = 2.0W, δ_o = 4.8 nm, κ = 3.265 x 10^{-2}, ϵ = 3.5,
β_o = -3.310 X 10^{-5}, β_1 = 1.0 X 10^{-2}).
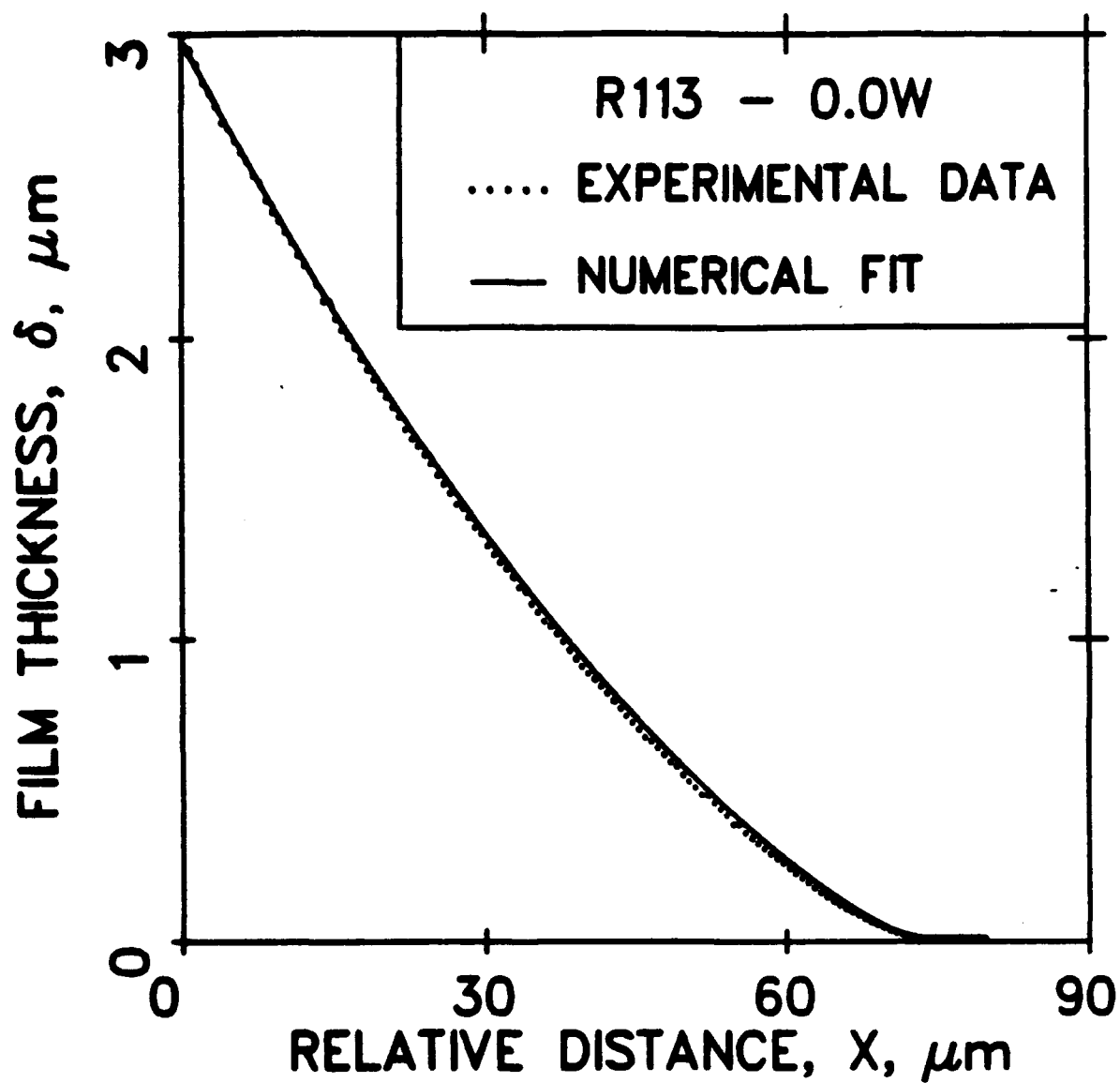
Figure 4.8 Comparison of Theory and Experiments
(Q = 0.0W, δ_0 = 11.5 nm, κ = 2.86 x 10^{-1}, ϵ = 6.0,
β_0 = -6.900 X 10^{-6}, β_1 = 1.0 X 10^{-2}).
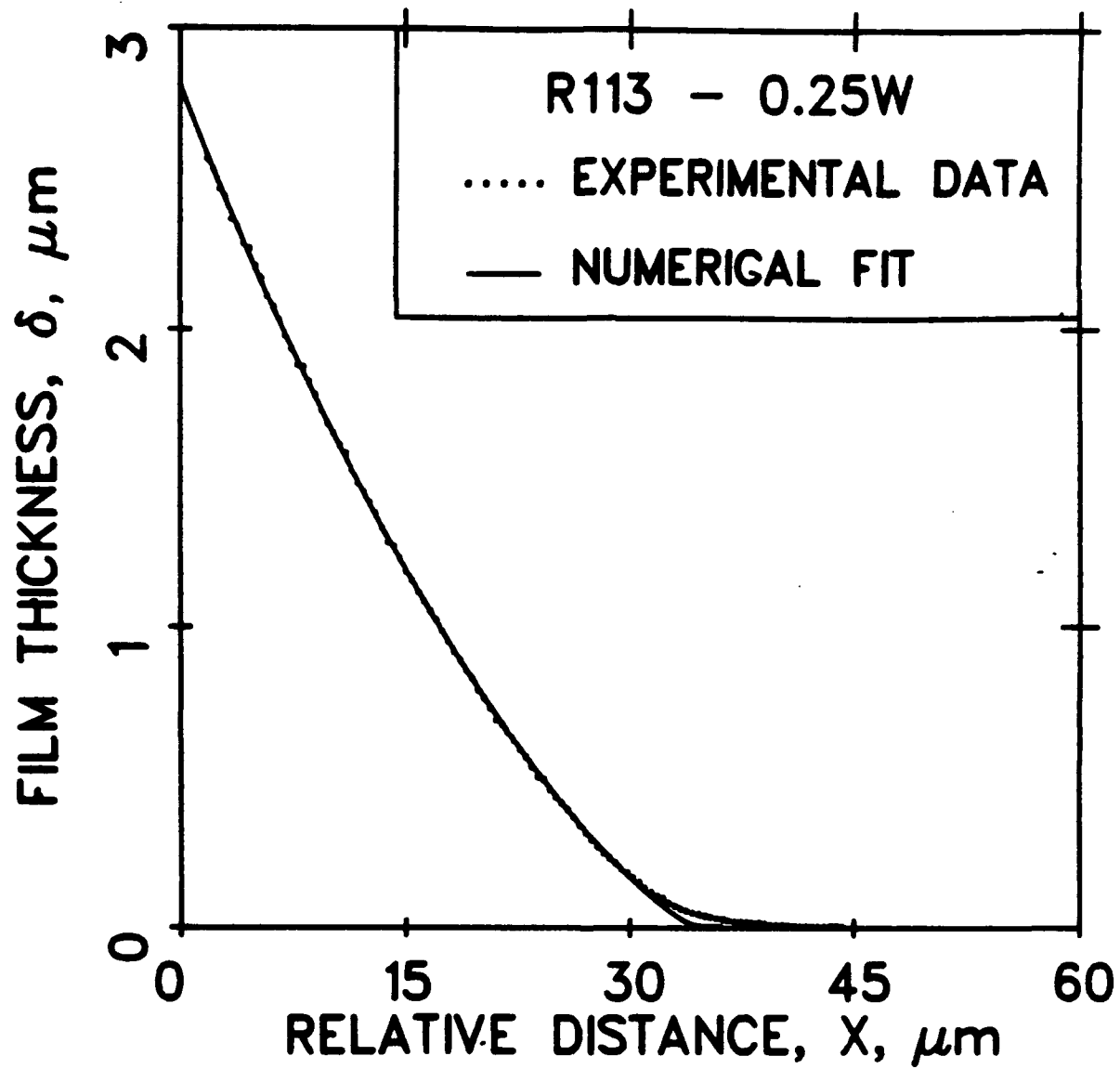
Figure 4.9   Comparison of Theory and Experiments
(Q = 0.25W, δ_0 = 4.8 nm, κ = 1.194 x 10^{-1}, ϵ = 5.5,
β_0 = -4.500 X 10^{-6}, β_1 = 1.0 X 10^{-2}).
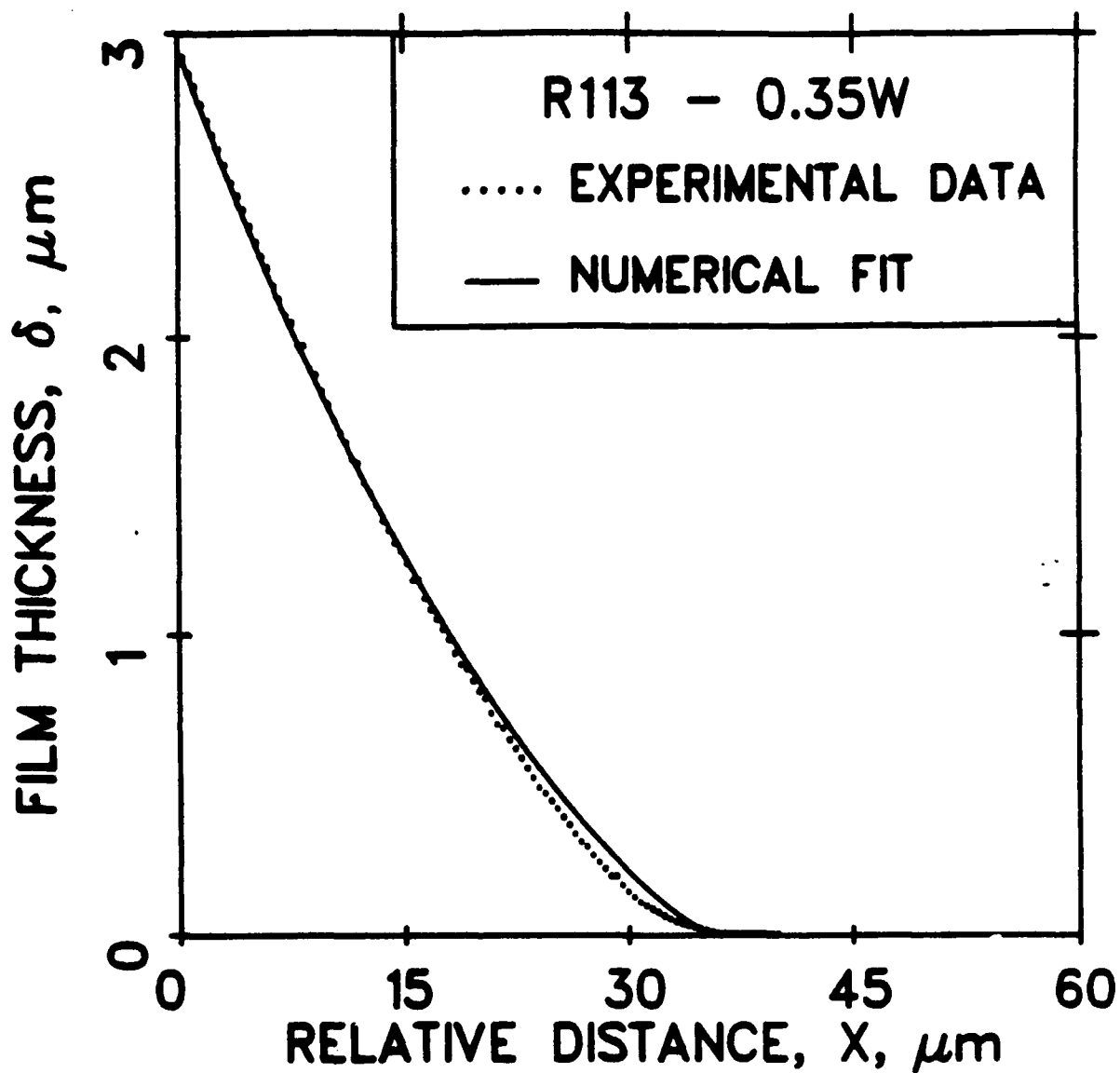
Figure 4.10   Comparison of Theory and Experiments
(Q = 0.35W, δ_o = 4.5 nm, κ = 1.193 x 10^{-1}, ϵ = 8.0,
β_o = -3.950 x 10^{-7}, β_1 = 1.0 X 10^{-2}).
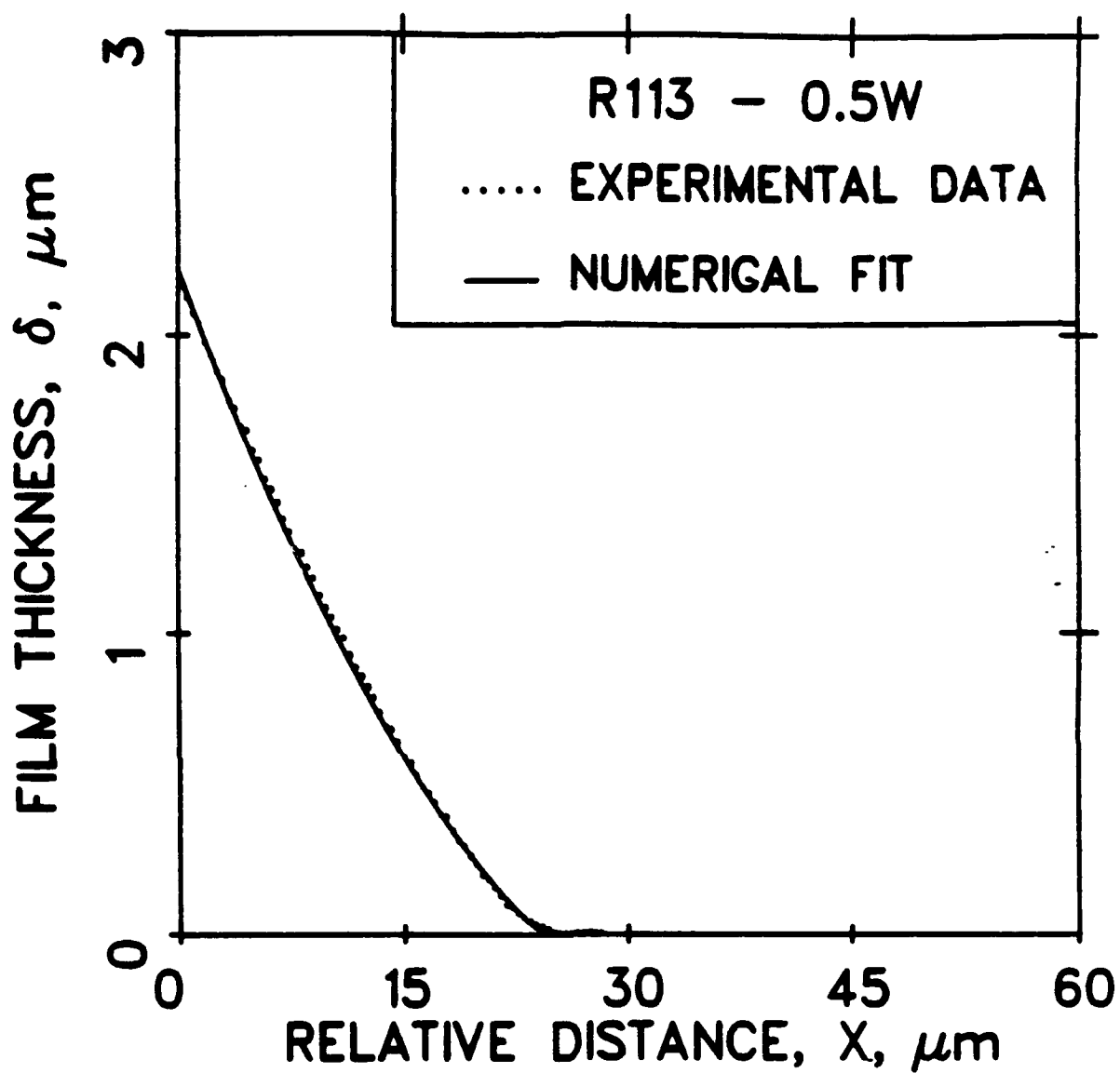
Figure 4.11   Comparison of Theory and Experiments
(Q = 0.5W, δ_0 = 4.0 nm, κ = 1.12 x 10^{-1}, ϵ = 4.0,
β_0 = -2.630 x 10^{-5}, β_1 = 1.0 X 10^{-2}).
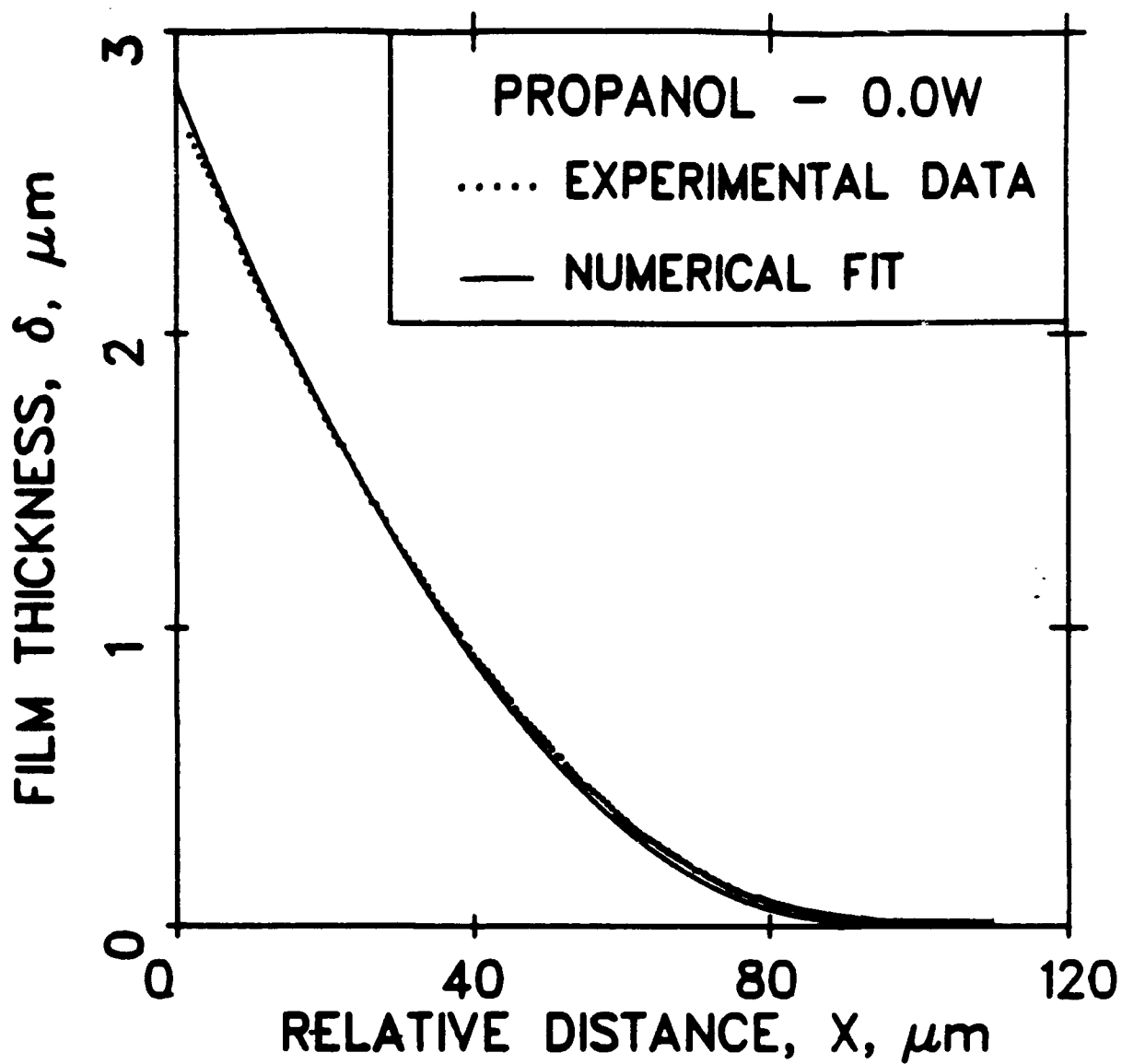
Figure 4.12   Comparison of Theory and Experiments
(Q = 0.0W, δ_0 = 13.6 nm, κ = 4.74 x 10^{-2}, ϵ = 5.5,
β_0 = -4.500 x 10^{-7}, β_1 = 1.0 X 10^{-2}).

65
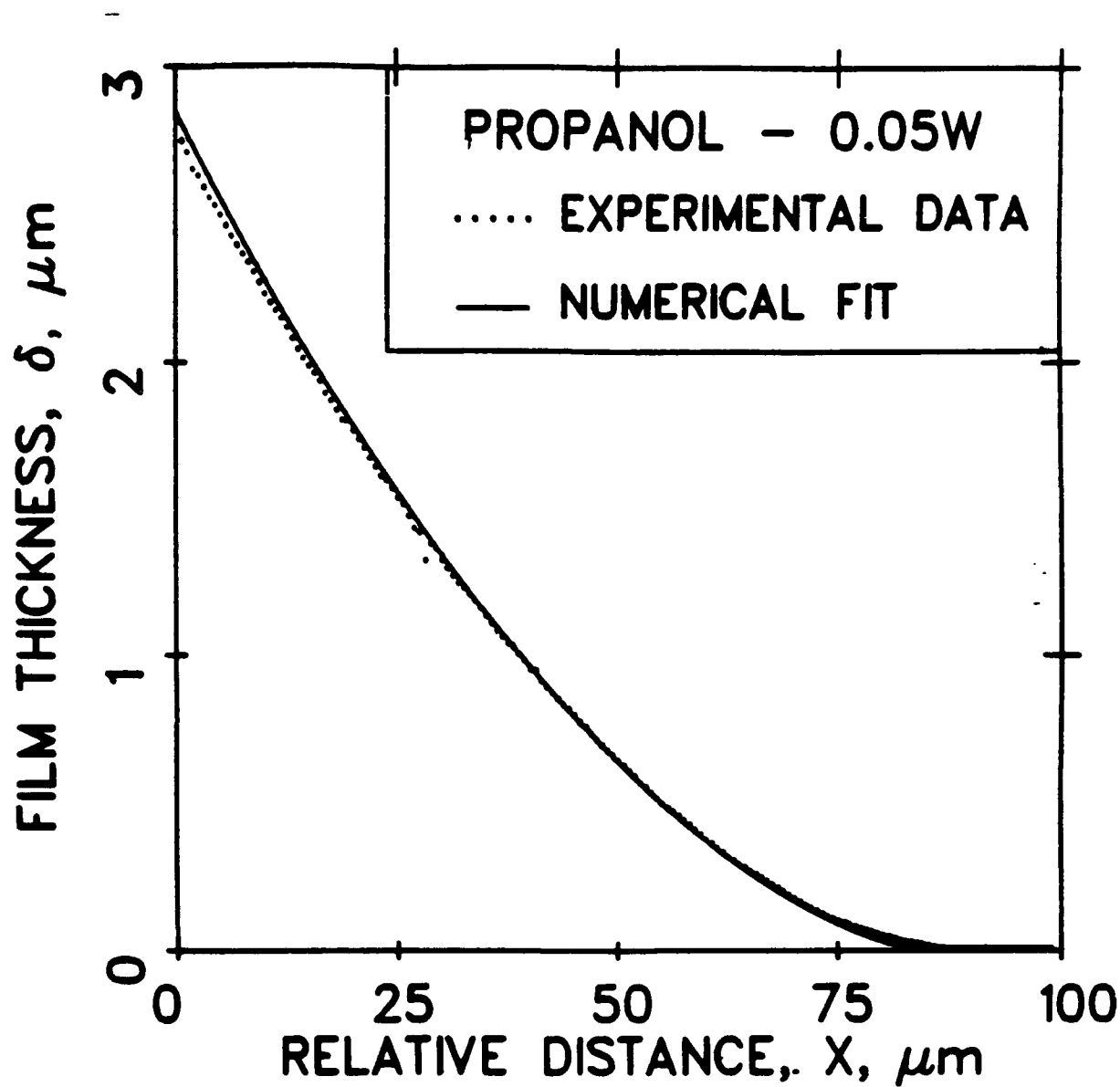
Figure 4.13   Comparison of Theory and Experiments
(Q = 0.05W, δ_0 = 6.5 nm, κ = 2.26 x 10^{-2}, ϵ = 5.5
β_0 = -2.100 x 10^{-6}, β_1 = 1.0 X 10^{-2}).
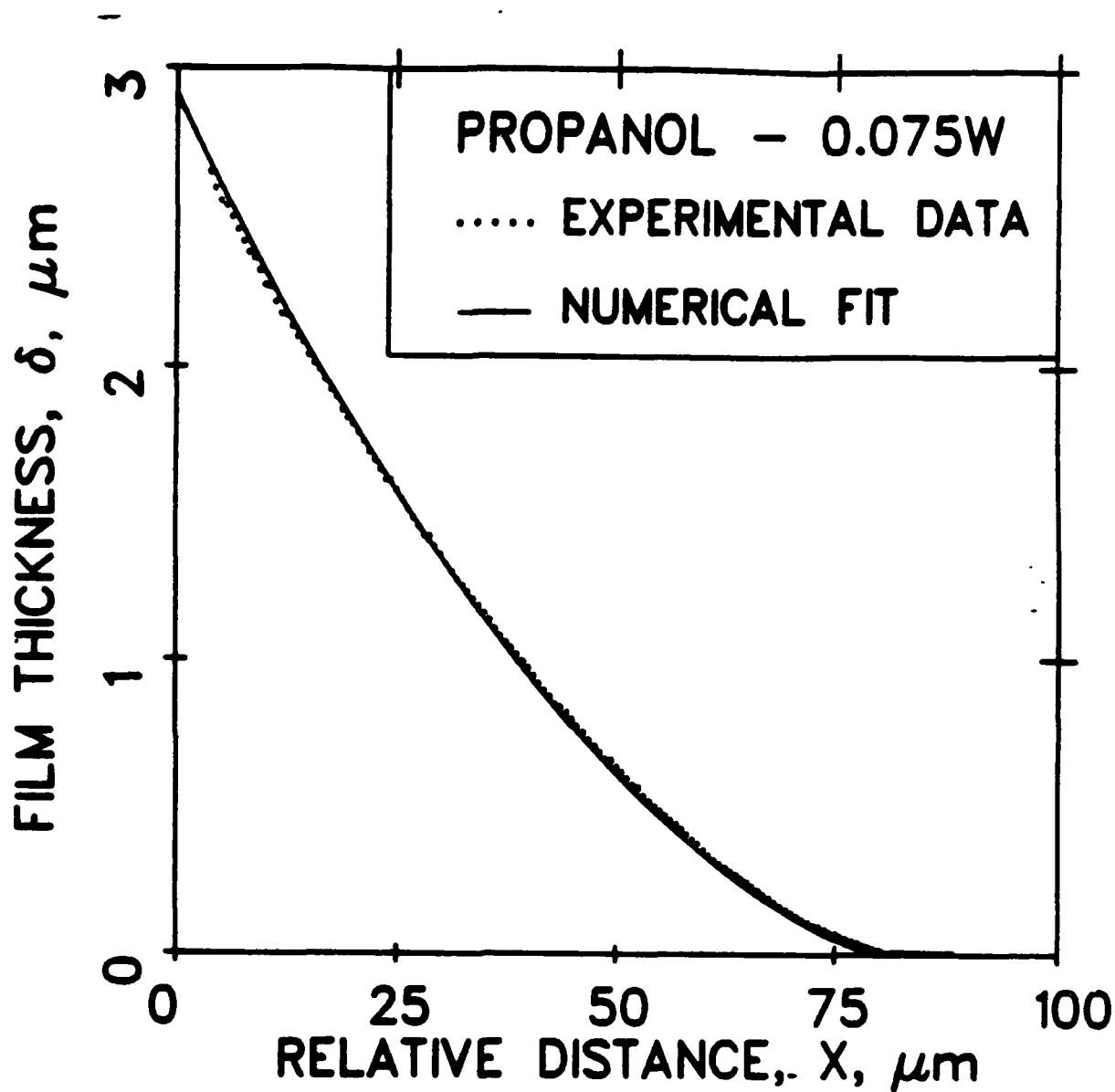
Figure 4.14   Comparison of Theory and Experiments
(Q = 0.075W, δ_0 = 5.2 nm, κ = 1.81 x 10^{-2}, ε = 5.5
β_0 = -2.100 x 10^{-6}, β_1 = 1.0 X 10^{-2}).
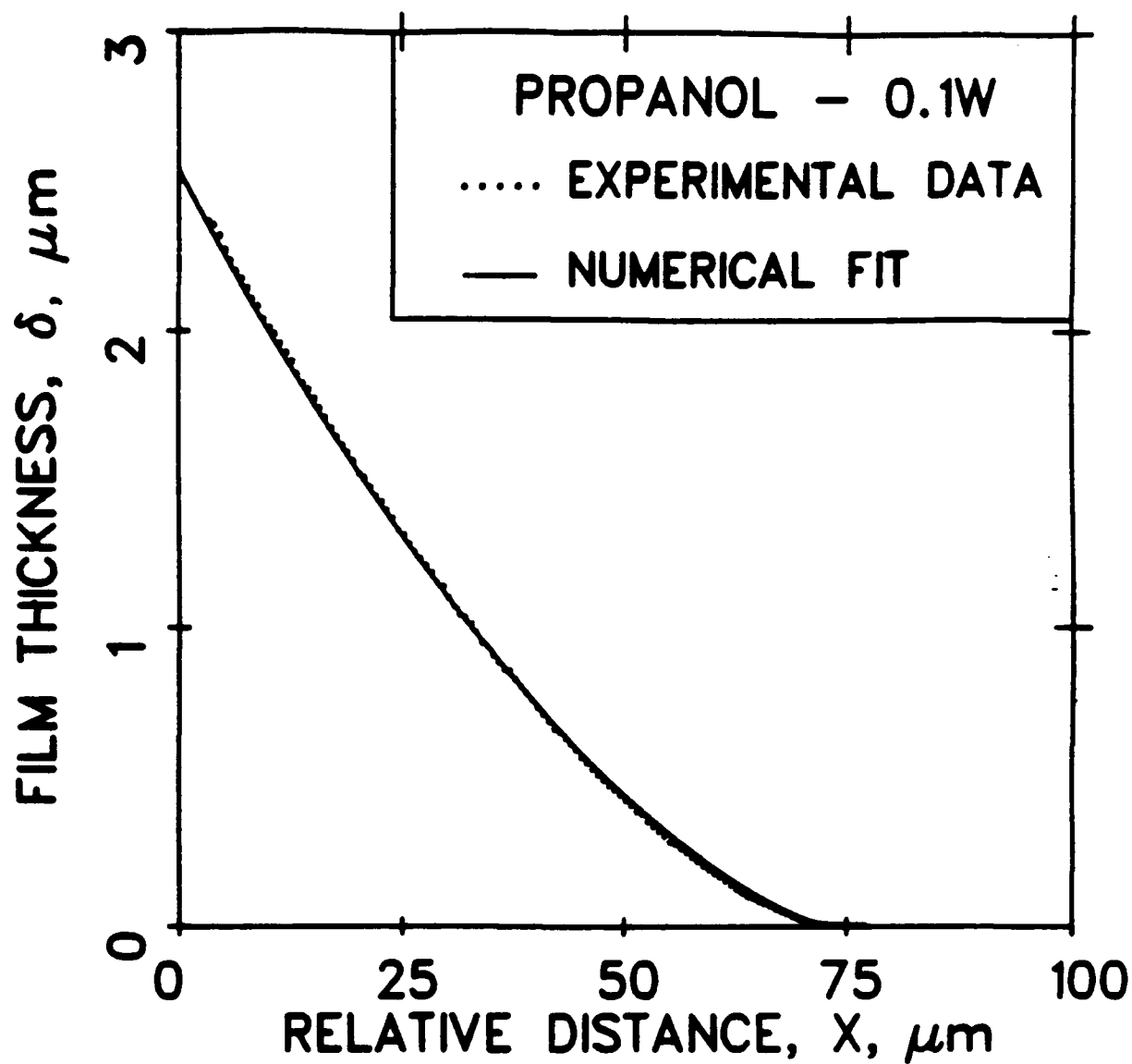
Figure 4.15   Comparison of Theory and Experiments
(Q = 0.1W, δ_o = 4.7 nm, κ = 1.64 x 10^{-2}, ε = 5.5)
β_o = -2.100 x 10^{-6}, β_1 = 1.0 X 10^{-2}).
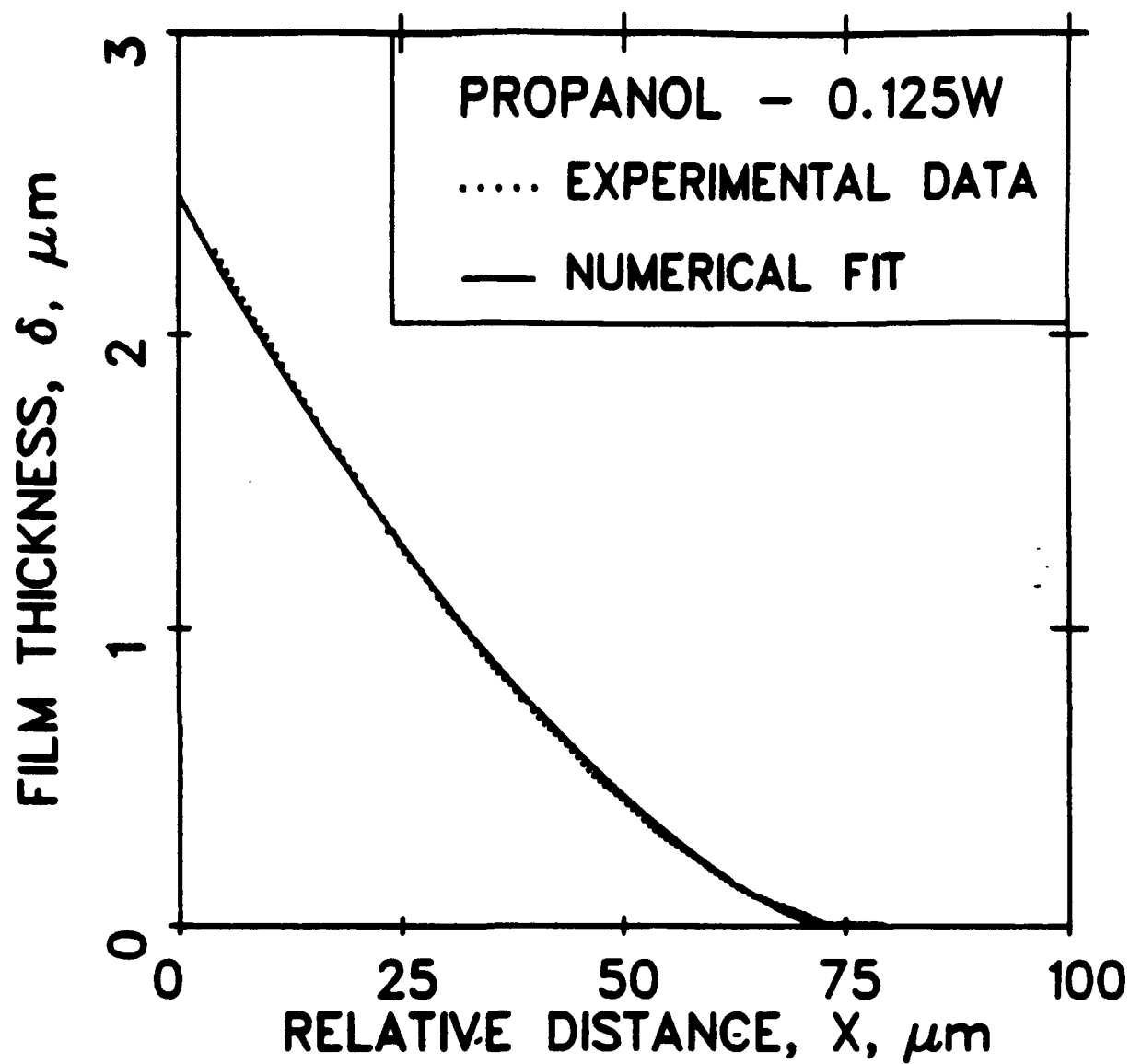
Figure 4.16   Comparison of Theory and Experiments
(Q = 0.125W, δ_o = 4.4 nm, κ = 1.53 x 10^{-2}, ϵ = 5.5
β_o = -2.100 x 10^{-6}, β_1 = 1.0 X 10^{-2}).
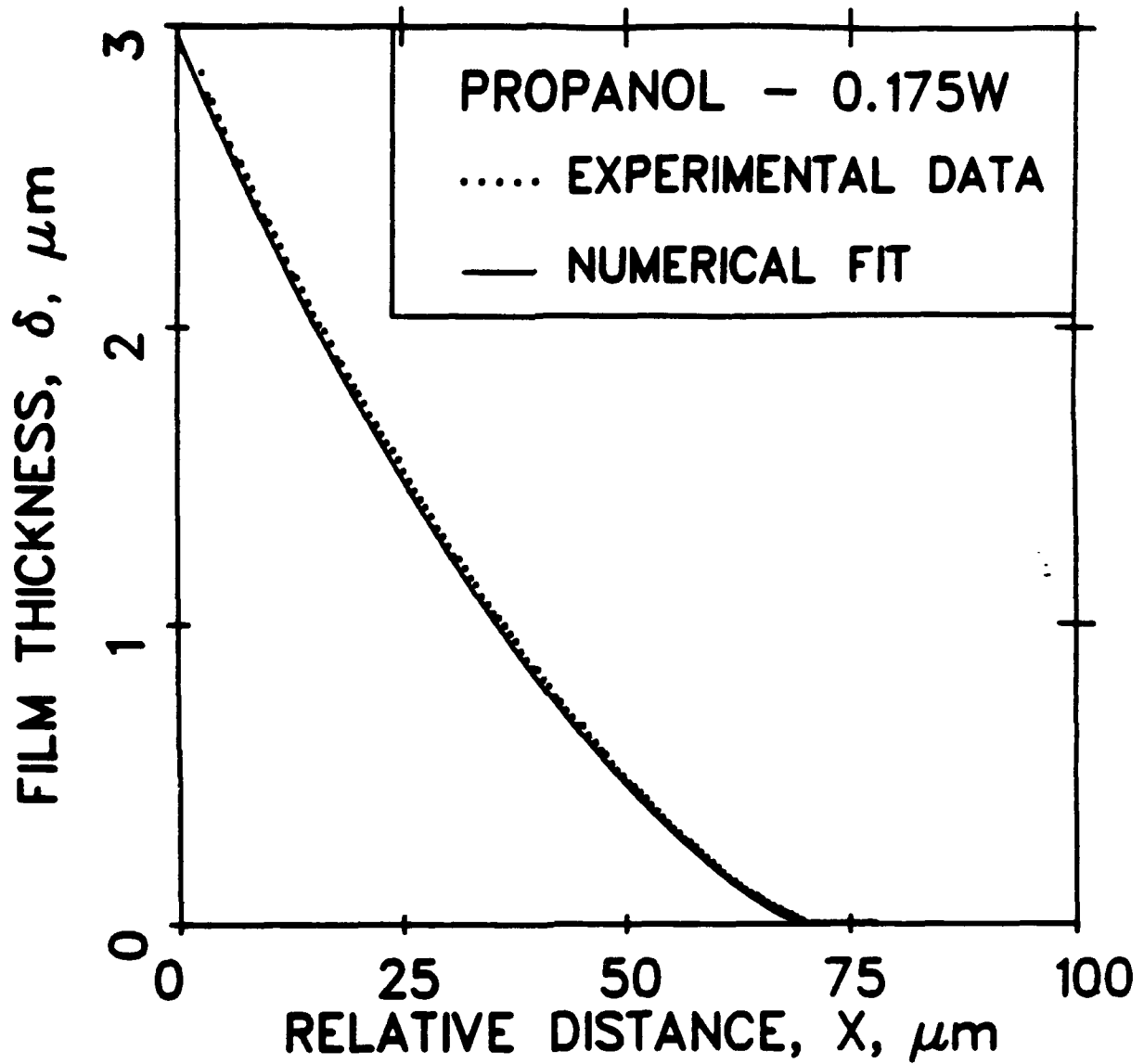
Figure 4.17   Comparison of Theory and Experiments
(Q = 0.175W, δ_0 = 3.6 nm, κ = 1.44 x 10^{-2}, ε = 5.5
β_0 = -2.100 x 10^{-6}, β_1 = 1.0 X 10^{-2}).

70
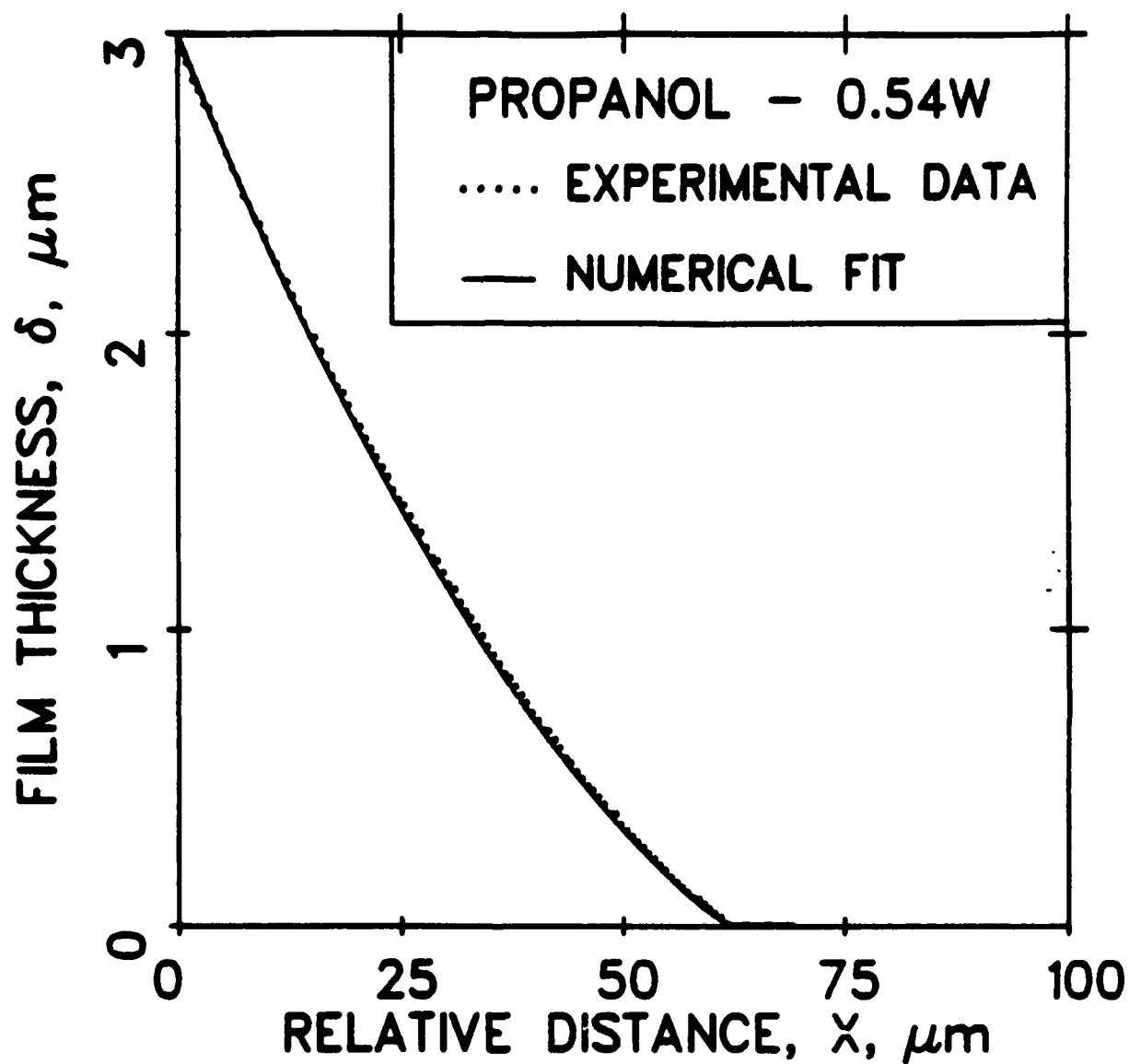
Figure 4.18 Comparison of Theory and Experiments
(Q = 0.54W, δ_0 = 2.9 nm, κ = 1.36 x 10^{-2}, ε = 5.0
β_0 = -3.825 x 10^{-6}, β_1 = 1.0 X 10^{-2}).

71
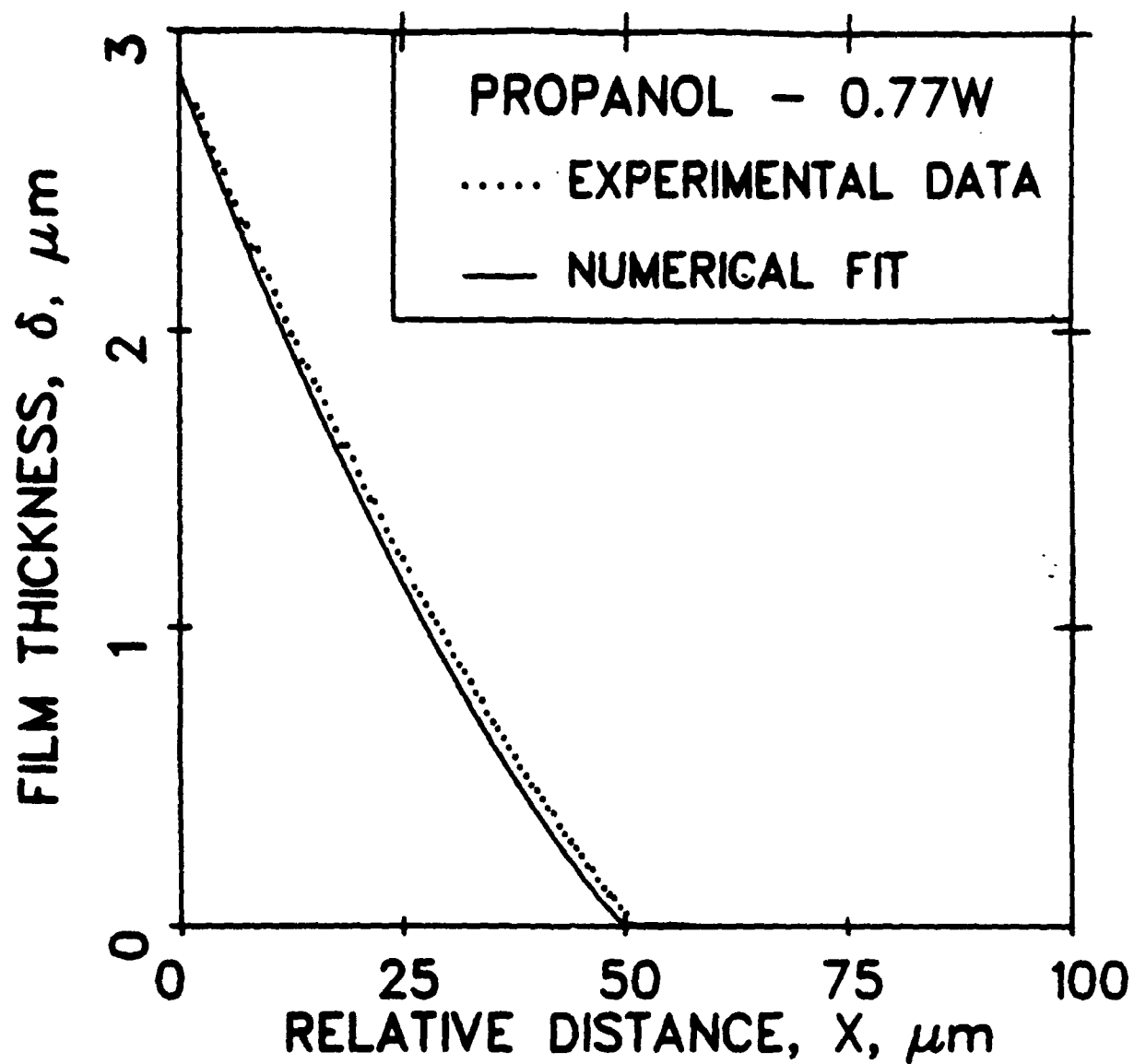
Figure 4.19   Comparison of Theory and Experiments
(Q = 0.77W, δ_0 = 2.7 nm, κ = 1.41 x 10^{-2}, ε = 1.8
β_0 = -7.285 x 10^{-4}, β_1 = 1.0 X 10^{-2}).

72
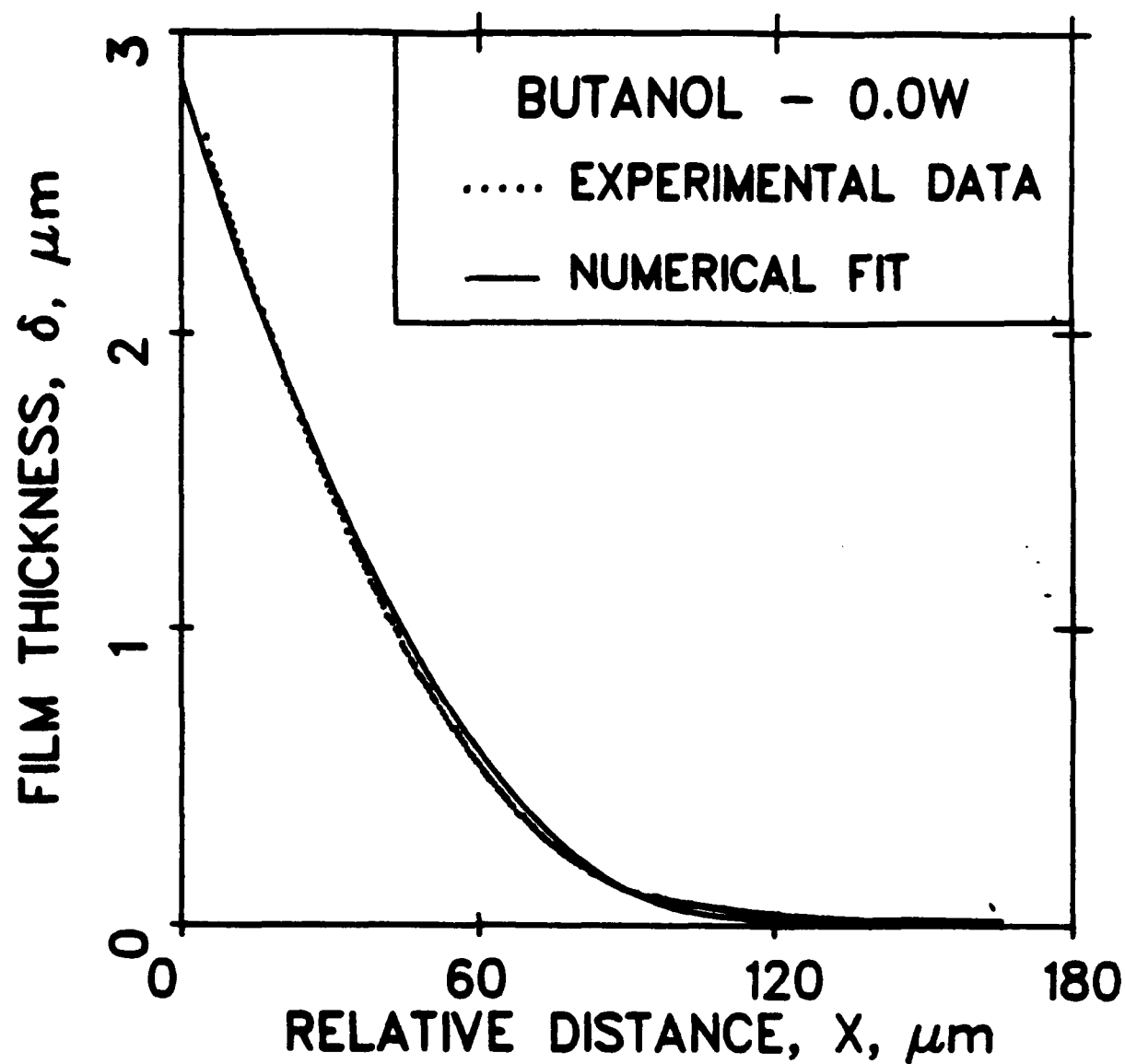
Figure 4.20   Comparison of Theory and Experiments
($Q = 0.0W$, $\delta_0 = 17.2$ nm, $\kappa = 1.652$ x 10^{-2}, $\epsilon = 11.0$
$\beta_0 = 1.000$ x 10^{-7}, $\beta_1 = 1.0$ X 10^{-2}).
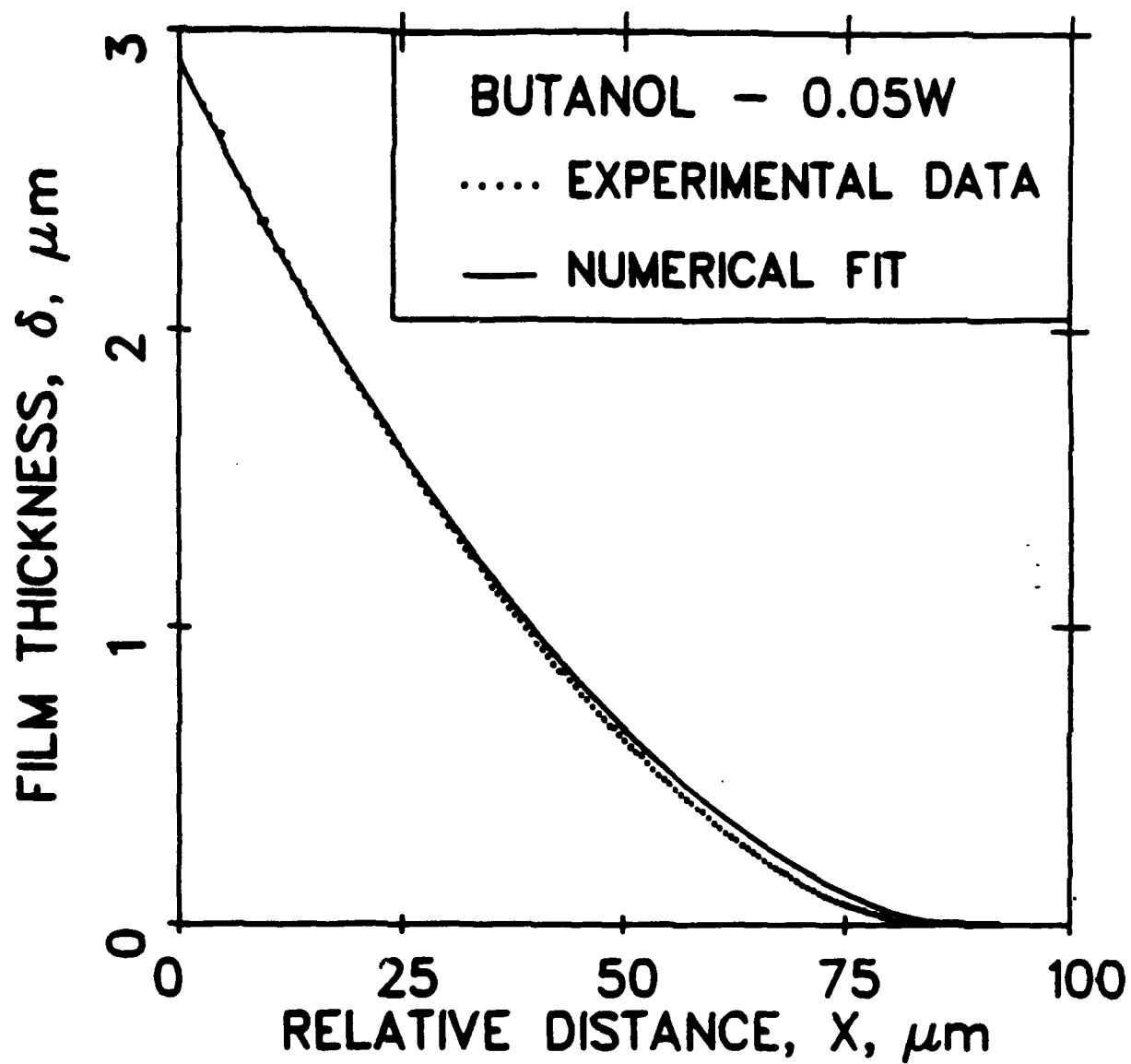
Figure 4.21   Comparison of Theory and Experiments
(Q = 0.05W, δ_0 = 5.9 nm, κ = 6.063 x 10^{-3}, ε = 5.0,
β_0 = -3.300 x 10^{-6}, β_1 = 1.0 X 10^{-2}).
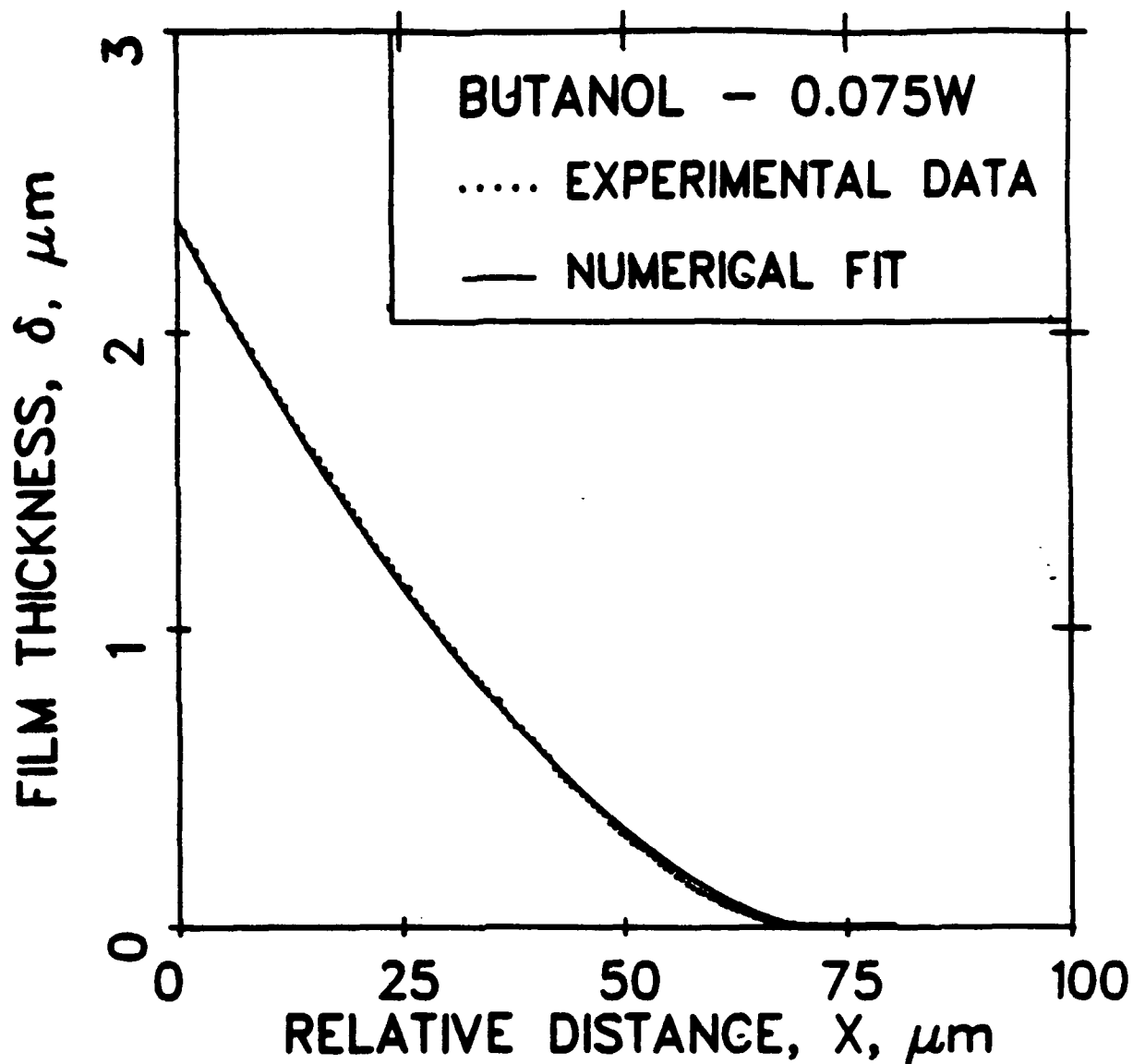
Figure 4.22   Comparison of Theory and Experiments
(Q = 0.075W, δ_0 = 5.4 nm, κ = 5.546 x 10^{-3}, ϵ = 3.5,
β_0 = -2.670 x 10^{-5}, β_1 = 1.0 X 10^{-2}).
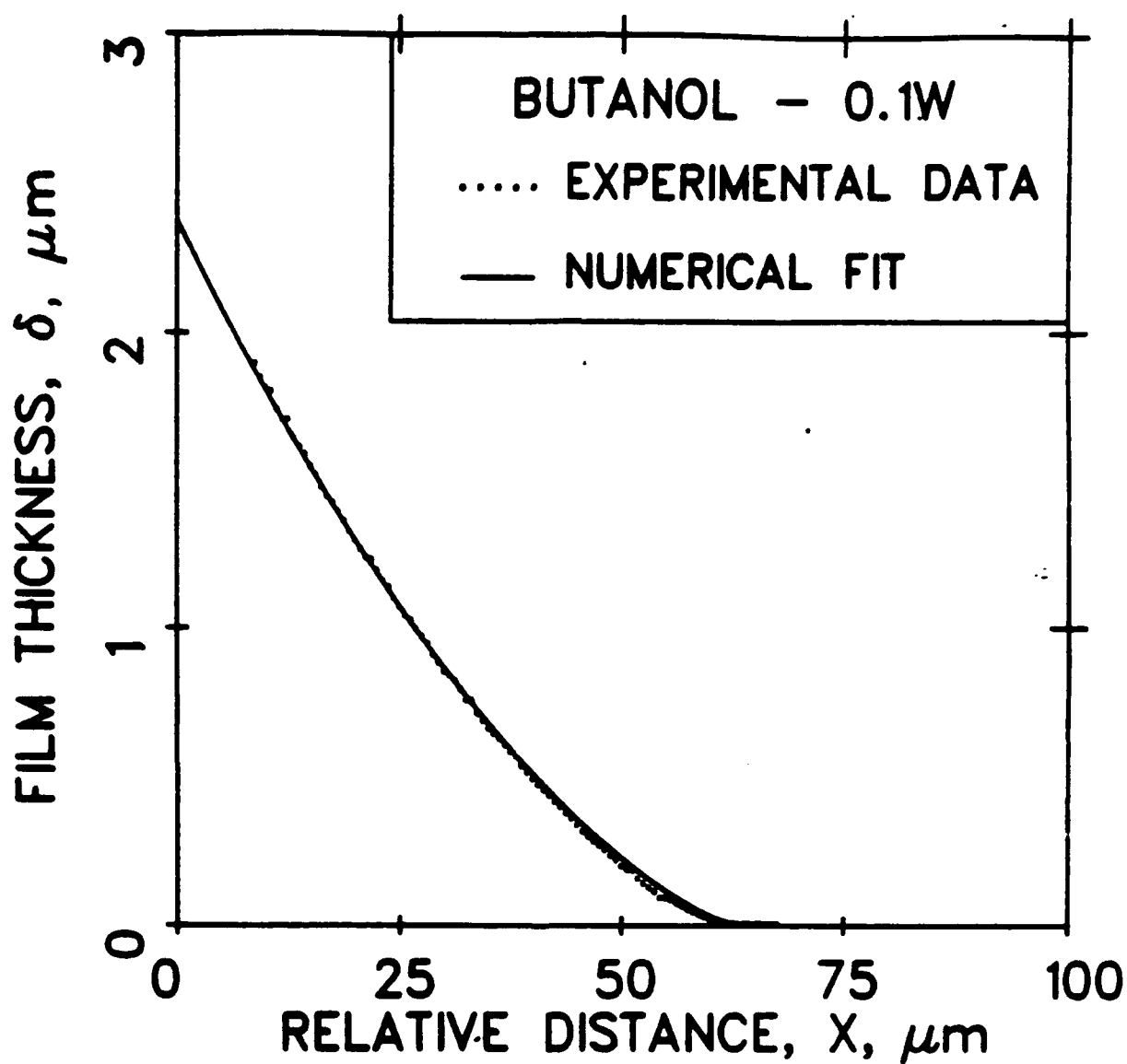
Figure 4.23   Comparison of Theory and Experiments
(Q = 0.1W, δ_0 = 4.9 nm, κ = 5.026 x 10^{-3}, ε = 2.25,
β_0 = -2..475 x 10^{-4}, β_1 = 1.0 X 10^{-2}).
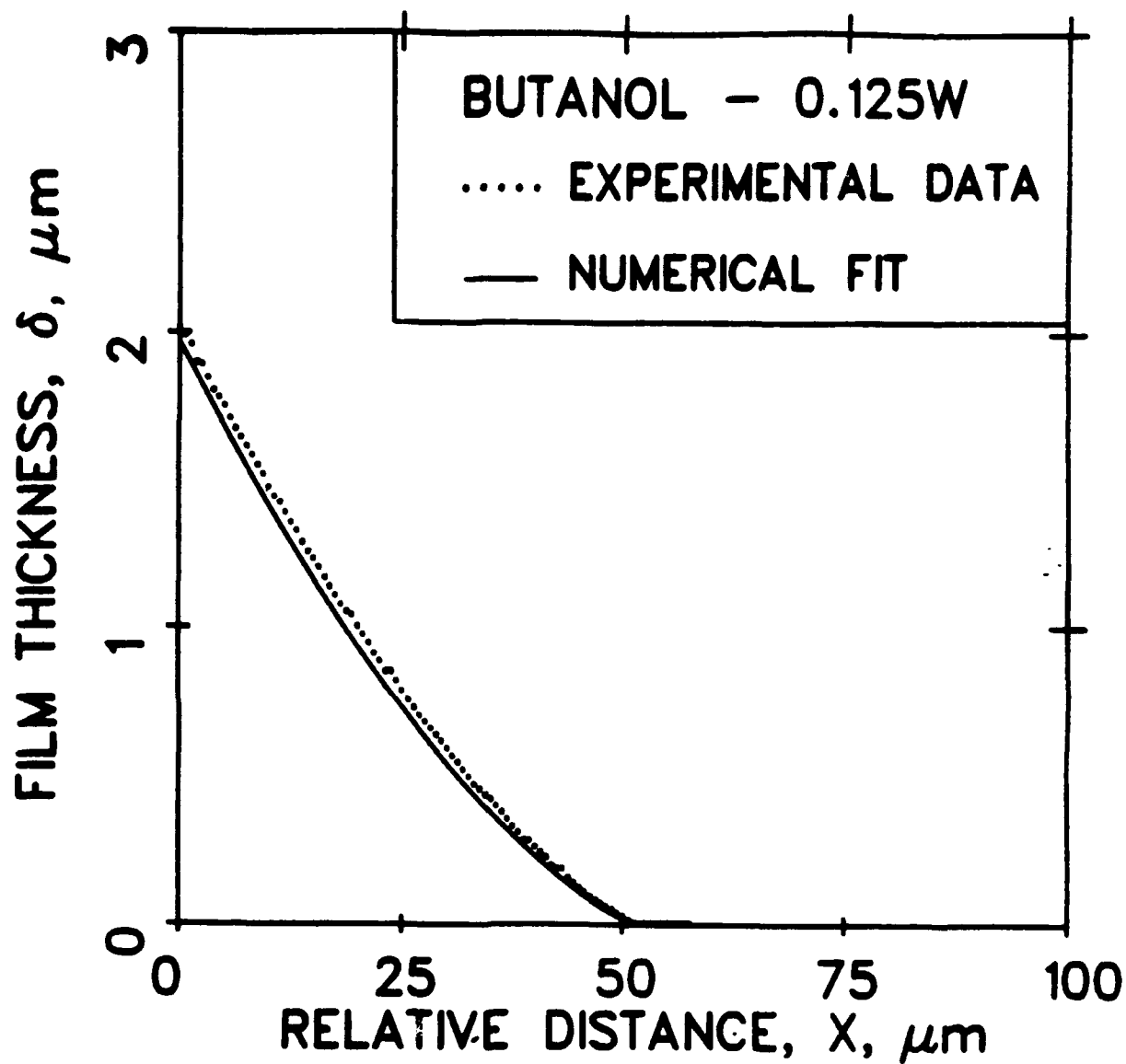
Figure 4.24   Comparison of Theory and Experiments
$(Q = 0.125W, \delta_0 = 4.5 \text{ nm}, \kappa = 4.815 \times 10^{-3}, \varepsilon = 1.8,$
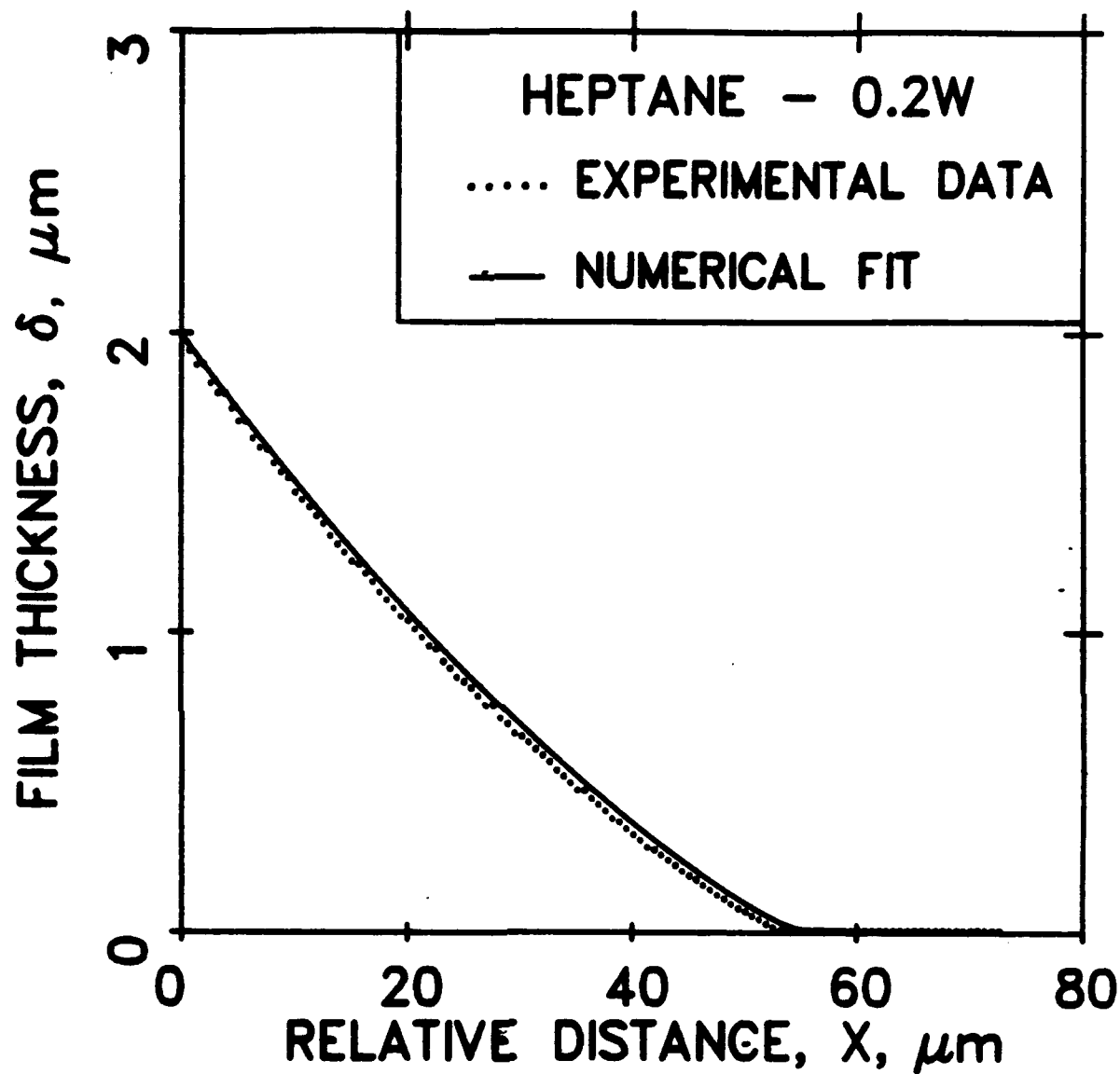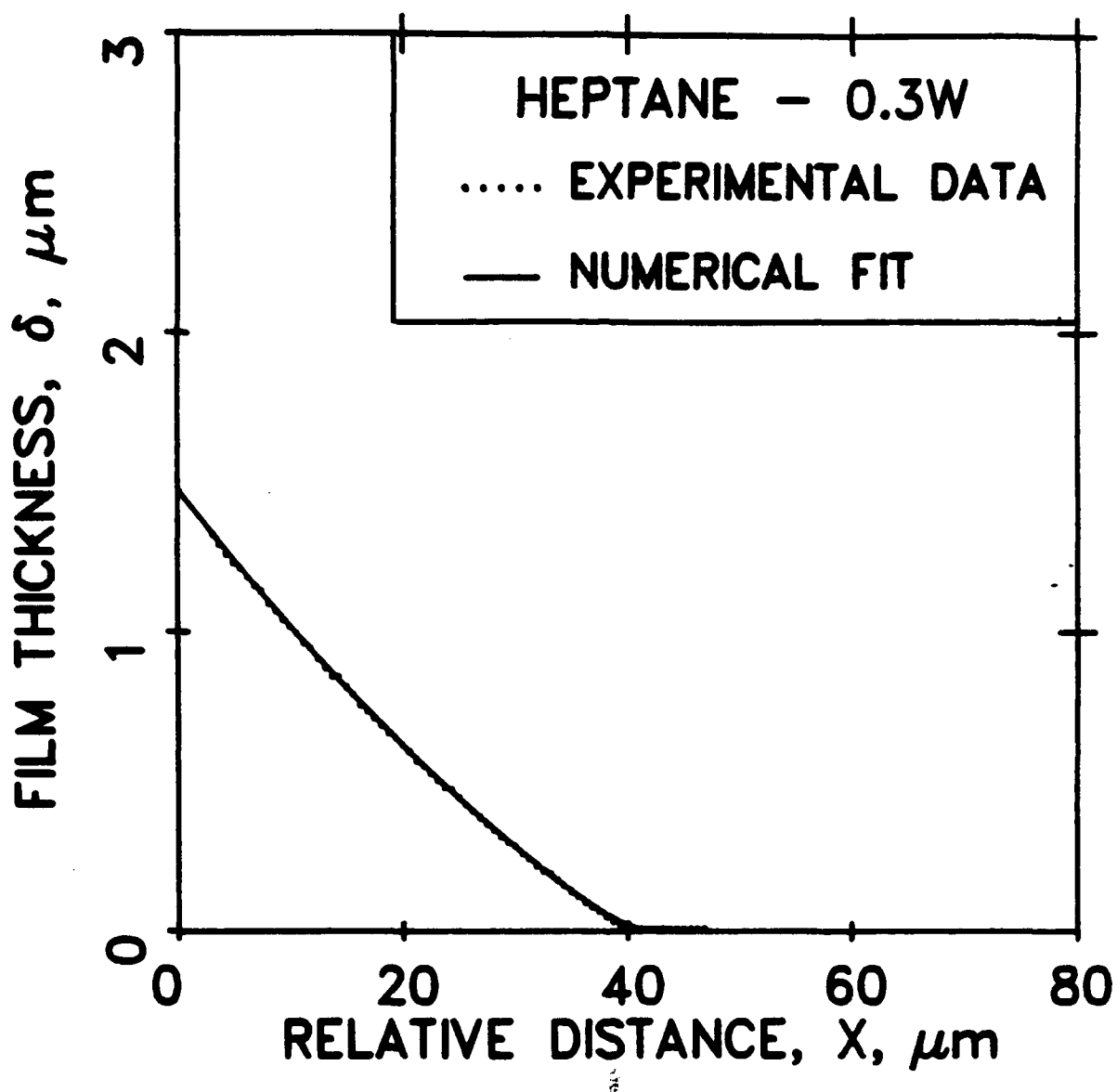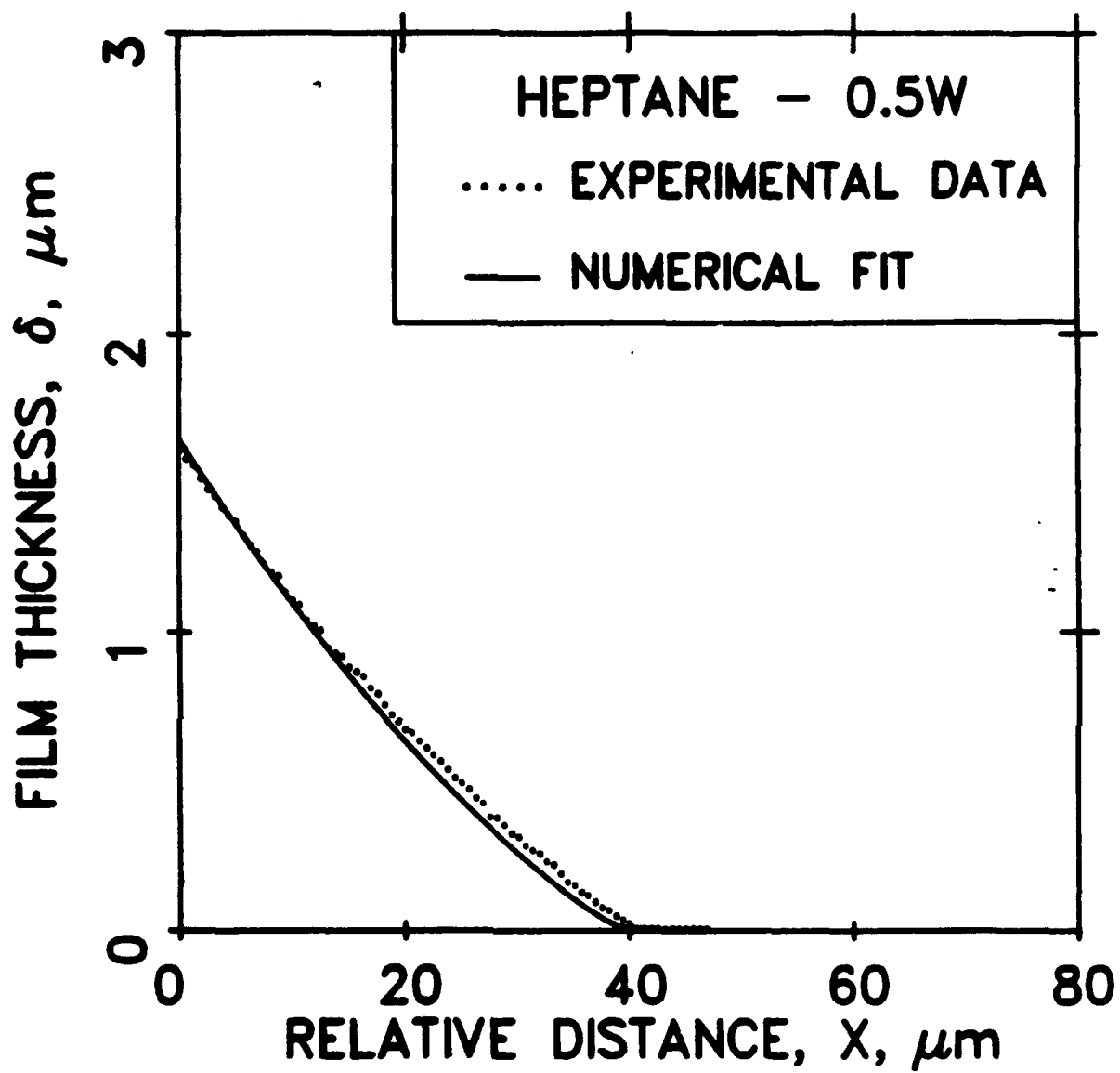$\beta_0 = -6.870 \times 10^{-4}, \beta_1 = 1.0 \times 10^{-2}).$

77

In Table 4.1 values of δ_0, ϵ, $-A$, $\dot{m}^{id}$, q^{id}, $(T_s - T_v)$, T_s are given for the data presented in Figures 4.2-4.24. The values of $-A$ were obtained using Equation (4.24.) The values of $\Delta T = (T_s - T_v)$ were obtained using Equation (4.15) and the values of T_{lv} taken to be approximated by T_s. The values of $\dot{m}^{id}$ and q^{id} were obtained using:

$$\dot{m}^{id} = a\Delta T \tag{4.34}$$

$$q^{id} = a\Delta T \, \Delta h_m \tag{4.35}$$

We note that the values of ΔT are extremely small; too small to be experimentally measured. We also note the correct trend in δ_0 and q^{id} with power input; as the power input increases, δ_0 decreases and q^{id} increases. We further note that, at the highest power studied, the contact line thickness, δ_0, is still substantially greater than a monolayer. Higher fluxes were limited by the experimental design. Therefore, additional studies at higher fluxes with an improved design are recommended.

The right-hand side of Eq. (4.21) is also the dimensionless mass flux at the liquid-vapor interface, $\dot{M}$:

$$\dot{M} = \frac{\dot{m}}{\dot{m}^{id}} = \frac{1}{1 + \kappa\eta}(1 + \phi) \tag{4.36}$$

where $\dot{m}^{id} = a(T_s - T_v)$ is the kinetic theory rate with a negligible resistance to conduction in the liquid ($T_s = T_{lv}$) and no effect of disjoining pressure or capillarity on the vapor pressure. Multiplying the numerator and the denominator by the latent heat of vaporization, $\dot{M}$ can also be viewed as the dimensionless interfacial evaporative heat flux.

Table 4.1 Values of δ_0, ε, $-\bar{A}$, $\dot{m}^{id}$, q^{id}, $(T_s - T_v)$, T_s at Various Power Inputs.

LIQUID: HEPTANE

Power Input (Watts)	δ_0 (nm)	ε	$-\bar{A}$ (Joules)	$\dot{m}^{id}$ (kg/m²·sec)	q^{id} (Watts/m²)	$(T_s - T_v)$ (°K)	T_s (°K)
0.0	15	2.5	1.27×10^{-22}	6.83×10^{-5}	2.479×10^{1}	4.514×10^{-5}	298.0
0.1	6.4	1.1	1.23×10^{-22}	8.50×10^{-4}	3.085×10^{2}	5.617×10^{-4}	299.6
0.2	6.2	1.5	0.87×10^{-22}	6.63×10^{-4}	2.406×10^{2}	4.381×10^{-4}	299.8
0.3	5.9	1.1	1.13×10^{-22}	9.99×10^{-4}	3.626×10^{2}	6.602×10^{-4}	300.1
0.5	5.65	1.05	1.14×10^{-22}	1.15×10^{-3}	4.174×10^{2}	7.600×10^{-4}	300.5
2.0	4.8	3.5	0.40×10^{-22}	1.11×10^{-3}	4.029×10^{2}	4.928×10^{-4}	309.7

LIQUID: R113

Power Input (Watts)	δ_0 (nm)	ε	$-\bar{A}$ (Joules)	$\dot{m}^{id}$ (kg/m²·sec)	q^{id} (Watts/m²)	$(T_s - T_v)$ (°K)	T_s (°K)
0.0	11.5	6.0	2.049×10^{-22}	1.92×10^{-3}	2.949×10^{2}	1.580×10^{-4}	298.0
0.25	4.8	5.5	0.933×10^{-22}	1.27×10^{-2}	1.950×10^{3}	1.045×10^{-3}	299.2
0.35	4.5	8.0	0.628×10^{-22}	1.04×10^{-2}	1.597×10^{3}	8.026×10^{-4}	300.6
0.50	4.0	4.0	1.124×10^{-22}	2.81×10^{-2}	4.316×10^{3}	2.054×10^{-3}	302.7

Table 4.1 Values of δ_o, ε, $-\bar{A}$, $\dot{m}$, q^{id}, (T_s-T_v), T_s at Various Power Inputs. (Continued)

LIQUID: PROPANOL

Power Input (Watts)	δ_o (nm)	ε	$-\bar{A}$ (Joules)	$\dot{m}^{id}$ (kg/m²·sec)	q^{id} (Watts/m²)	$(T_s - T_v)$ (°K)	T_s (°K)
0.0	13.6	5.5	4.505×10^{-23}	5.64×10^{-6}	4.534×10^{0}	8.344×10^{-6}	296.8
0.05	6.5	5.5	2.153×10^{-23}	2.47×10^{-5}	1.986×10^{1}	3.654×10^{-5}	297.0
0.075	5.2	5.5	1.722×10^{-23}	3.84×10^{-5}	3.087×10^{1}	5.681×10^{-5}	297.95
0.1	4.7	5.5	1.557×10^{-23}	4.73×10^{-5}	3.803×10^{1}	6.998×10^{-5}	298.5
0.125	4.4	5.5	1.457×10^{-23}	5.39×10^{-5}	4.333×10^{1}	7.974×10^{-5}	299.25
0.175	3.6	5.5	1.324×10^{-23}	1.04×10^{-4}	8.335×10^{1}	1.332×10^{-4}	300.1
0.54	2.9	5.0	1.305×10^{-23}	2.33×10^{-4}	1.860×10^{2}	2.548×10^{-4}	302.7
0.77	2.7	1.8	3.643×10^{-23}	9.10×10^{-4}	7.239×10^{2}	8.950×10^{-4}	304.8

LIQUID: BUTANOL

Power Input (Watts)	δ_o (nm)	ε	$-\bar{A}$ (Joules)	$\dot{m}^{id}$ (kg/m²·sec)	q^{id} (Watts/m²)	$(T_s - T_v)$ (°K)	T_s (°K)
0.0	17.2	11.0	1.975×10^{-23}	6.24×10^{-7}	3.629×10^{-1}	2.466×10^{-6}	298.0
0.05	5.9	5.0	1.546×10^{-23}	1.30×10^{-5}	7.560×10^{0}	4.807×10^{-5}	299.0
0.075	5.4	3.5	2.021×10^{-23}	2.21×10^{-5}	1.285×10^{1}	8.173×10^{-5}	299.1
0.1	4.9	2.25	2.853×10^{-23}	4.18×10^{-5}	2.431×10^{1}	1.546×10^{-4}	299.4
0.125	4.5	1.8	3.358×10^{-23}	6.64×10^{-5}	3.861×10^{1}	2.358×10^{-4}	299.9

SECTION 5

DISCUSSION

5.1. Macroscopic Results

Using the macroscopic heat balance model the evaporative heat flow rate based on two different sets of measurements agreed. This important result confirms the presence of evaporation and gives a measure of the contact line heat sink which is needed for the design of small heat exchangers. However, the microscopic results are more significant and are discussed below. Another interesting macroscopic phenomenon was observed during the high heat flux studies which are not reported in detail herein. The evaporating meniscus started to oscillate at higher power inputs (3 watts and greater). The oscillations increased with an increase in power input, but the meniscus maintained an average shape and still supplied cooling liquid to the hot spot. The oscillations appeared to improve the heat sink capability of the meniscus. We note that this is a more complex phenomenon than that analyzed above because the fluid flow rate may not be governed by disjoining and curvature gradients alone. For a power input of 4 watts the temperature of the interline was 53°C. At this high temperature, large surface tension gradients may start to influence the liquid flow rate [45].

5.2. Microscopic Results

5.2.1. Comparison of Data and Model

By the proper selection of ε, β_0 and β_1, good agreement could be obtained between the model Equation (4.21) and the data. There are two ways to evaluate this result. First, the agreement between

81

the experimental and theoretical profiles is good. This is an important achievement. Second, the values of the modified Hamaker constant, $\bar{A}$, are not a function of the evaporation rate. We note that there is scatter in the resulting values of $\bar{A}$. However, we feel that this scatter can be reduced by further adjustments in ε and the ratio β_0/β_1. We also feel that there is sufficient consistency between the systems to claim success. Although the polar and non-polar systems are different, the subsystems (polar versus non-polar) are consistent. Since this is the first nonequilibrium use of the procedures and experimental design, direct comparisons with past work cannot be made.

With regard to the absolute value of the Hamaker constant, we find it below the theoretical value of an ideal system. We feel that this is due to the complexity of the system needed to study transport phenomena. Therefore, we have measured an important property ($\bar{A}$) *in situ* at the start and used it to describe the characteristics of an evaporating meniscus. As discussed in the next subsection, these characteristics agree with theoretical expectations. The resulting confirmed model can then be used to predict the performance of an evaporating meniscus as discussed in Appendix B.

5.2.2. Calculation of Dimensionless Pressure and Curvature Profiles

In Figures (5.1-5.23) the dimensionless pressure, ϕ, and curvature, (η''), profiles are presented for the various fluids tested. The numerical procedures described in Section 4 and Appendix C were used to obtain these results. The interfacial pressure difference can be obtained by multiplying the dimensionless pressure by the reference disjoining pressure, Π_0, which is given in

82

Figure 5.1   Plot of Dimensionless Pressure and Curvature
vs. Dimensionless Film Thickness (Q = 0.0W,
δ_0 = 15 nm, π_0 = 3.76 x 10^1 N/m^2).

Figure 5.2   Plot of Dimensionless Pressure and Curvature
vs. Dimensionless Film Thickness (Q = 0.1W,
δ_0 = 6.4 nm, π_0 = 4.69 x 10^2 N/m^2).

83
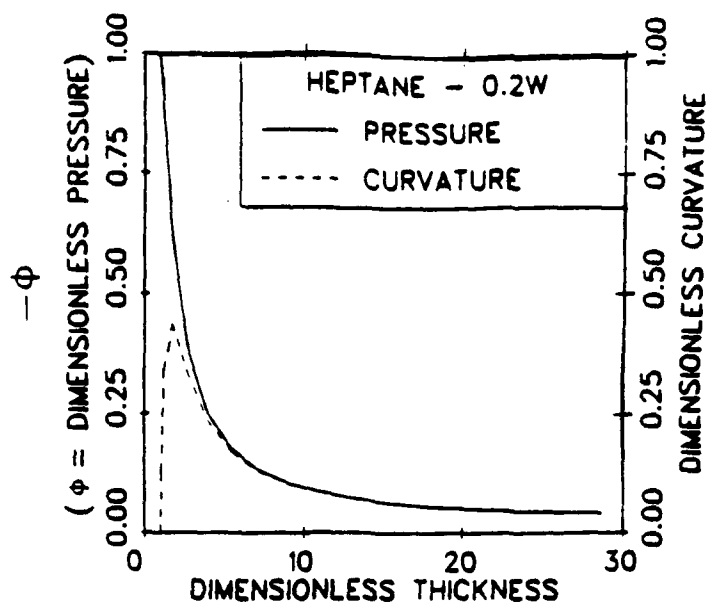
Figure 5.3   Plot of Dimensionless Pressure and Curvature vs. Dimensionless Film Thickness (Q = 0.2W, δ_0 = 6.2 nm, π_0 = 3.65 x 10^2 N/m^2).
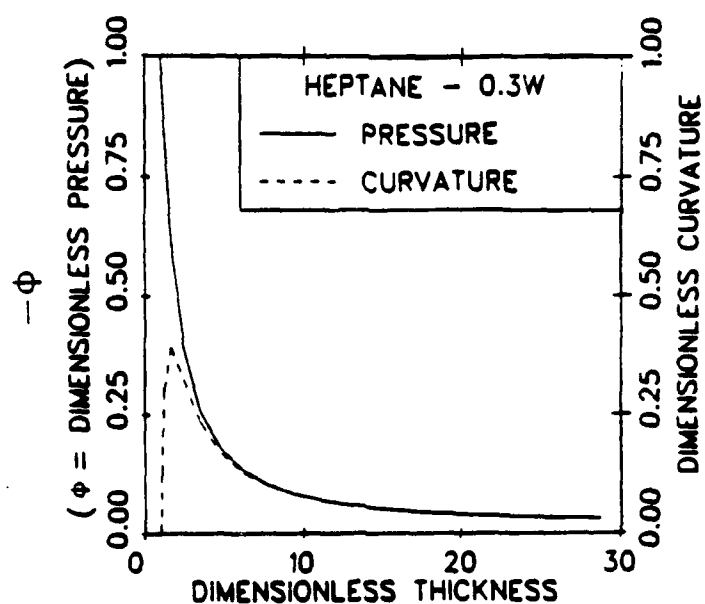
Figure 5.4   Plot of Dimensionless Pressure and Curvature vs. Dimensionless Film Thickness (Q = 0.3W, δ_0 = 5.9 nm, π_0 = 5.50 x 10^2 N/m^2).
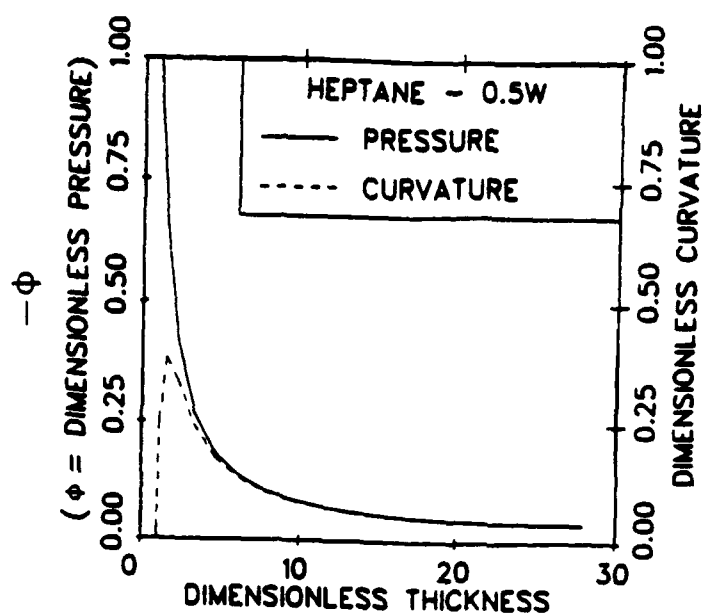
Figure 5.5   Plot of Dimensionless Pressure and Curvature vs. Dimensionless Film Thickness ($Q = 0.5W$, $\delta_0 = 5.65$ nm, $\pi_0 = 6.32 \times 10^2$ N/m^2).
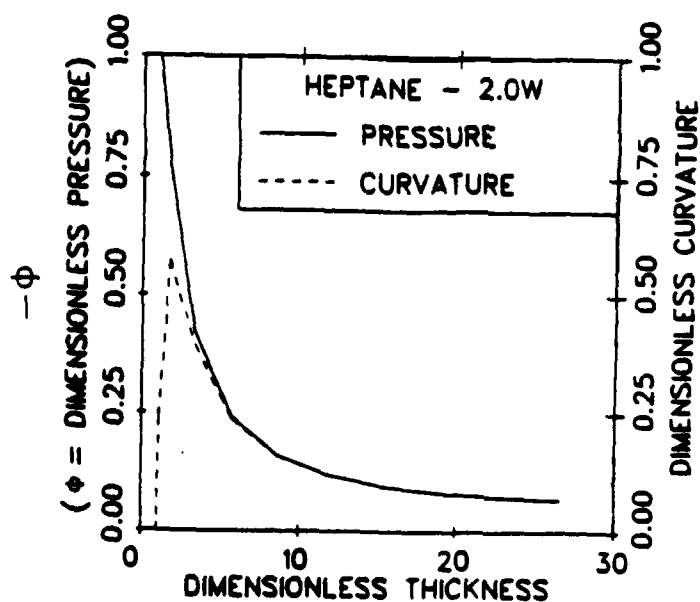
Figure 5.6   Plot of Dimensionless Pressure and Curvature vs. Dimensionless Film Thickness ($Q = 2.0W$, $\delta_0 = 4.8$ nm, $\pi_0 = 3.62 \times 10^2$ N/m^2).
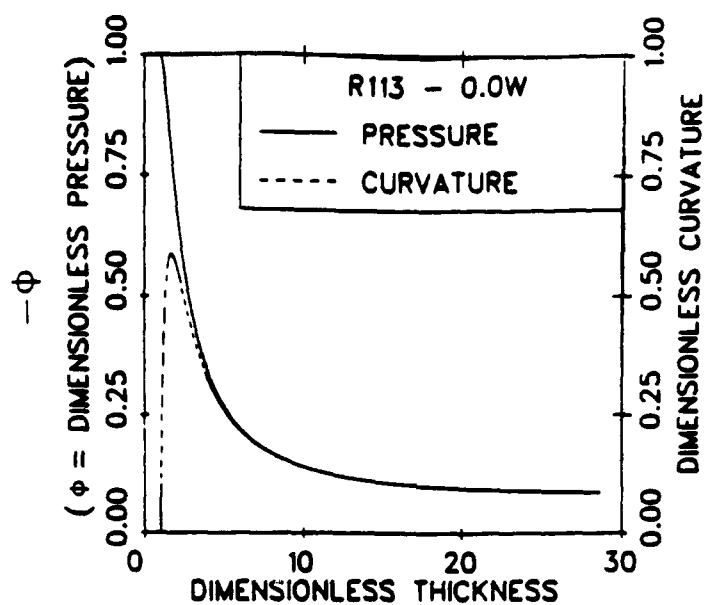
Figure 5.7   Plot of Dimensionless Pressure and Curvature
vs. Dimensionless Film Thickness (Q = 0.0W,
δ_0 = 11.5 nm, π_0 = 1.347 x 10^2 N/m²).
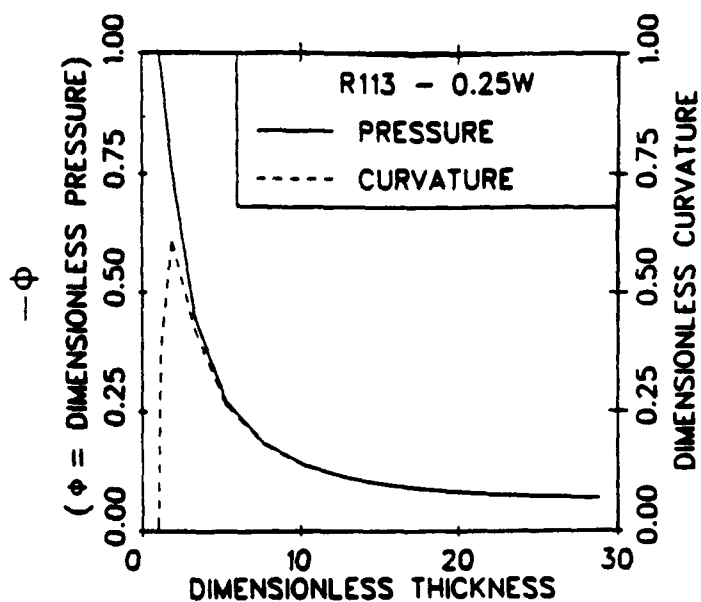
Figure 5.8   Plot of Dimensionless Pressure and Curvature
vs. Dimensionless Film Thickness (Q = 0.25W,
δ_0 = 4.8 nm, π_0 = 8.436 x 10^2 N/m²).
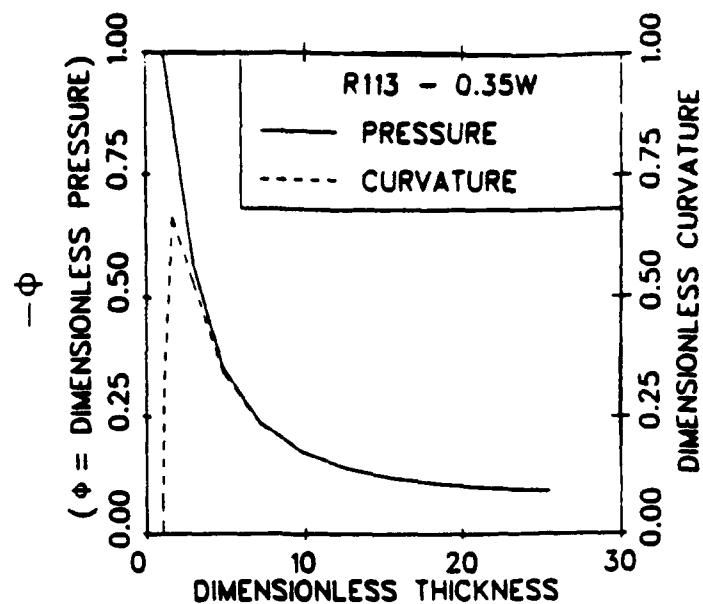
Figure 5.9   Plot of Dimensionless Pressure and Curvature
vs. Dimensionless Film Thickness (Q = 0.35W,
δ_0 = 4.5 nm, π_0 = 6.89 x 10^2 N/m^2).
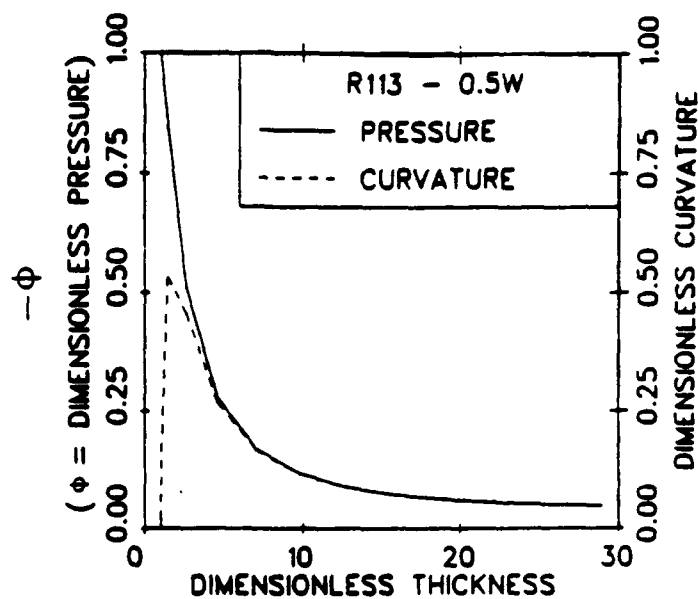
Figure 5.10   Plot of Dimensionless Pressure and Curvature
vs. Dimensionless Film Thickness (Q = 0.5W,
δ_0 = 4.0 nm, π_0 = 1.756 x 10^3 N/m^2).
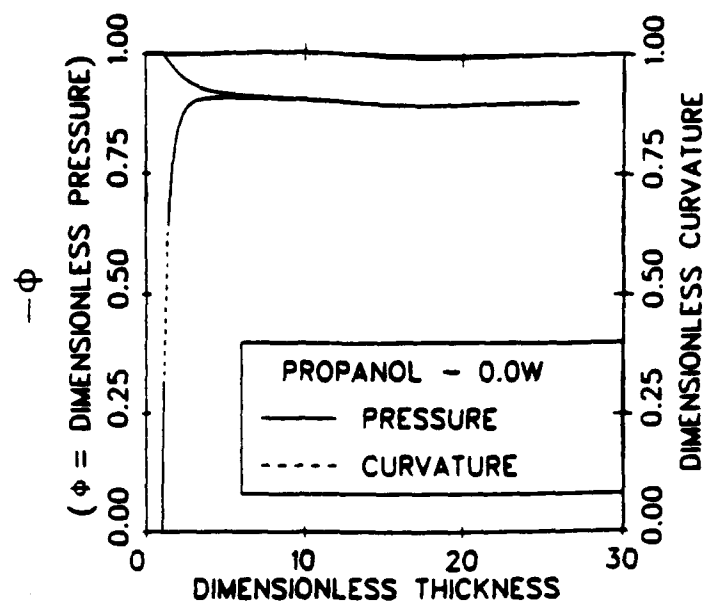
Figure 5.11   Plot of Dimensionless Pressure and Curvature
vs. Dimensionless Film Thickness ($Q = 0.0W$,
$\delta_0 = 13.6$ nm, $\pi_0 = 1.79 \times 10^1$ N/m^2).
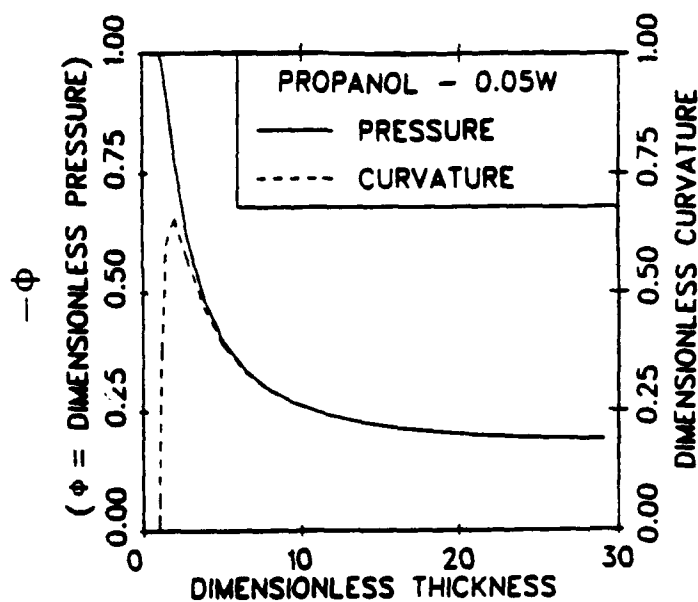
Figure 5.12   Plot of Dimensionless Pressure and Curvature
vs. Dimensionless Film Thickness ($Q = 0.05W$,
$\delta_0 = 6.5$ nm, $\pi_0 = 7.84 \times 10^1$ N/m^2).
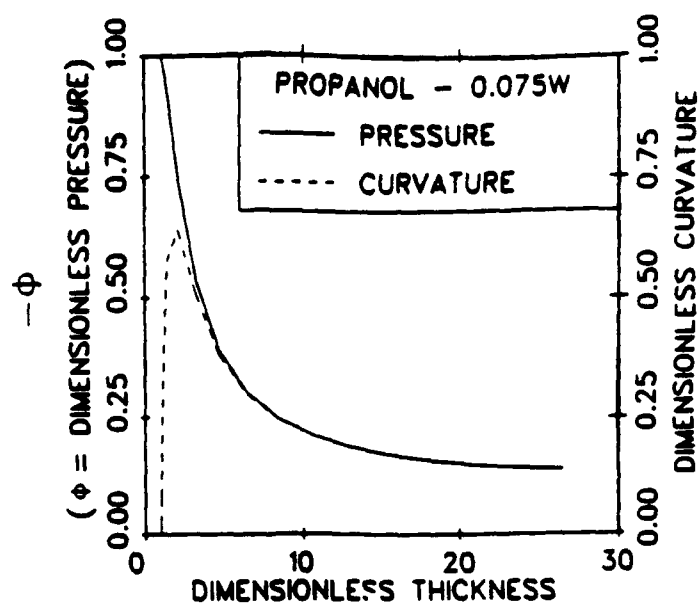
Figure 5.13   Plot of Dimensionless Pressure and Curvature
vs. Dimensionless Film Thickness (Q = 0.075W,
δ_0 = 5.2 nm, π_0 = 1.22 x 10^2 N/m²).
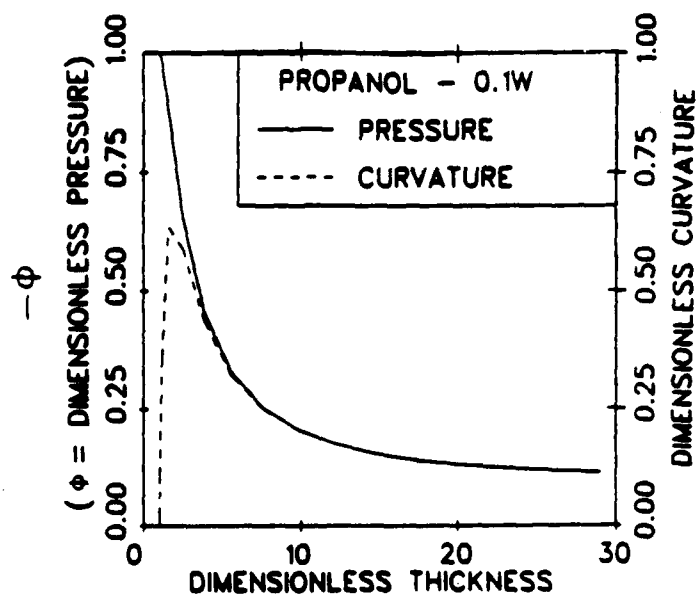
Figure 5.14   Plot of Dimensionless Pressure and Curvature
vs. Dimensionless Film Thickness (Q = 0.1W,
δ_0 = 4.7 nm, π_0 = 1.50 x 10^2 N/m²).

89
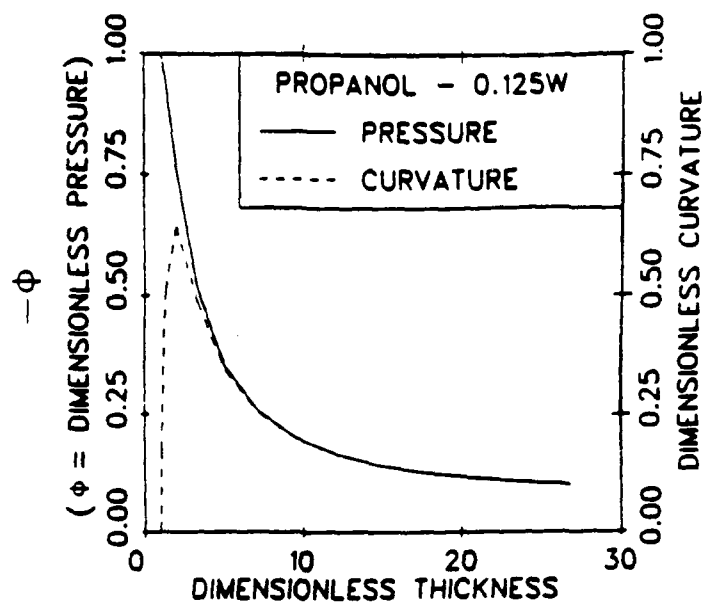
Figure 5.15   Plot of Dimensionless Pressure and Curvature
vs. Dimensionless Film Thickness (Q = 0.125W,
δ_0 = 4.4 nm, π_0 = 1.71 x 10^2 N/m^2).
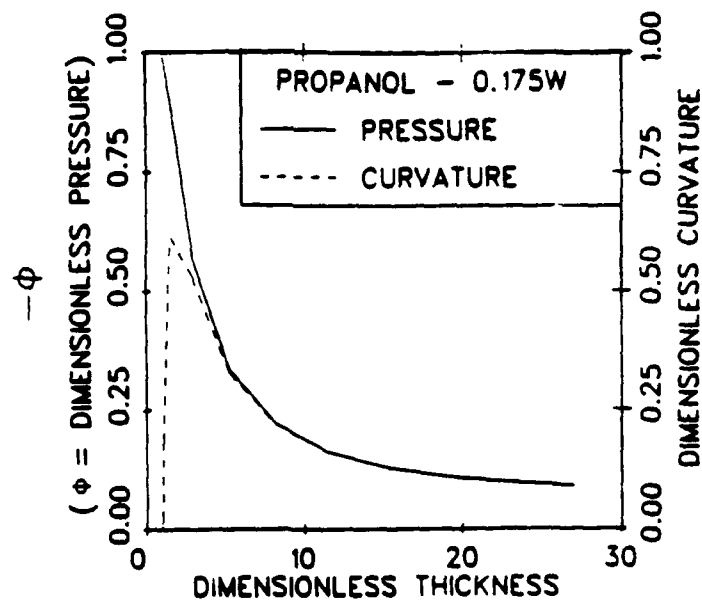
Figure 5.16   Plot of Dimensionless Pressure and Curvature
vs. Dimensionless Film Thickness (Q = 0.175W,
δ_0 = 3.6 nm, π_0 = 2.84 x 10^2 N/m^2).
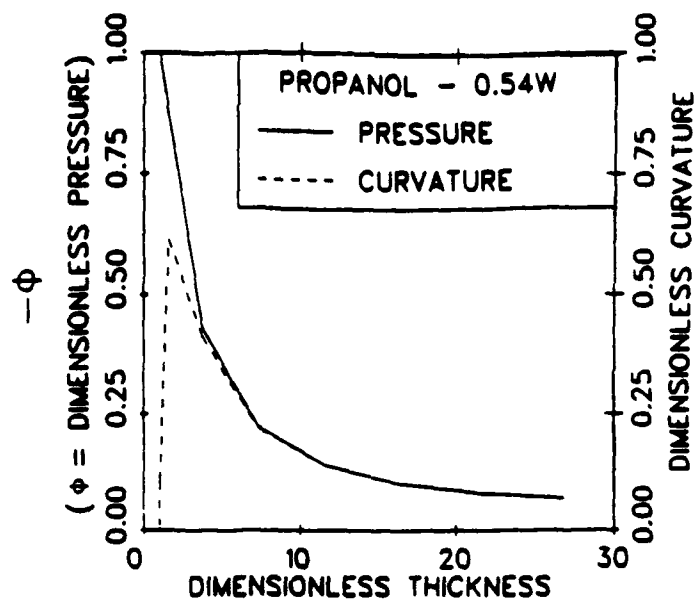
Figure 5.17   Plot of Dimensionless Pressure and Curvature
vs. Dimensionless Film Thickness (Q = 0.54W,
δ_0 = 2.9 nm, π_0 = 5.35 x 10^2 N/m^2).
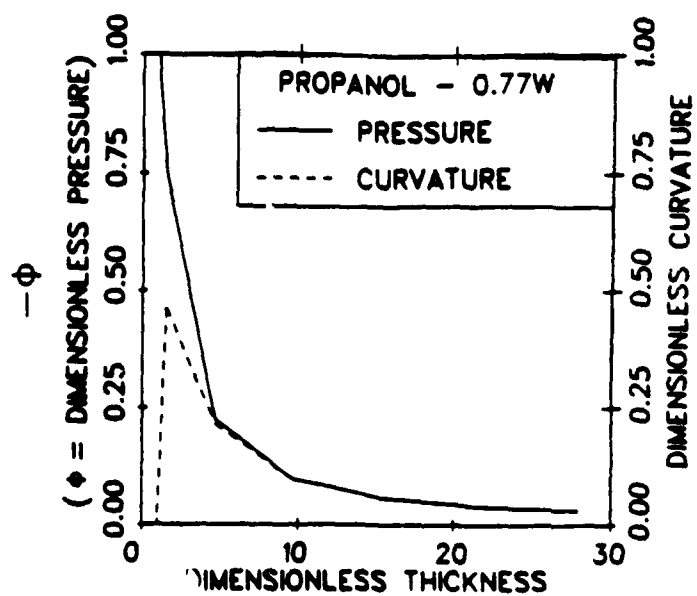
Figure 5.18   Plot of Dimensionless Pressure and Curvature
vs. Dimensionless Film Thickness (Q = 0.77W,
δ_0 = 2.7 nm, π_0 = 1.85 x 10^3 N/m^2).

91
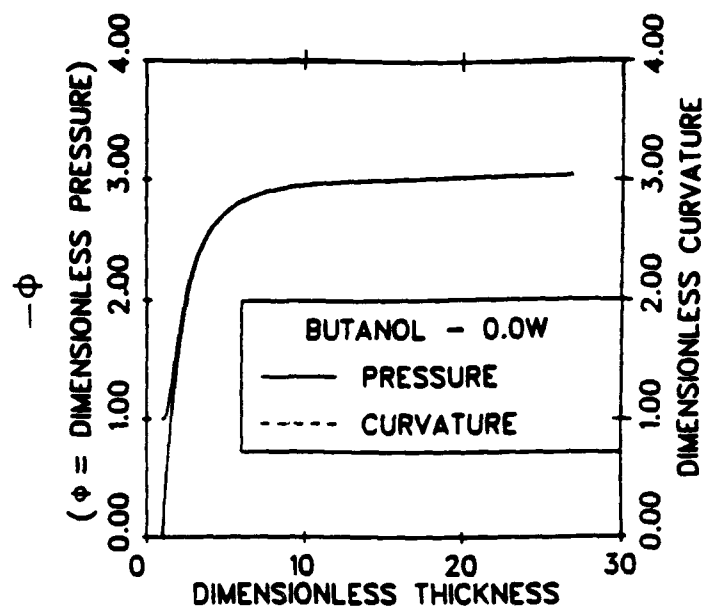
Figure 5.19   Plot of Dimensionless Pressure and Curvature vs. Dimensionless Film Thickness ($Q = 0.0W$, $\delta_0 = 17.2$ nm, $\pi_0 = 3.88 \times 10^0$ N/m^2).
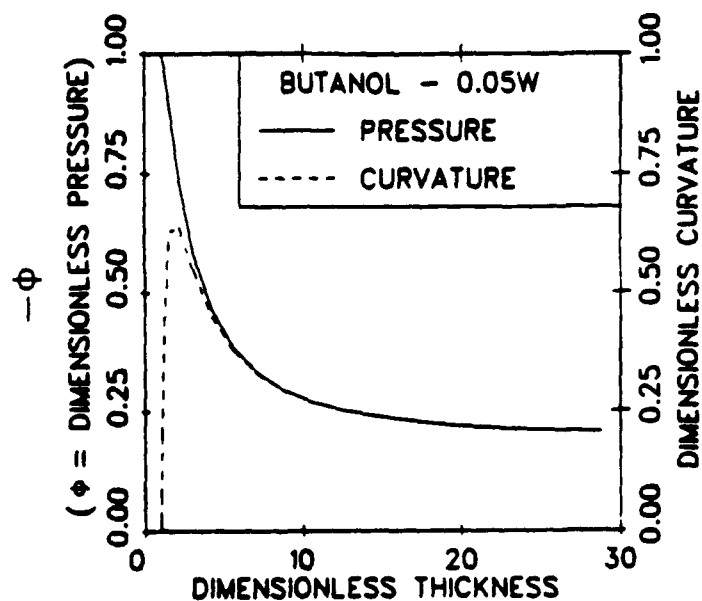
Figure 5.20   Plot of Dimensionless Pressure and Curvature vs. Dimensionless Film Thickness ($Q = 0.05W$, $\delta_0 = 5.9$ nm, $\pi_0 = 7.53 \times 10^1$ N/m^2).
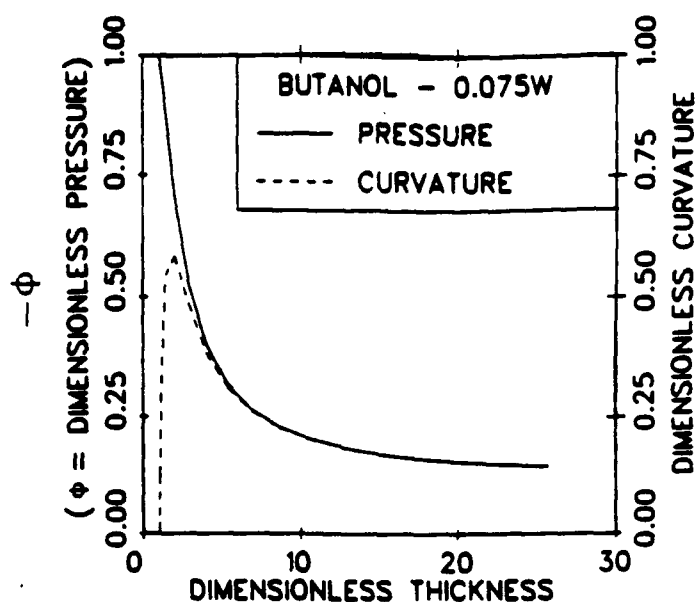
Figure 5.21   Plot of Dimensionless Pressure and Curvature
vs. Dimensionless Film Thickness (Q = 0.075W,
δ_0 = 5.4 nm, π_0 = 1.28 x 10^2 N/m²).
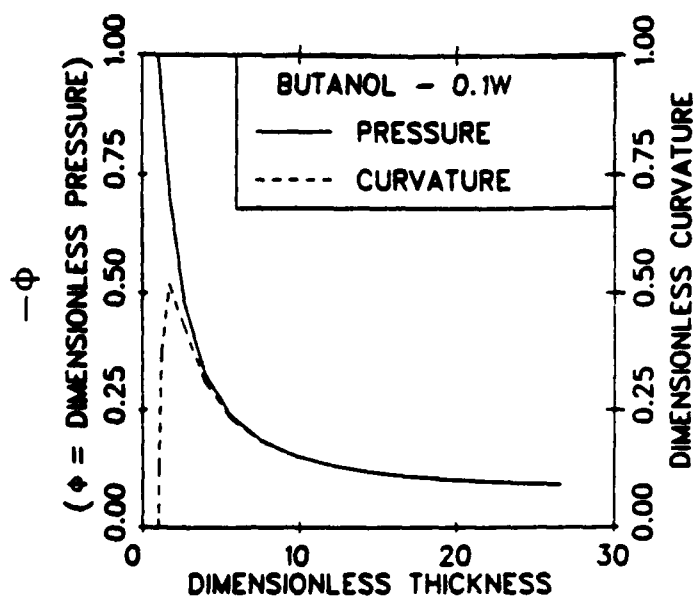
Figure 5.22   Plot of Dimensionless Pressure and Curvature
vs. Dimensionless Film Thickness (Q = 0.1W,
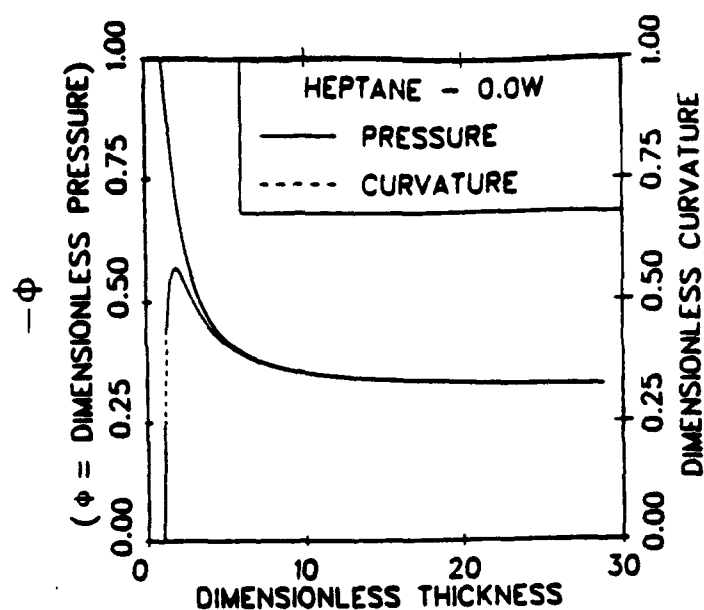δ_0 = 4.9 nm, π_0 = 2.42 x 10^2 N/m²).

93
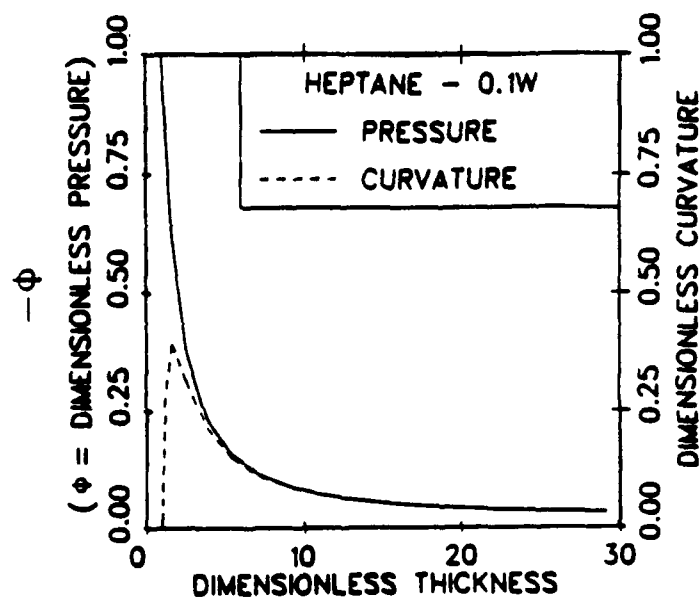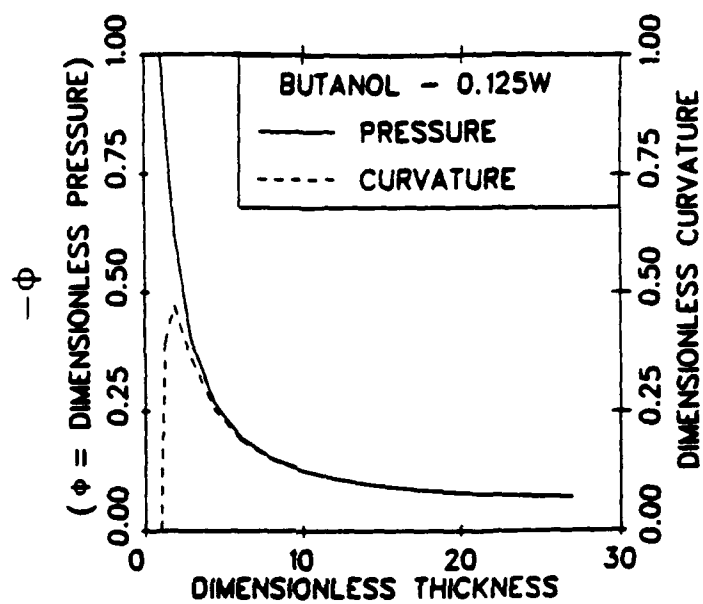
Figure 5.23 Plot of Dimensionless Pressure and Curvature
vs. Dimensionless Film Thickness (Q = 0.125W,
δ_0 = 4.5 nm, π_0 = 3.68 x 10^2 N/m^2).

94

the captions. The results clearly demonstrate that, initially, fluid flow results from a disjoining pressure gradient. In this region the curvature builds up to a maximum value at a relatively small thickness. The thickness can be obtained by multiplying the dimensionless thickness by the reference thickness, δ_0, which is also given in each caption. The effect that this curvature buildup has on the pumping capacity of a meniscus is addressed in Appendix B.

5.2.3. Calculation of Dimensionless Evaporative Heat or Mass Flux, $\dot{M}$, versus Dimensionless Film Thickness

The dimensionless interfacial heat or mass evaporative flux, $\dot{M}$, profiles are presented in Figures (5.24-5.33). The dimensional evaporative mass flux can be obtained by multiplying these values by the reference ideal mass flux, $\dot{m}^{id}$, which is given in each caption. To obtain the heat fluxes, the reference ideal heat fluxes are given in Table 4.1. The right-hand side of Equation (4.21) which is equal to $\dot{M} = \dot{m}/\dot{m}^{id} = q/q^{id}$ can be used to describe the characteristics of the profile. At the interline, δ_0, the dimensionless pressure, ϕ, is given by $\phi = -1$. Therefore, the flux is equal to zero. The variation of ϕ with thickness is given in Figures (5.1-5.23). These figures show that the absolute value of ϕ decreases as the thickness increases. Therefore, the interfacial flux increases because the effect of interfacial forces decreases. This increase does not continue indefinitely because of conductive resistance in the liquid film which is represented by $\kappa\eta$ in Equation (4.21). Therefore, we obtain a maximum in the flux profile and note that the resistances are substantial. All the trends are as expected. A recent numerical study by Busse, et al. also predicted substantial resistances in the contact line region [58].
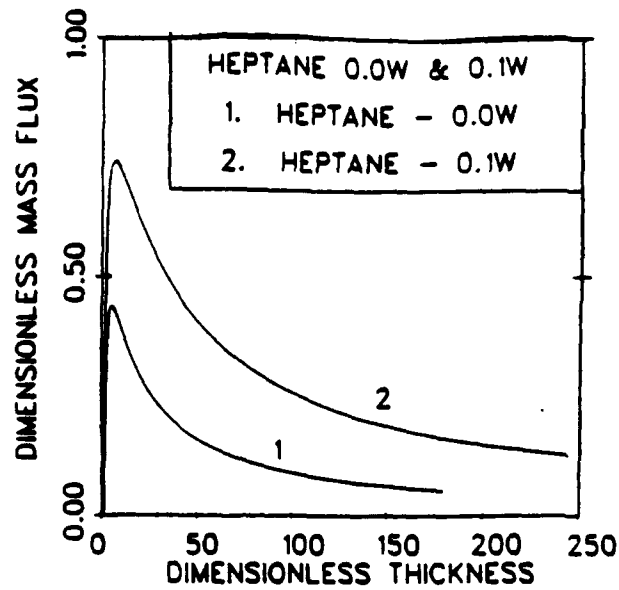
Figure 5.24

Dimensionless Mass Flux, $\dot{M}$ vs. Dimensionless Film Thickness, η.

$$\begin{pmatrix} \text{Case 1} & Q = 0.0W, & \delta_o = 15 \text{ nm}, & \dot{m}^{id} = 6.83 \times 10^{-5} \text{ kg/m}^2\cdot\text{sec} \\ \text{Case 2} & Q = 0.1W, & \delta_o = 6.4 \text{ nm}, & \dot{m}^{id} = 8.50 \times 10^{-4} \text{ kg/m}^2\cdot\text{sec} \end{pmatrix}$$
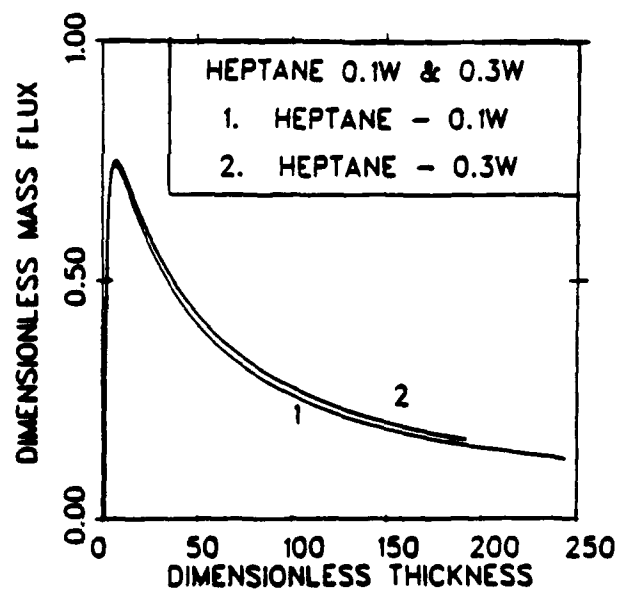
Figure 5.25

Dimensionless Mass Flux, $\dot{M}$ vs. Dimensionless Film Thickness, η.

$$\begin{pmatrix} \text{Case 1} & Q = 0.1W, & \delta_o = 6.4 \text{ nm}, & \dot{m}^{id} = 8.50 \times 10^{-4} \text{ kg/m}^2\cdot\text{sec} \\ \text{Case 2} & Q = 0.3W, & \delta_o = 5.9 \text{ nm}, & \dot{m}^{id} = 9.99 \times 10^{-4} \text{ kg/m}^2\cdot\text{sec} \end{pmatrix}$$

96
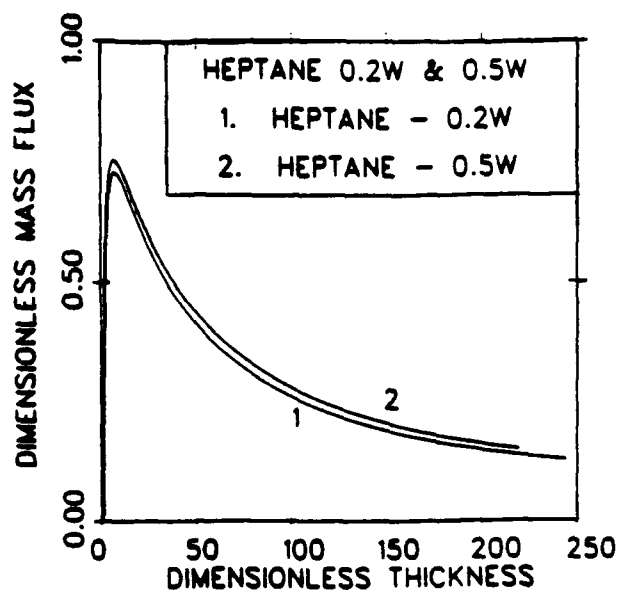
Figure 5.26

Dimensionless Mass Flux, $\dot{M}$ vs. Dimensionless Film Thickness, η.

$$\left(\begin{array}{l} \text{Case 1} \quad Q = 0.2W, \ \delta_0 = 6.2 \text{ nm}, \ \dot{m}^{id} = 6.63 \times 10^{-4} \text{ kg/m}^2 \cdot \text{sec} \\ \text{Case 2} \quad Q = 0.5W, \ \delta_0 = 5.65 \text{ nm}, \ \dot{m}^{id} = 1.15 \times 10^{-3} \text{ kg/m}^2 \cdot \text{sec} \end{array}\right)$$
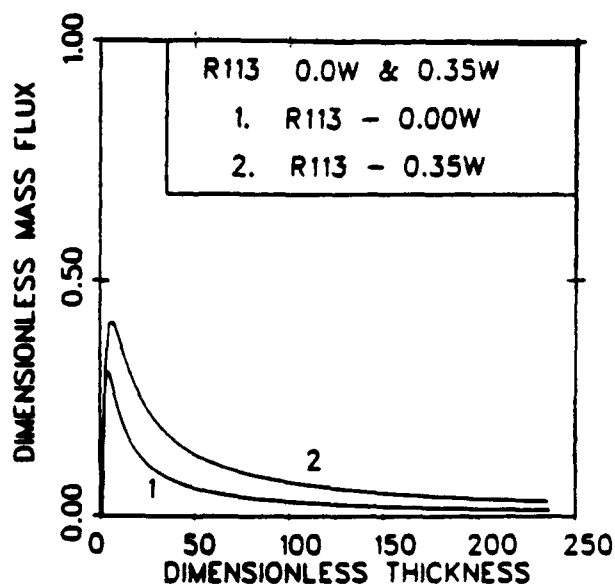
Figure 5.27

Dimensionless Mass Flux, $\dot{M}$ vs. Dimensionless Film Thickness, η.

$$\left(\begin{array}{l} \text{Case 1} \quad Q = 0.0W, \ \delta_0 = 11.5 \text{ nm}, \ \dot{m}^{id} = 1.92 \times 10^{-3} \text{ kg/m}^2 \cdot \text{sec} \\ \text{Case 2} \quad Q = 0.35W, \ \delta_0 = 4.5 \text{ nm}, \ \dot{m}^{id} = 1.04 \times 10^{-2} \text{ kg/m}^2 \cdot \text{sec} \end{array}\right)$$

97
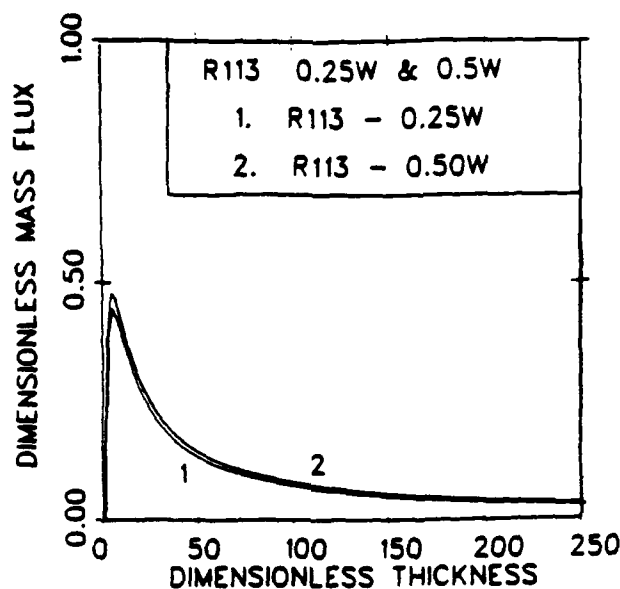
Figure 5.28

Dimensionless Mass Flux, $\dot{M}$ vs. Dimensionless Film Thickness, η.

$$\left(\begin{array}{l} \text{Case 1} \quad Q = 0.25W, \; \delta_0 = 4.8 \text{ nm}, \; \dot{m}^{id} = 1.27 \times 10^{-2} \text{ kg/m}^2 \bullet \text{sec} \\ \text{Case 2} \quad Q = 0.5W, \; \delta_0 = 4.0 \text{ nm}, \; \dot{m}^{id} = 2.81 \times 10^{-2} \text{ kg/m}^2 \bullet \text{sec} \end{array} \right)$$
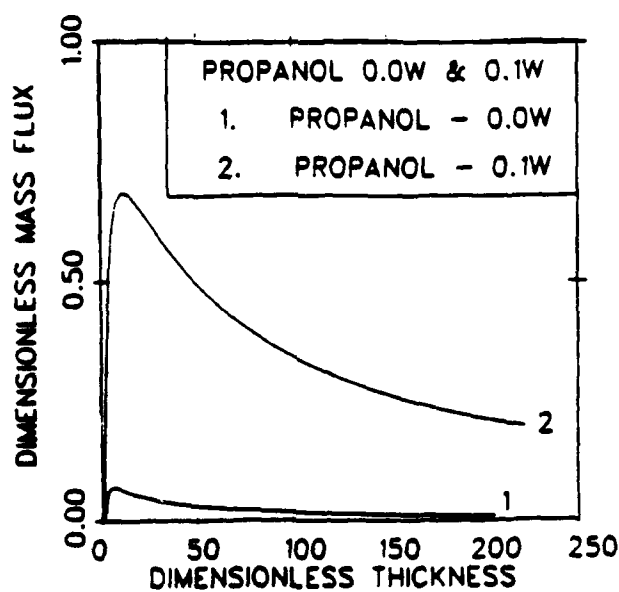
Figure 5.29

Dimensionless Mass Flux, $\dot{M}$ vs. Dimensionless Film Thickness, η.

$$\left(\begin{array}{l} \text{Case 1} \quad Q = 0.0W, \; \delta_0 = 13.6 \text{ nm}, \; \dot{m}^{id} = 5.64 \times 10^{-6} \text{ kg/m}^2 \bullet \text{sec} \\ \text{Case 2} \quad Q = 0.1W, \; \delta_0 = 4.7 \text{ nm}, \; \dot{m}^{id} = 4.73 \times 10^{-5} \text{ kg/m}^2 \bullet \text{sec} \end{array} \right)$$

98
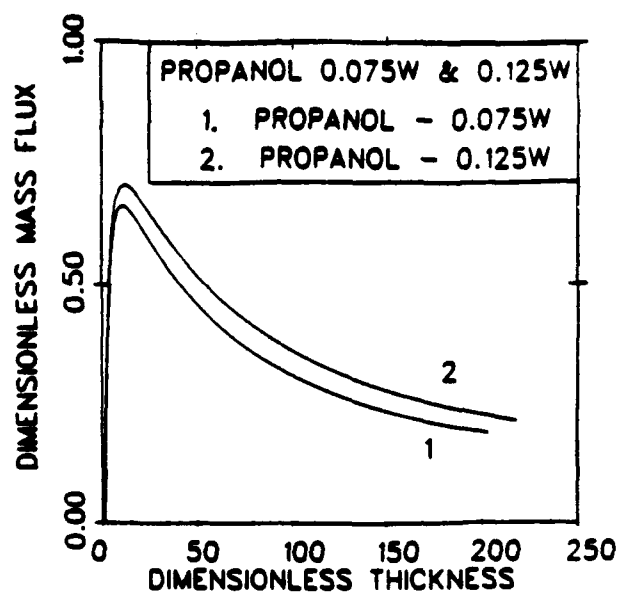
Figure 5.30

Dimensionless Mass Flux, $\dot{M}$ vs. Dimensionless Film Thickness, η.

$$\left(\begin{array}{l} \text{Case 1} \quad Q = 0.075\text{W}, \ \delta_0 = 5.2 \text{ nm}, \ \dot{m}^{id} = 3.84 \times 10^{-5} \text{ kg/m}^2\text{•sec} \\ \text{Case 2} \quad Q = 0.125\text{W}, \ \delta_0 = 4.4 \text{ nm}, \ \dot{m}^{id} = 5.39 \times 10^{-5} \text{ kg/m}^2\text{•sec} \end{array} \right)$$
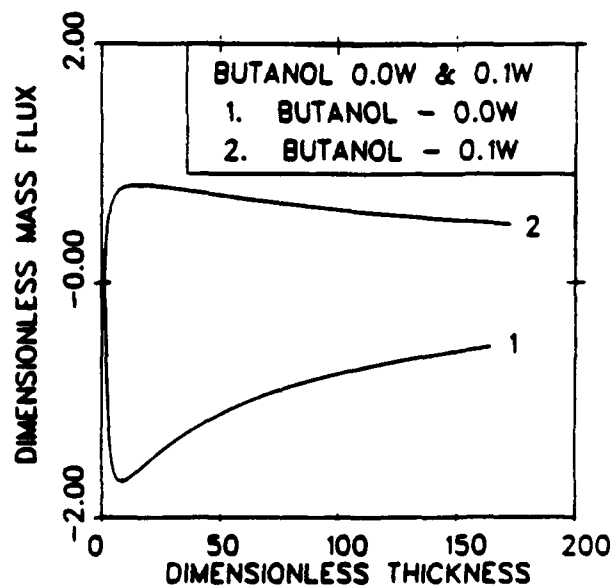
Figure 5.31

Dimensionless Mass Flux, $\dot{M}$ vs. Dimensionless Film Thickness, η.

$$\left(\begin{array}{l} \text{Case 1} \quad Q = 0.0\text{W}, \ \delta_0 = 17.2 \text{ nm}, \ \dot{m}^{id} = 6.24 \times 10^{-7} \text{ kg/m}^2\text{•sec} \\ \text{Case 2} \quad Q = 0.1\text{W}, \ \delta_0 = 4.9 \text{ nm}, \ \dot{m}^{id} = 4.18 \times 10^{-5} \text{ kg/m}^2\text{•sec} \end{array} \right)$$

99
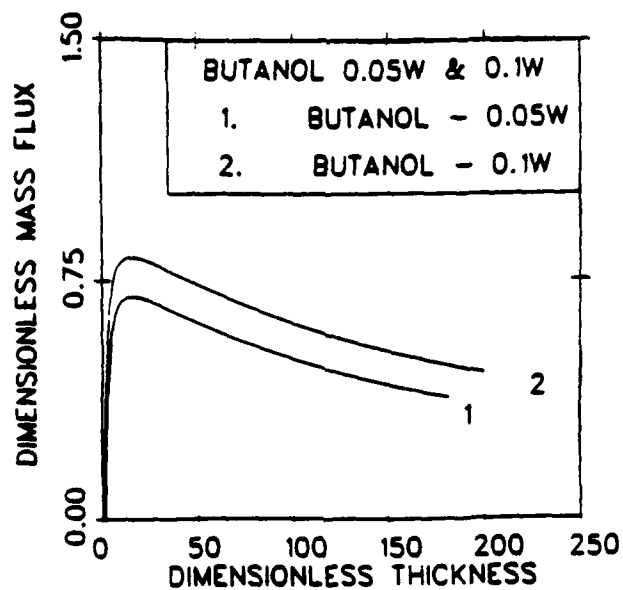
Figure 5.32

Dimensionless Mass Flux, $\dot{M}$ vs. Dimensionless Film Thickness, η.

$\left(\begin{array}{l} \text{Case 1} \quad Q = 0.05W, \; \delta_0 = 5.9 \text{ nm}, \; \dot{m}^{id} = 1.30 \times 10^{-5} \text{ kg/m}^2\cdot\text{sec} \\ \text{Case 2} \quad Q = 0.1W, \; \delta_0 = 4.9 \text{ nm}, \; \dot{m}^{id} = 4.18 \times 10^{-5} \text{ kg/m}^2\cdot\text{sec} \end{array}\right)$
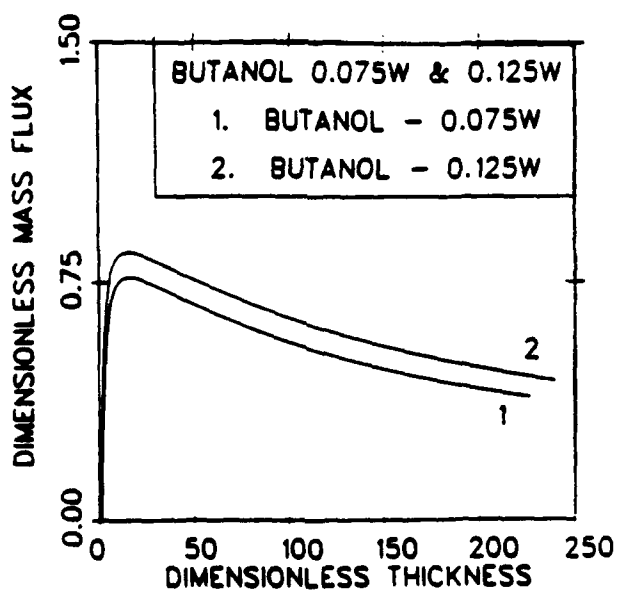
Figure 5.33

Dimensionless Mass Flux, $\dot{M}$ vs. Dimensionless Film Thickness, η.

$\left(\begin{array}{l} \text{Case 1} \quad Q = 0.075W, \; \delta_0 = 5.4 \text{ nm}, \; \dot{m}^{id} = 2.21 \times 10^{-5} \text{ kg/m}^2\cdot\text{sec} \\ \text{Case 2} \quad Q = 0.125W, \; \delta_0 = 4.5 \text{ nm}, \; \dot{m}^{id} = 6.64 \times 10^{-5} \text{ kg/m}^2\cdot\text{sec} \end{array}\right)$

100

Finally, in Figure 5.34, examples of the integral evaporative heat sink for the same power input for the region studied are presented. Again, all the trends are as expected. However, the effect due to conduction was not in the original model. We find that the resistance due to thermal conduction also has a significant effect on the integral evaporative heat sink because these curves tend to become parallel to the δ axis. Therefore, both interfacial forces and thermal conduction control the heat sink characteristics of the evaporating meniscus.

5.2.4.   Application of the Results

We find that the simplest overview of the results can be obtained using the right-hand side of Equation (4.21) which is the dimensionless interfacial mass (or heat) flux given by:

$$\overset{\bullet}{M} = \frac{\overset{\bullet}{m}}{\overset{\bullet}{m}_{id}} = \frac{1}{1 + \kappa\eta}(1 + \phi) \qquad (5.1)$$

This demonstrates that a smaller (i.e., $\kappa\eta$ small) **stable** meniscus could have a high evaporative heat flux. The reference flux, $\overset{\bullet}{m}$ given by Equation (4.34) would be large with moderate T and ΔT. On the other hand, if the system is extremely small, the value of ϕ (which is negative) could make the flux negligible. In addition, viscous forces represented by the left-hand side of Equation (4.21) could make the system unstable.

We find that the experimental results confirm the proposed model presented in Section 4 for the characteristics of an evaporating meniscus. Therefore, the model could, within limits, be used to evaluate the heat sink capability of other systems. Stability at higher heat fluxes is an unknown. Smaller systems should be more stable and, therefore, have a capacity to operate at higher heat fluxes. Obviously, this should be evaluated with additional experimental studies. The heat sink capacity of transient systems should also be evaluated using the optical techniques developed within this study.

101
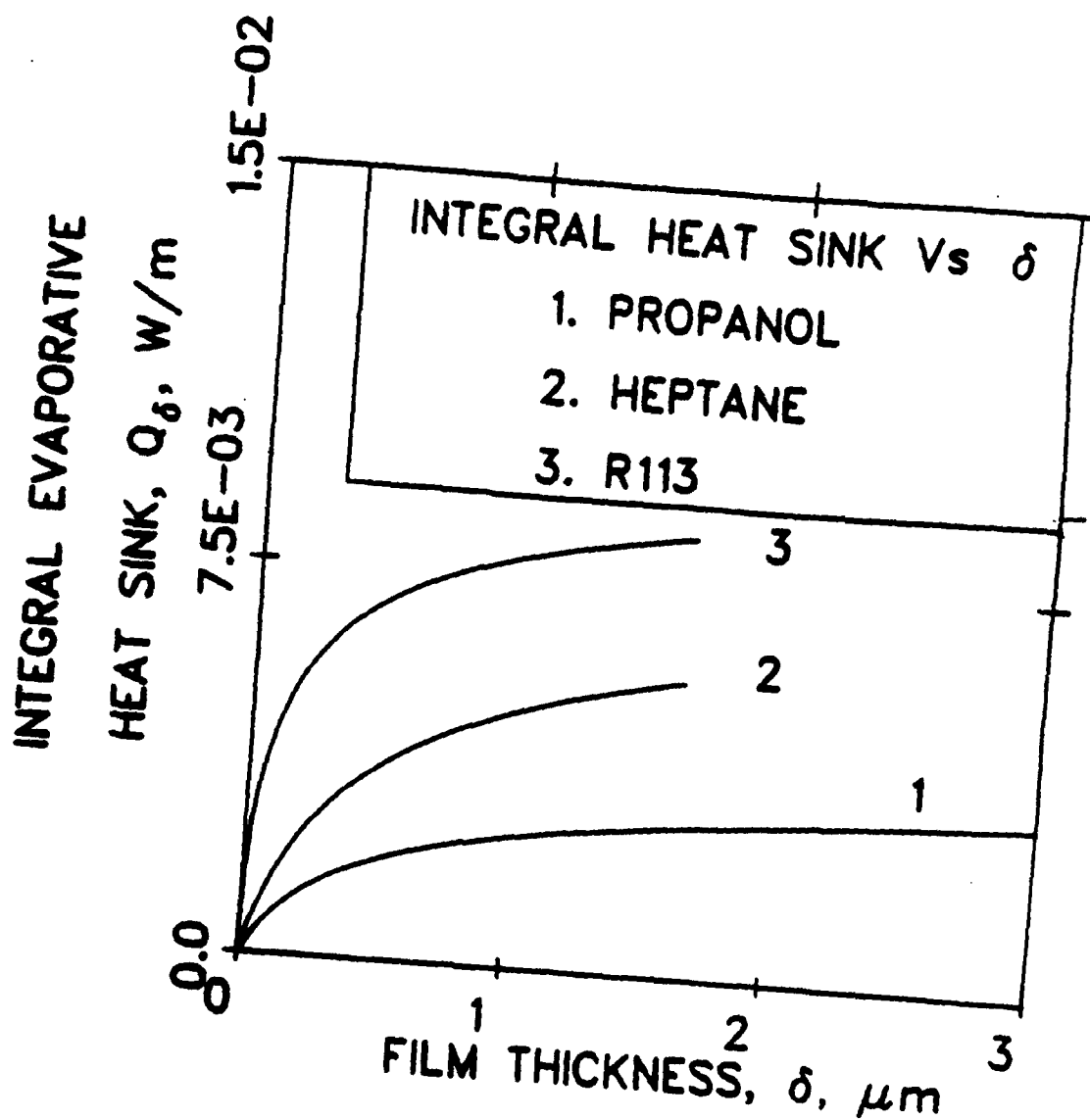
Figure 5.34   Integral Evaporative Heat Sink vs. Film Thickness
(Q = 0.5W for all the cases).

SECTION 6

CONCLUSIONS

1. A reversible capillary fed heat transfer cell was successfully used to obtain both the macroscopic and microscopic heat transfer characteristics of an evaporating extended meniscus.

2. Ellipsometry and microcomputer enhanced interferometry were successfully used to obtain the thickness profile of the meniscus as a function of evaporation rate.

3. Video image processing provided a convenient, efficient and accurate method for evaluating changes in the thickness profiles of evaporating thin liquid films.

4. The experimental results obtained for the relatively low heat fluxes studied generally confirm the basic model presented. Therefore, the model can be used to predict the performance of other systems and/or operating conditions.

5. We find that there are significant resistances to heat transfer in a small meniscus due to interfacial forces, viscous stresses, and thermal conduction. Therefore, the ideal heat flux based on kinetic theory cannot be obtained.

REFERENCES

1. Derjaguin, B.V., *Zh. Fiz. Khim.*, **14**,137 (1940).

2. Dzyaloshinskii, I.E., Lifshitz, E.M.,and Pitaevskii, L.P., *Ad. Phys.*, **10**, 165 (1961).

3. Sheludko, A., *Advan. Colloid Interface Sci.* **1**, 39 (1969).

4. Miller, C.A., and Ruckenstein, E., *J. Colloid Interface Sci.*,**48**, 368 (1974).

5. Derjaguin, B.V., Starov, V.M., and Churaev, N.V., *Colloid J. USSR* (English Translation), **38**, 786 (1976).

6. Derjaguin, B.V., and Churaev, N.V., *J. Colloid Interface Sci.*, **54**, 157 (1976).

7. Derjaguin, B.V., Nerpin, S.V., and Churaev, N.V. *,Bull. Rilem*, **29**, 93 (1965).

8. Potash, M., Jr. and Wayner, P.C., Jr., *Int. J. Heat Mass Transfer*, **15**, 1851 (1972).

9. Wayner, P.C., Jr., Kao, Y.K., and LaCroix, L.V., , *Int. J. Heat Mass Transfer*, **19**, 487 (1976).

10. Renk, F., Wayner, P.C., Jr., and Homsy, G.M., *J Colloid Interface Sci.*, **67**, 408 (1978).

11. Moosman, S. and Homsy, S.M., *J. Colloid Interface Sci.*, **73**,212 (1980).

12. Ivanov, I.B., and Toshev, B.V., *Colloid and Polymer Sci.*, **253**, 593 (1975).

13. Holm, F.W., and Goplen, S.P., *J. Heat Transfer*, **101**, 543 (1979).

14. Das, S. and Gaddis, J.L., in *"Nonequilibrium Transport Phenomena,"* (F. Dobran, et al., Eds.), HTD-Vol. 77, p. 17, ASME, New York, 1987.

15. Mirzamoghadam, A.Y., and Catton, I., in *"Augmentation of Heat Transfer in Energy Systems,"* (P.J. Bishop, Ed.), HTD-Vol. 52, p. 47, ASME, New York,1985.

16. Adamson, A.W. and Zebib, A., *J. Phys. Chem.*, **84**, 2619 (1980).

17. Chen., J.D., and Slattery, J.C., *AIChE J.*, **28**, 955 (1982).

18. Teletzke, G.F., Davis, H.T., and Scriven, L.E., *Chem. Eng. Comm.*, **55**, 41 (1987).

19. Wayner, Jr., P.C., *Colloids and Surfaces*, **52**, 71-84 (1991) [also included in report # WRDC-TR-90-2008].

20. DeGennes, P.G., *Rev. Mod. Phys.*, **57**, 827-863 (1985).

21. Derjaguin, B.V., Churaev, N.V. and Muller, V.M., *"Surface Forces,"* Consultants Bureau, NY (1987).

22. DeFeijter in *"Thin Liquid Films, Fundamentals and Applications,"* (I.B. Ivanov, Ed.), p. 1, Marcel Dekker, Inc., New York, 1988.

23. Neogi, P. and Miller, C.A., AIChE Symposium Series, **252(82)**, 145-155 (1988).

24. Tan, M.J., Bankoff, S.G. and Davis, S.H., *Physics of Fluids A*, **2**, 313-321, (1990).

25. Burelbach, J.P., Bankoff, S.G., and Davis, S.H., *Physics of Fluids A*, **2**, 322-333 (1990).

26. Bankoff, S.G., *ASME J. of Heat Transfer*, **112**, 538-546 (1990).

27. Derjaguin, B.V. and Zorin, Z.M., in "Proc. 2nd Int. Conf. Surface Activity," (J.H. Schulman, Ed.), **2**, p. 145, Butterworths, London, 1957..

28. Bascom, W.D., Cottington, R.L., and Singleterry, C.R., in *"Contact Angle, Wettability and Adhesion,"* (R.E. Gould, Ed.), Adv. Chem. Ser. No. 43, Am. Chem. Soc., Washington, DC, p. 355, 1964.

29. Ingram, B.J., *J. Chem. Soc., Faraday Trans. I.*, **70**, 868 (1974).

30. Blake, T.D., *J. Chem. Soc., Faraday Trans. I.*, **71**, 192 (1975).

31. Sabisky, E.S. and Anderson, C.H., *Phys. Rev. A.*, **7**, p. 790 (1973).

32. Renk, F.J. and Wayner, P.C., Jr., *J. of Heat Transfer*, **101**, 55-62 (1979).

33. Cook, R., Tung, C.Y., and Wayner, Jr., P.C., *J. Heat Transfer*, **103**, 325 (1981).

34. Zorin, Z.M., Churaev, N.V., and Shishin, V.A., *Colloid J.*, (English Translation), **40**, 828 (1978).

35. Kayser, R.F., Schmidt, J.W., and Moldover, M.R., *Phys. Rev.Lett.*, **54**, 707 (1985).

36. Truong, J.G. and Wayner, Jr., P.C., *J. Chem. Phys.*, **87**(7), p. 4187 (1987).

37. Gee, M.L., Healy, T.W., and White, L.R. *J. Colloid Interface Sci.*, **131**,18 (1989).

38. Beaglehole, D., *J.Phys.Chem*, **93**, 893 (1989).

39. Voutsinos, C.M., and Judd, R.L,. *J. Heat Transfer*, **97**, 88 (1975).

40. Sujanani, M. and Wayner, P.C., Jr., in *"Hydrodynamics of Dispersed Media,"* (J.P. Hulin, et al., Ed.), Elsevier, North Holland, p. 55, 1990..

41. Truong, J.G. and Wayner, P.C., Jr., in Proceedings of the 8th International Heat Transfer Conference, (C.L. Tien, V.P. Carey and J.K. Ferrell, Ed.) Hemisphere Publishing Corp., Washington, **2**, p. 507, 1986.

42. Sujanani, M. and Wayner, P.C., Jr., to be pulished in *J. Colloid and Interface Science*.

43. Kiewra, E. and Wayner, P.C., Jr., *J. of Electrochemical Soc.*, **136**, 740-746 (1989).

44. Schonberg, J. and Wayner, P.C., Jr., Proceedings of 9th International Heat Transfer Conference, Edited by G. Hestroni, Hemisphere Publishing Co., New York, **4**, 228-234 (1990) [also included in report # WRDC-TR-90-2008]

45. Parks, C.J. and Wayner, P.C., Jr., *AIChE J.*, **33**, 1 (1987).

46. Brinker,C.J., Hurd, A.J., Frye, G.C., Ward, K.J. and Ashley, C.J., *J. of Non-Crystalline Solids*, **121**, 294-302 (1990).

47. Scherer, G.W., *J. of Non-Crystalline Solids*, **121**, 104-109 (1990).

48. Tilton, D.,Chow, L., Mahefkey,E., and Switzer,G., Paper # AIAA 90-1729, AIAA/ASME 5th Joint Thermophysics and Heat Transfer Conference, Seattle, WA., June18-20,1990.

49. Peterson, G.P and Babin, B.R., WRDC - TR -89 - 2067, 24 June 1989.

50. Israelachvili, J., Intermolecular and Surface Forces, Academic Press, New York (1985)

51. Sujanani, M and Wayner, P.C.,Jr., to be published in *J. Colloid and Interface Sci.*

52. DasGupta, S., Sujanani, M., and Wayner, P.C., Jr., "Microcomputer Enhanced Optical Investigation of an Evaporating Liquid Film Controlled by a Capillary Feeder," Presented at 2nd World Conference on Experimental Heat Transfer, Fluid Mechanics and Thermodynamics, Dubrovnik, Yugoslavia, June 23-28, 1991.

53 . Ivanov, I.B. and Kralchevsky , P.A., in Thin Liquid Films (I.B. Invanov, Ed.) p. 49, Dekker, New York, (1988).

54. Cooper,W.and Nuttal,J., *J Agricult. Sci.*, 7, 219 -239 (1915).

55. Wayner, P.C.,Jr., *AIAA Journal*, 17, 772-776 (1979).

56. Schonberg,J. A. and Wayner, P.C., Jr. (expanded form of AIAA-90-1787) to be published in *J. Thermophysics & Heat Transfer*.

57. Bluman, G.W. and Cole, J.D., Similarity Methods for Differential Equations, Springer-Verlag, New York, Heidelberg, Berlin, 1974.

58. Stephan, P.C. and Busse, C.A., Theoretical Study of an Evaporating Meniscus in a Triangular Groove, 7th Int. Heat Pipe Conference, Minsk, USSR, 1990.

APPENDIX A

A.1 Interfacial Phenomena Concepts

The following discussion relates the concept of disjoining pressure to more classical interfacial concepts.

A.1.1 Classical

When a liquid comes into contact with a solid substrate, one of three conditions must exist at equilibrium: complete wetting, partial wetting, or nonwetting. Complete wetting occurs when the liquid spreads on the solid substrate to form an equilibrium film with a uniform thickness and a contact angle equal to zero ($\theta = 0$). For $0^\circ < \theta < 90^\circ$ the liquid partially wets the solid.

At equilibrium, the total interfacial free energy is a minimum, i.e.:

$$\sigma_{sl}A_{sl} + \sigma_{sv}A_{sv} + \sigma_{lv}A_{lv} = \text{minimum} \qquad (A.1)$$

where σ_{sv}, σ_{sl}, and σ_{lv} are the interfacial free energies of the solid-vapor, solid-liquid and liquid-vapor interfaces respectively and where A_{ij} are the areas. The solid-vapor interfacial free energy is used because the solid is in equilibrium with a vapor phase. The solid surface free energy is a function of the vapor pressure because the vapor can adsorb on the solid surface. Equation (A.1) can be used to describe the apparent contact angle formed by a liquid in contact with a solid substrate:

$$\sigma_{lv} \cos \theta = \sigma_{sv} - \sigma_{sl} \qquad (A.2)$$

The modifier apparent is used to remind us that we cannot see the real contact angle, which is of molecular dimensions, and that the

108

surface tensions were assumed constant in the derivation of Equation (A.2). Since the interfaces are boundaries between phases, large stress gradients are present in the contact line region. Therefore, the resulting interfacial free energies are a function of the local liquid film thickness. At the molecular level, the interfaces are dynamic with large anisotropic density gradients. In passing, it is noted that the internal pressure of a liquid can be of the order of a 1,000 atmospheres, whereas it approximately vanishes in the vapor at normal conditions. Obviously, the above equations are successful macroscopic models of the intermolecular force field. Equivalently, we can relate the wetting characteristics in terms of the final spreading coefficient, S, introduced by Cooper and Nuttal [54] :

$$S = \sigma_{sv} - \sigma_{sl} - \sigma_{lv} \qquad (A.3)$$

Thus the condition for complete wetting is $S = 0$; while the condition for partial wetting and nonwetting is $S < 0$.

A.1.2   Disjoining Pressure

Although the apparent contact angle, spreading coefficient and the surface tensions give considerable information concerning the general wetting characteristics of a system, the disjoining pressure concept, Π, outlined next is more useful. It allows fluid flow concepts in an ultra-thin film to be introduced and evaluated because it can be viewed as an effective pressure resulting from a body force acting between the substrate and the mobile liquid film [1,2]. A good review of the Hamaker constant and disjoining pressure is given in [50]. Briefly, the disjoining pressure is (minus) the potential energy per unit volume due to intermolecular forces, F, and is a function of the film thickness, δ:

$$\Pi\,(\delta) = -\,F\,(\delta) \qquad\qquad\qquad\qquad (A.4)$$

Disjoining describes the physical process whereby a completely spreading liquid naturally tends to disjoin a solid from the vapor by spreading. For completeness, an equivalent change in energy per unit surface area, E_s, with liquid film thickness could be given as:

$$\Pi = -\,dE_s/d\delta \qquad\qquad\qquad\qquad (A.5)$$

Therefore, for a completely wetting system, the "surface energy" decreases with an increase in the film thickness. This leads to a positive disjoining pressure, Π, and a negative potential energy, F.

For a completely spreading system, we discuss the case of a solid flat plate partially immersed at an angle θ in a pool of wetting fluid as shown in Figure 2.1. The presence of interfacial forces in the thin wetting film and capillary forces in the thicker film stabilizes it against the hydrostatic forces. Therefore, we see from hydrostatics that the pressure, F, in the liquid decreases with an increase in height. For a completely wetting system the adsorbed thin film can extend for a very long distance. The interfacial forces ($F(\delta)$) in the thin film start to become important at a thickness of approximately 10^{-7} m. The continuous film extends until it is a monolayer. At equilibrium, the chemical potential energy per unit volume in the thin flat film differs from that of a bulk liquid by an amount often referred to as the excess potential. Derjaguin has studied this potential energy experimentally and theoretically, and defined it in units of a pressure as the disjoining pressure. The Dzyaloshinskii-Lifshitz-Pitaevskii (DLP) theory enables one to calculate the force (per unit area), $F(\delta)$, from the film thickness, δ, and the optical and thermophysical properties of the solid, vapor, and the thin liquid film [2]. We note that although the DLP theory is

110

a powerful tool, extensive data on the optical properties as a function of frequency are needed. An expanded discussion of this material is given in Reference [36].

In the limit of a thin film (nonretarded regime, $\delta < 10$nm) one can represent the dispersion force as:

$$F(\delta) = A/ 6\pi\delta^3 = \frac{\bar{A}}{\delta^3}, \qquad (A.6)$$

while for the thicker regime (retarded regime, $\delta > 20$nm),

$$F(\delta) = B/ \delta^4 \qquad (A.7)$$

In Eq. (A.6), A is the well known Hamaker constant, while B is defined as the retarded dispersion force constant. For stable wetting films, both A and B must be negative. This implies that the potential energy of the system increases when the wetting film increases in thickness. In a horizontal film or under zero gravity conditions, fluid naturally flows from the thicker to the thinner region and a film of uniform thickness forms. Calculations of these forces indicate that the above two equations are simple approximations but as such are highly useful. The constants A and B are a weak function of thickness in their respective regimes [36].

The condition for equilibrium in the system presented in Figure 2.1 requires that the following form of the chemical potential (per unit volume) throughout the liquid be zero:

$$-F(\delta) + \sigma K - \rho g H = 0 \qquad (A.8)$$

where the three terms represent the contributions from the van der Waals force, the capillary force, and the hydrostatic force. The curvature of the film is represented by K, the density by ρ, and the gravitational force per unit mass by g. When we use only the

111

liquid-vapor interfacial free energy, σ_{lv}, we suppress the subscripts. The theoretical film profile obtained using Equation (A.8) can be compared to the measured equilibrium profile to determine the important interactive constant A or B. Therefore, a simple hydrostatic experiment can be done to determine the force field in a thin film. The hydrostatic term gives the pressure as a function of height and, therefore, the equation gives the profile as a function of pressure. We note that **both** A and σ are important. However, the use of the theoretically difficult liquid-solid and solid-vapor interfacial free energies has been replaced by the use of the Hamaker constant. In the adsorbed thin film above the curvature controlled region, the pressure can vary by a large amount because H can be very large. In an evaporating system H and δ decrease dramatically but the pressure is still a function of the thickness and shape. Therefore, large pressure gradients are possible in evaporating thin films with a change in shape which usually occurs over a very short distance.

Under zero gravity conditions, Equation (A.8) becomes:

$$-F(\delta) + \sigma K = \text{constant} \qquad (A.9)$$

Therefore, if an air or vapor bubble is present in a channel under zero gravity conditions, its shape can be predicted. In a _cylindrical_ channel, the bubble would be tubular with rounded ends and a surface film of liquid (if completely wetting) would form on the walls. The curvature at the ends would be approximately $K = 2/R$ where R is the radius of the tube if $\delta \ll R$. The film thickness could then be obtained from:

$$A/\ 6\pi\delta^3 \quad \text{or} \quad B/\delta^4 = -\sigma K \qquad (A.10)$$

112

At equilibrium, the adsorbed thin film would be relatively thick. For example, taking $R = 8.6 \times 10^{-4}$ m , $A = -6.9 \times 10^{-21}$ J, $\sigma = 2 \times 10^{-2}$ N/m , we find $\delta = 2 \times 10^{-8}$ m.

A.1.2   Evaluation of the Hamaker Constant

In the previous sections, the central importance of the Hamaker constant to the analysis of wetting, meniscus shape, and the heat sink characteristics of evaporating thin films have been discussed.   Fortunately, the Hamaker "constant" is a well known function of the film thickness and the optical properties of the liquid and substrate.   However, the necessary raw data on the optical properties are only well known for simple and ideal systems.   For example, the properties are well known for nonpolar simple fluids on quartz.   In addition there has been extensive discussions concerning water because of its importance even though it is an extremely complicated fluid.   Some data for other polar liquids like the alcohols exist.   This is extensively discussed in the literature review section (Section 2.1).

In general, the total disjoining pressure, $\Pi(\delta)$, in Equation (A.4) is the sum of a van der Waals component (Π_{vdw}), an electrostatic component based on charge (Π_{el}), and a structural component (Π_s). The van der Waals component is made up of Keesom energy (due to dipole-dipole interactions based on orientation), Debye energy (due to dipole - nonpolar interactions based on polarizability), and the London dispersion energy (due to electrodynamic interactions between the electrons in all atoms and molecules). The structural component is presumed negligible herein.

The substrate of primary importance herein is a single crystal of Silicon.   A surface oxide forms on the Silicon that protects it from

113

the environment, and the ideal Silicon substrate is really Silicon with a native surface oxide approximately 3 nm thick. Theoretically, it should be possible to start with intermolecular forces (as described by the optical properties of the materials) and calculate the Hamaker constant, the ideal heat transfer coefficient and the heat sink cf an evaporating ultra-thin film from first principles. However, the exact composition of the real experimental interface is unknown because it is a strong function of its history which is only approximately known because of possible interaction with water and other contaminants.. Therefore, although all the theoretical concepts are available for overall direction, experimental characterization of an "engineering" surface is still required. The experimental section demonstrates this characterization.

APPENDIX B: APPLICATION EXAMPLE

B.1 Application Example

In Figure (B.1), the profiles of two menisci located at the exit of a pore are presented. The pressure jump across the _base_ of the meniscus with the smaller radius of curvature is larger and, therefore, it would have the potential to draw more liquid to its interface. We take this to be the reference profile for an ideal evaporating meniscus: $\theta = 0$ for the completely wetting case. The following material analyzes the effect that fluid flow in the contact line region has on the pressure drop at the base of the meniscus. Briefly, viscous effects in the immediate vicinity of the interline would increase the effective (apparent) contact angle, θ_e, because the meniscus profile is a function of the pressure field that causes fluid flow in the meniscus.

The governing Equation (4.21) is used with the simplifying assumption that $\phi = - \eta^{-3}$ thereby neglecting the relative effect of curvature in the contact line region.

$$\frac{d}{d\xi} \left(\frac{1}{\eta} \frac{d\eta}{d\xi} \right) = \frac{1}{(1 + \kappa\eta)} \left(1 - \frac{1}{\eta^3} \right) \tag{B1}$$

The details of the impact of this assumption are discussed below. However, we note that applying this restriction in the contact line region does not effect the qualitative conclusions concerning the curvature at the base of the meniscus.

The boundary conditions of interest in this study are really a far-field condition. The thin film is a transition between a thicker body and a nonevaporating thin film (a film of thickness δ_0 at the
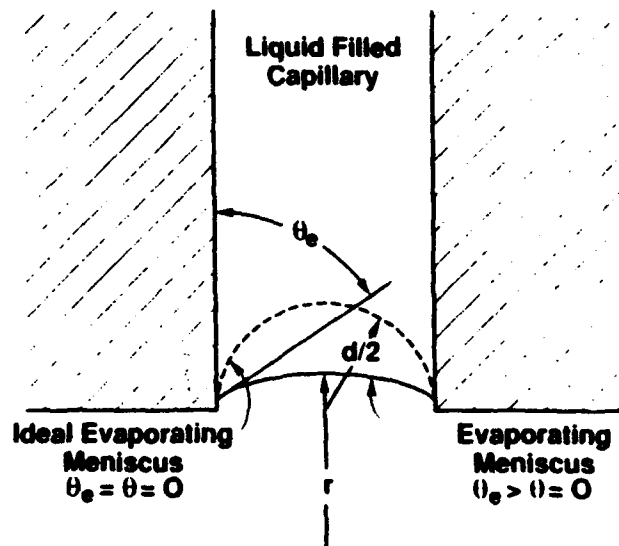
Figure B.1   Evaporating Meniscus Model Profile

contact line at the exit of the pore). Therefore the scaled thickness, η, satisfies the limit:

$$\eta \to 1$$

as:

$$\xi \to \infty.$$

Furthermore the slope satisfies the limit:

$$\frac{d\eta}{d\xi} \to 0$$

as:

$$\xi \to \infty.$$

The governing Equation (B1) is subjected to a transformation by defining the variable:

$$u = \eta^3 \tag{B2}$$

and find from Equation (B1) that:

$$\frac{1}{3} \frac{d}{d\xi} \left(\frac{1}{u} \frac{du}{d\xi} \right) = \frac{1}{1 + \kappa u^{1/3}} \left(1 - \frac{1}{u} \right) \tag{B3}$$

This equation is invariant with respect to translation in the independent variable ξ, therefore following Bluman and Cole [57] the transformation:

$$W = \frac{du}{d\xi} \tag{B4}$$

is used with the chain rule to eliminate ξ from the equation. The result is a first order differential equation which may be integrated. The proposed solution involves back transformation to replace u with η, and the inclusion of the far-field condition:

117

$$\frac{W}{u} = \left[18(1 + \kappa^3) \, ln \left(\frac{\eta}{1 + \kappa\eta}(1 + \kappa)\right) + 6(\eta^{-3} - 1)\right.$$

$$\left. + 9\kappa(1 - \eta^{-2}) + 18\kappa^2 (\eta^{-1} - 1)\right]^{1/2} \qquad (B5)$$

The solution is discussed in more depth in Section B.5. The integral heat sink for the contact line region, Q, is directly related to this quantity:

$$Q = \Gamma\Delta h_m = \frac{-\bar{A}\Delta h_m}{3\nu l} \cdot \frac{W}{u} \qquad (B6)$$

Therefore, $\frac{W}{u}$ is a dimensionless contact line heat sink, Q*:

$$Q^* \equiv \frac{W}{u} \qquad (B7)$$

B.2 Solution for Meniscus Profile and Heat Sink for Zero κ and Larger η

Equation (B5) represents a first order differential equation which we have integrated for a special case. The equation is simplified to obtain (B9) in that κ has been assumed to be zero (no insulation effects). It is further simplified by assuming that η is large. Specifically we assume:

$$\eta^{-3} \ll 1 \qquad (B8)$$

Then Equation (B5) becomes:

$$\frac{W}{u} = (18 \ln \eta - 6)^{1/2} \qquad (B9)$$

Solution of this is:

$$\eta = e^{1/3} e^{\xi^2/2} \qquad (B10a)$$

We find the film slope to be:

$$\frac{d\eta}{d\xi} = \frac{1}{3} \frac{W}{u} \exp\left(\frac{1}{18}\left(\frac{W}{u}\right)^2 + \frac{1}{3}\right)^2 \tag{B10b}$$

Equation (B1) was treated directly by a numerical method for zero κ by Wayner, et al. [9]. The use of the above result will be discussed more extensively in Section B.4.

B.3 Solution for Meniscus Profile and Heat Sink for Large κ

The meniscus profile might be found by integrating Equations (B4) and (B5). We propose an analytical solution valid for large κ. Analysis of both Equations (B5) and (B3) for the case of large values of κ yields:

$$\frac{1}{\eta} \frac{d\eta}{d\xi} = \kappa^{-1/2} \sqrt{2} \left(1 - \frac{1}{\eta} - \frac{1}{4}\left(1 - \frac{1}{\eta^4}\right)\right)^{1/2} \tag{B11}$$

Integration yields:

$$\frac{1}{\sqrt{3}} \ln\left(\eta + \frac{1}{3} + \sqrt{\left(\eta + \frac{1}{3}\right)^2 + \frac{2}{9}}\,\right)$$

$$- \frac{1}{\sqrt{6}} \ln\left(\frac{2\eta+1}{3\eta-3} + \sqrt{\left(\frac{2\eta+1}{3\eta-3}\right)^2 + \frac{1}{18}}\,\right)$$

$$= \frac{1}{\sqrt{2\kappa}} \xi \tag{B12}$$

In this case, the integral heat sink is:

$$Q = \frac{-\bar{A}\Delta h_m}{v l} \sqrt{\frac{2}{\kappa}} \left(1 - \frac{1}{\eta} - \frac{1}{4}\left(1 - \frac{1}{\eta^4}\right)\right)^{1/2} \tag{B13}$$

The maximum integral heat sink is the heat absorbed by the entire meniscus, Q_t. This is found from Equation (B13) with η "equal" infinity. In dimensional terms:

$$Q_t = \sqrt{\frac{3}{2}} \; (-\bar{A})^{1/3} \; \left(\frac{\Delta h_m \; k}{\nu}\right)^{1/2} \; \left(\frac{a}{b}\right)^{1/6} \Delta T^{2/3} \qquad (B14)$$

B.4 Discussion

The expression for the integral heat sink, Eq. (B6), implies that the slope and curvature of the film at some position along the substrate are functions of the amount of heat absorbed by the portion of the meniscus "downstream" of that position, or in other words the amount of material flowing past that position multiplied by the heat of vaporization. The expression for curvature is developed by expanding the left-hand side of Equation (B1) and using the expression for the integral heat sink which provides the slope of the film. That is:

$$\frac{1}{\eta} \frac{d^2\eta}{d\xi^2} - \frac{1}{\eta^2} \left(\frac{d\eta}{d\xi}\right)^2 = \frac{1}{1 + \kappa\eta} \left(1 - \frac{1}{\eta^3}\right) \qquad (B15)$$

The relationship between slope, curvature and the integral heat sink may be illustrated by a case study.

Consider the system of n-octane, silicon, and air. The temperature is 70°C and the temperature difference between the solid and vapor phases is $5.3(10^{-3})$°C. The constant $-\bar{A}$ is found from Truong and Wayner [36] as:

$$\bar{A} = -3.18 \; (10^{-21}) \; J \qquad (B16)$$

It is important to note that this is the value for an ideal system because these calculations were done before the experimental results were obtained in this research project. To put the following

120

results in perspective relative to the experimental portion, the value of ε is used. This demonstrates the importance of the parameter ε. For these temperatures and physical properties, the value of ε is 0.057. **Therefore, these conditions are substantially different from those that were experimentally studied.** Based on this information and the physical properties of bulk n-octane; the vapor pressure, P_v; the molar volume, V_l; the enthalpy of vaporization, Δh_m; and the kinematic viscosity, ν:

$$P_v = 119.03 \text{ torr}$$

$$V_l = 1.724 \ (10^{-4}) \ \text{m}^3/\text{mole}$$

$$\Delta h_m = 339.8 \ \text{kJ/kg}$$

$$\nu = 4.916 \ (10^{-7}) \ \text{m}^2/\text{s}$$

We find:

$$\delta_o = 45.08 \ \text{Å}$$

$$l = 1962 \ \text{Å} \tag{B17}$$

$$\kappa = 0.041$$

Figure B.2 provides a plot of $\dfrac{d\delta}{dx}$ and $\dfrac{d^2\delta}{dx^2}$ versus the integral heat sink Q, which is given by Equation (B6). Note the only factor in Q which is varied is the dimensionless film thickness η. This plot shows that the slope is steeper and the curvature larger in the portions of the meniscus which experience a greater flow. Curiously, these curves follow one another quite closely. The plot of curvature is important because capillarity is neglected in this analysis. Figure B.2 indicates that curvature increases with Q. Therefore this simple expression for the integral heat sink may be invalid for the larger

121
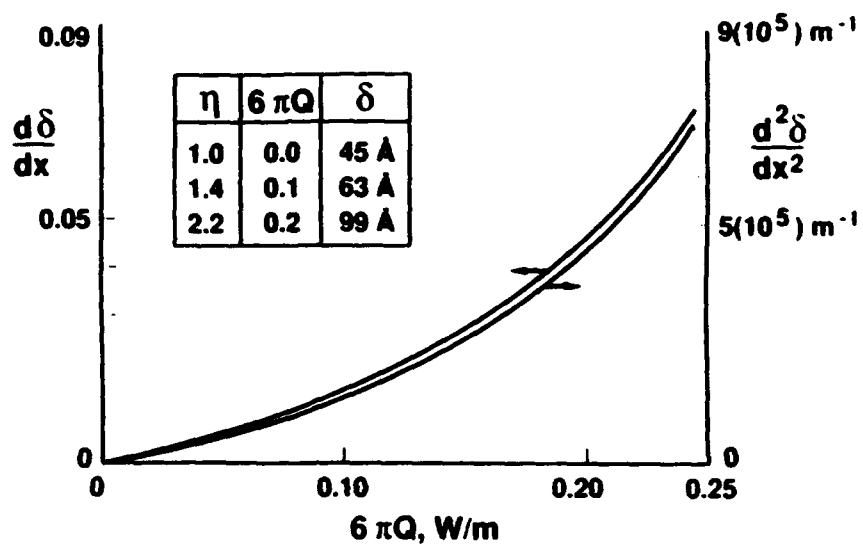
Figure B.2   Film Slope and Curvature as a Function of Heat Sink for a Particular Case.   Table provides corresponding film thicknesses.

values of Q. These values correspond to the thicker portions of the meniscus. The criteria for neglecting capillary pressure are:

$$\sigma \, \frac{d^2\delta}{dx^2} \ll -\frac{\bar{A}}{\delta^3}$$ (B18)

Taking the surface tension to be 16.87×10^{-3} N/m and using Equations (B5) and (B15) as well as the reference quantities, we estimate the disjoining pressure to be about 10 times larger than the capillary pressure at a thickness of $\eta = 1.25$. For convenience κ is set equal to zero. This corresponds to $Q^* = 1.04$ (or with $\Delta T = 4.5K$, $\delta_0 = 1$ nm, $Q^* = 1.98$). A more in depth treatment of capillary effects and the region of the meniscus over which they are negligible is beyond the scope of this report. We note that curvature in this example reaches $\delta'' = 700,000$ m^{-1} in the region where δ varies between 45Å and 126Å. This demonstrates how the curvature builds up near the contact line. Although the small scale of the analyzed region precludes quantitative comparison with experimental data at the present time, the results qualitatively agree with current experimental observations. The extrapolated use of the basic model evaluated at lower heat fluxes should be valid.

The heat flux, q, in the evaporating meniscus is of interest as well. This may be estimated with the ideal evaporation rate, $\dot{m}^{id}$:

$$q \sim \dot{m}^{id} \, \Delta h_m$$ (B19)

This is illustrated with more case studies. Case 1 corresponds to the conditions listed above, with varying temperature difference, ΔT. Case 2 is the n-octane-silicon-air system at 170°C. The higher temperature has a strong effect on the vapor pressure of n-octane. At 170°C it is very near 3 atm whereas at 70°C it is only 0.16 atm.

123

The ideal heat flux is plotted a ,ainst ΔT in Figure B.3. The flux is very high; however, it is not yet apparent how or if these fluxes may be realized. The effects of the various resistances are indicated in Equation (1.4) and are detailed in the main body of the report for lower heat fluxes. We find that, because the interfacial force field (represented by ϕ) lowers the vapor pressure and conduction in the liquid (represented by $\kappa\eta$) lowers the temperature at the liquid-vapor interface, the ideal heat flux based on kinetic theory and the solid-vapor interfacial temperature difference, ΔT, is greater than the maximum heat flux in the evaporating meniscus. Therefore, the results indicate that high interfacial mass (heat) fluxes can be obtained in small systems (small $\kappa\eta$) if they are stable. We note that stability should increase in small wetting systems because the relative importance of the solid substrate increases. However, this complex question has not been addressed and the experimental system was relatively large.

A dimensionless plot of the integral heat sink versus the film thickness, constructed from Equation (B5), is shown in Figure B.4 for four values of κ. This plot shows that the most active part of the meniscus is the thinnest part, especially for larger values of κ. Even though the heat flux decreases as $\eta \to 1$, the area is large because η' $\to 0$. Furthermore the resistance to heat transfer by the film is less in the thinnest part. This figure demonstrates the importance of κ. Although a parametric evaluation is required, we anticipate that κ should be relatively small for most systems.

The analysis may be related to the effective contact angle, θ_e, shown in Figure B.1, due to evaporation by constructing an engineering model of the evaporating thin film. The thin film is assumed to consist of two parts. The thinner part is governed by

124
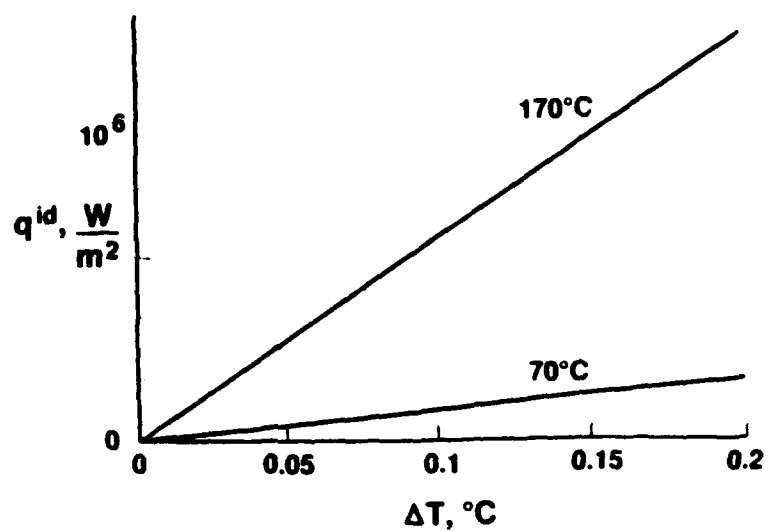
Figure B.3   Ideal Heat Flux Versus Solid to Vapor Temperature Change
at 70°C and 170°C.
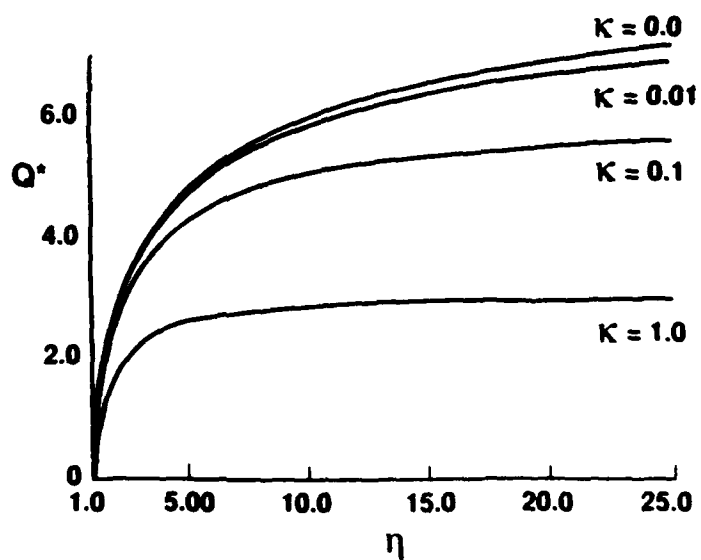
Figure B.4   Integral Heat Sink Versus Film Thickness for Several
Values of κ.

disjoining pressure and is analyzed in this paper. The thicker part is a capillary meniscus which has no appreciable pressure change. Although evaporation occurs in the complete meniscus, evaporation is assumed to occur only in the thinner part. Furthermore the thinner part of the film is taken to be so thin that insulation effects, $\kappa\eta$, are negligible. Therefore, the solution outlined in Equations (B7) through (B10) may be used. The two parts of the film meet smoothly so the slope of the capillary meniscus very near the solid is equal to the slope of the disjoining pressure film at η. This slope is related to the integral heat sink through Equation (B10). In this way, the effective contact angle, θ_e, is related to the integral heat sink. We expect a transition region between the capillary meniscus and the thinner part of the film in which both effects are important. We expect evaporation in this transition region and we expect the slope of the film to increase and so the relationship between the slope and the integral heat sink is approximate. Although we do not know the accuracy of the approximation, the additional insight gained is significant.

In particular, the effective contact angle, θ_e, is related to the dimensional slope through the inverse tangent:

$$\theta_e = \tan^{-1}\left(\frac{1}{3}\frac{\delta_o}{l}\frac{W}{u} \exp\left(\frac{1}{18}\left(\frac{W}{u}\right)^2 + \frac{1}{3}\right)\right) \qquad \text{(B20)}$$

According to this equation the effective contact angle increases with increases in the integral heat sink. The contact angle is relevant because it affects the radius of curvature of a meniscus in a circular pore. For a given pore the radius of curvature, r, is larger if the effective contact angle θ_e is larger. Specifically:

$$r = d/(2 \cos \theta_e) \qquad \text{(B21)}$$

where d is the diameter of the pore. In a passive cooling device the driving force for fluid flow is the Laplace pressure change at the meniscus. A larger value of r at the <u>base</u> of the meniscus due to a change in θ_e translates into a smaller driving force for flow. Therefore, a larger value of the integral heat sink may hinder the flow of liquid to the base of the meniscus and towards the interline from the base. We note the large slopes and curvatures presented in Figure B.2. These are due to viscous effects because the film analyzed would have been flat at equilibrium.

For large values of κ an analytical expression for the meniscus shape was developed. This is plotted in Figure B.5. Note that the independent variable is $\dfrac{\xi}{\sqrt{2\kappa}}$ In the numerical solution of Wayner, et al. the independent variable is ξ. Therefore, the effect of large resistance in the film (resistance to thermal conduction) is to stretch out the contact line region. A stronger effect induces more stretching.

For the limiting case of a <u>large κ value</u>, the maximum integral heat sink was found for a thin film. This is given in Equation (B14). The maximum integral heat sink is the total heat absorbed in the contact line region. In the derivation of Equation (B14) capillary effects were neglected. However, this expression may still be valid because, as previously discussed, the thinnest portions of the thin film are most active especially when film resistivity is large. It is the thinnest portions which have the least curvature. **On the other hand, we caution that large κ values might not be applicable to heat pipes and other high flux systems of interest.**
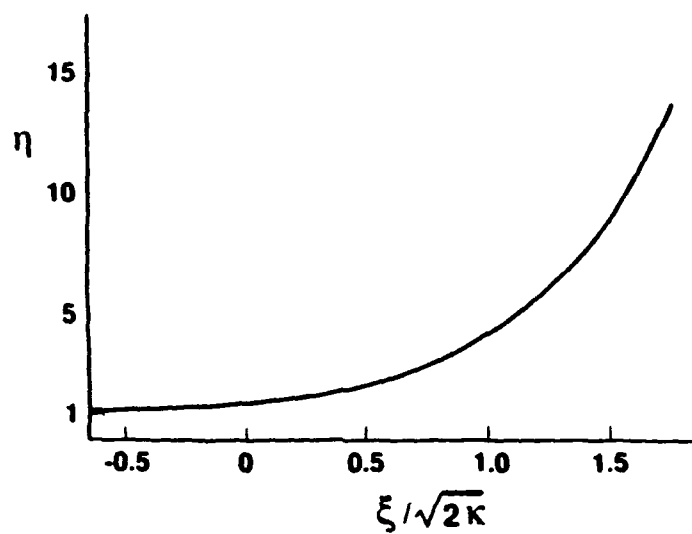
Figure B.5   Film Profile for Large κ (κ greater than 10, approximately).

The expression, Equation (B14), shows a reasonable dependence on parameters. Previous work has indicated that a large value of the Hamaker constant promotes evaporation, presumably because a stronger disjoining pressure pumps more liquid to the contact line region. A higher heat of vaporization Δh_m is correlated with improved performance. Thermal conductivity has a similar effect. This is not surprising since the resistance of the film to thermal conduction is assumed to be very important in the derivation of Equation (B14). Viscosity has a detrimental effect. Lubrication flow, a viscous flow, involves large pressure decreases which hinder evaporation. The parameter "a" indicates the magnitude of the response of evaporation to the degree of superheating. The parameter "b" indicates the propensity of the hindrance of evaporation due to the disjoining pressure. Therefore, the dependence of Q_t on a and b is plausible. Finally, we note that the elevation of the substrate temperature improves the total heat uptake. However, we do not expect the large κ solution to yield a high heat flux. For Case I, ΔT is 5.3 $(10^{-3})°C$ and κ is 0.041, κ is equal to 10 only if ΔT is 3.6 $(10^{-10})°C$. The choice of 10 is an estimate based on Equation (B31). Such a film would be quite thick, δ_o would be about 1 μm and the disjoining pressure would be virtually non-existent. In conclusion, parametric studies are obviously desirable using the equations experimentally evaluated herein.

B.5 DEVELOPMENT OF EQUATION (B5)

The governing equation (B1) is:

$$\frac{d}{d\xi}\left(\frac{1}{\eta}\frac{d\eta}{d\xi}\right) = \frac{1}{(1 + \kappa\eta)}\left(1 - \frac{1}{\eta^3}\right) \tag{B22}$$

The presence of the η^3 term suggests the transformation:

$$u = \eta^3 \qquad \text{(B23)}$$

This is only useful in the special case of κ equal to zero. The transformed equation is:

$$\frac{1}{3}\frac{d}{d\xi}\left(\frac{1}{u}\frac{du}{d\xi}\right) = \frac{1}{1 + \kappa u^{1/3}}\left(1 - \frac{1}{u}\right) \qquad \text{(B24)}$$

As mentioned in the text this is invariant with respect to translation in ξ, that is if we replace ξ with $\dot\xi$ such that:

$$\dot\xi = \xi - c \qquad \text{(B25)}$$

where c is some constant, the differential equation for $u(\dot\xi)$ is identical to (B24). Therefore following Bluman and Cole [57] we introduce the transformation:

$$W = \frac{du}{d\xi} \qquad \text{(B26)}$$

The chain rule implies:

$$\frac{d}{d\xi} = \frac{du}{d\xi}\frac{d}{du} = W\frac{d}{du} \qquad \text{(B27)}$$

Therefore, equation (B24) may be rewritten:

$$\frac{1}{3}W\frac{d}{du}\left(\frac{W}{u}\right) = \frac{1}{1 + \kappa u^{1/3}}\left(1 - \frac{1}{u}\right) \qquad \text{(B28)}$$

or:

$$\frac{1}{3}\frac{W}{u}\frac{d}{du}\left(\frac{W}{u}\right) = \frac{1}{1 + \kappa u^{1/3}}\left(1 - \frac{1}{u}\right)\frac{1}{u} \qquad \text{(B29)}$$

This may be integrated to yield:

$$\frac{1}{6}\left(\frac{W}{u}\right)^2 = \int \frac{1}{1 + \kappa u^{1/3}}\left(1 - \frac{1}{u}\right)\frac{1}{u}\,du \qquad \text{(B30)}$$

130

The integral is simpler if u is eliminated in favor of η with equation (B23). We find:

$$\frac{1}{18}\left(\frac{W}{u}\right)^2 = \int \frac{d\eta}{\eta(1 + \kappa\eta)} - \int \frac{d\eta}{\eta^4(1 + \kappa\eta)} \qquad (B31)$$

The integrals were solved by the method of "partial fractions" for the expression (B5). The far-field condition implies that:

$$\frac{W}{u} \to 0 \qquad (B30)$$

as:

$$\eta \to 1 \qquad (B31)$$

This fixes the constant of integration.

APPENDIX C

C.1 Computer Program

The programs used to generate the numerical results corresponding to the theory discussed in Section 4 of the report are listed in this appendix. The NAG (Numerical Algorithms Group) routine is not listed, of course. The code consists of a main program, shown in C.2; a subroutine which calls the NAG routine, shown in C.3: and two subroutines called by the NAG routine, one of which prepares output, while the other calculates derivatives.

The main program reads the experimental data which can be shipped to a plotting routine through a common block, after minor alterations for convenience. The alterations involve reversing the direction of the independent variable (position along the substrate) to match the convention of the numerical solution, chopping away a portion of the flat end of the meniscus (except for some occasional noise the flat end is strictly flat), and translating the data to reduce the variation between data and theory. Reversal of the direction of the independent variable and translation of the data are justified by the nature of the governing equations. The dependent variable λ does not appear and all terms have an even number of differentiations relative to λ.

The main program also calls subroutine THEOR1 and can call a plotting routine if desired.

Subroutine THEOR1 calculates the initial conditions as discussed in Section 4 (note the direction of the independent variable is reversed), and calls NAG routine DO2CBF which is reported to employ Adam's method. Also shown is subroutine FCN,

called by the NAG routine, which calculates the derivatives of the state variables from the state variables $U(1)$, ... $U(4)$ used by the NAG routine. The state variables are defined to be η, $-\dfrac{d\eta}{d\lambda}$, ϕ, and $-\dfrac{d\phi}{d\lambda}$, in terms of Section 4.

Different versions of subroutine "output" are shown in C.4 and C.5. Each of these versions is used by the NAG routine to record the values of the state variables at particular locations. The different versions may calculate various derived quantities, such as the dimensionless curvature.

C.2

```
C       Dec. 17, 1990    Jeff Schonberg
C
C       Comparison of Theory and Sunando's Data
C
C       Version 1
C
C       The theory comes from file ADAMS1. The data is read
C       from Sunando's output file.
C
        REAL*8 EPS,KAP,XEND,TOL,A,B,XNOT,DELREF,XREF,XTRANS
        REAL*8 X(400),D(400),XR(400),DR(400),PX(400),PD(400),TX(400),TH(400)
        EXTERNAL THEOR1
        EXTERNAL PLOT1
        EXTERNAL FCN,OUTPUT
        INTEGER NDATA,I,J,IBEG,IEND,NPLOT,NPTS
        COMMON/DERVS/EPS,KAP
        COMMON/DIFFEQ/XEND,TOL,A,B,XNOT,NPTS
        COMMON/ART/DELREF,XREF,TX,TH
        COMMON/PARM/XTRANS
C
        READ(5,10) NDATA
10      FORMAT(I4)
        DO 20 I=1,NDATA
           READ(4,30) X(I),D(I)
30         FORMAT(E12.6,2X,E12.6)
20      CONTINUE
        DO 35 I=1,NDATA
           J= NDATA -I + 1
           XR(J) = X(NDATA) - X(I)
           DR(J) = D(I)
35      CONTINUE
        READ(5,40) IBEG,IEND
40      FORMAT(2I4)
        NPLOT= IEND - IBEG + 1
C
        READ(5,60) XTRANS
        DO 50 I=IBEG,IEND
           J= I + 1 - IBEG
           PX(J) = XR(I) + XTRANS
           PD(J) = DR(I)
50      CONTINUE
60      FORMAT(E13.6)
C       DO 70 J=IBEG,IEND
C          PX(J) = PX(J) + XTRANS
C70     CONTINUE
C
        READ(5,80) EPS,KAP,XEND,TOL
        READ(5,90) A,B,XNOT
        READ(5,100) DELREF,XREF
C       So I dont have to recalculate XREF when I vary EPS do it in
C       the program.
        XREF=XREF*DSQRT(EPS)
80      FORMAT(4E13.6)
90      FORMAT(3E13.6)
100     FORMAT(2E13.6)
        READ(5,110) NPTS
110     FORMAT(I3)
C
        WRITE(6,125) EPS
125     FORMAT(' CAPILLARITY PAR EPS  =',E15.6/)
        WRITE(6,126) KAP
126     FORMAT(' RESISTIVITY PAR KAP  =',E15.6/)
        WRITE(6,130)
130     FORMAT(' ',10X,' **** RESULTS ****'//
     &' ','X',15X,'U(1)',15X,'U(2)',15X,'U(3)',15X,'U(4)'//
     &' ','REAL X',13X,' H',17X,'DHDX',15X,' P',17X,'DPDX'/)
        WRITE(6,132) TOL
132     FORMAT(' ','   TOL =',E15.6/)
        WRITE(6,140) A,B,XNOT
140     FORMAT(' ',' A =',E13.6,' B=',E13.6,' XNOT=',E13.6//)
        CALL THEOR1
        CALL PLOT1(PX,PD,NPLOT)
        STOP
        END
```

134

```
C     Dec. 18, 1990      Jeff   Schonberg
C
C
C     Subroutine to solve extended Kao problem
C
C     ( h.h.h p' )' = 3 eps ( 1 + p )/( 1 + k.h )
C
C                 p = -1/(h.h.h) - h''
C
C     The algorithm uses Adam's method.
C
      SUBROUTINE THEOR1
      REAL*8 X,XEND,TOL,U(4),EPS,KAP,DX,W(110),XNOT
      REAL*8 A,B
      REAL*8 DUM1
      COMMON/DERVS/EPS,KAP
      COMMON/DIFFEQ/XEND,TOL,A,B,XNOT,NPTS
      EXTERNAL FCN,OUTPUT
C
      COMMON/OUT/DX,I
C
C
C     Now we try to compute the initial conditions.
C
      DUM1=DSQRT(EPS/( KAP + 1 ))
      U(1)= 1.0 + A*DEXP(XNOT*DUM1*3.**.5) + B*DEXP(XNOT*3.**.5)
      U(2)=   A*DUM1*(3.**.5)*DEXP(XNOT*DUM1*3.**.5)
     &+ B*(3.**.5)*DEXP(XNOT*3.**.5)
      U(3)= -1.0 + 3.0*( 1.0 - DUM1**2 )*A*DEXP(XNOT*DUM1*3.**.5)
      U(4)= 3.0*( 1.0 - DUM1**2 )*A*DEXP(XNOT*DUM1*3.**.5)*(3.**.5)*DUM1
C
C
      X=0.
      N=4
      IRELAB=1
      IFAIL=0
C
      DX=( XEND  )/( NPTS - 1 )
      I = 1
C
      CALL D02CBF(X,XEND,N,U,TOL,IRELAB,FCN,OUTPUT,
     & W,IFAIL)
C
      RETURN
      END
      END
C
C
C
      SUBROUTINE FCN(T,U,F)
      REAL*8 T,U(4),F(4),EPS,KAP
      COMMON/DERVS/EPS,KAP
C
      F(1)=U(2)
      F(2)= -( U(1)**(-3) ) - U(3)
      F(3)=U(4)
      F(4)=EPS*3.0*( 1. + U(3) )*( U(1)**(-3) )/( 1. + KAP*U(1) )
     & -3.0*U(2)*U(4)/U(1)
      RETURN
      END
      SUBROUTINE OUTPUT(XSOL,U)
      REAL*8 XSOL,U(4),DX,X
      REAL*8 DELREF,XREF,TX(400),TH(400)
      COMMON/ART/DELREF,XREF,TX,TH
      COMMON/OUT/DX,I
      WRITE(6,10) XSOL,U(1),U(2),U(3),U(4)
      TX(I)=XREF*XSOL
      TH(I)=DELREF*U(1)
C      WRITE(7,20) TX(I),TH(I)
20    FORMAT(' ','TX= ',E13.6,'TH= ',E13.6)
      XSOL=    DX*I
      I=I+1
10    FORMAT(' ',E13.6,E16.6,3E19.6/)
      DEL=0.9
      IF(U(1).LT.DEL) STOP
      RETURN
      END
```

135

C.4

```
        SUBROUTINE OUTPUT(XSOL,U)
        REAL*8 XSOL,U(4),DX,X
        REAL*8 KURV,FLUX,KAP,EPS
        REAL*8 DELREF,XREF,TX(400),TH(400)
        COMMON/ART/DELREF,XREF,TX,TH
        COMMON/OUT/DX,I
        COMMON/DERVS/EPS,KAP
        WRITE(6,10) XSOL,U(1),U(2),U(3),U(4)
C   TRY TO FIND CURVATURE, AND FLUX AND WRITE THEM OUT
C   TO A DATA FILE TO BE USED BY A PLOTTING ROUTINE.
C
        KURV= -U(3) - 1./ U(1)**3
        FLUX= ( 1. + U(3) )/(1. + KAP*U(1) )
        WRITE(8,30) U(1),U(3),KURV,FLUX
   30   FORMAT(' ',4E15.6/)
C
        TX(I)=XREF*XSOL
        TH(I)=DELREF*U(1)
C       WRITE(7,20) TX(I),TH(I)
   20   FORMAT(' ','TX= ',E13.6,'TH= ',E13.6)
        XSOL=    DX*I
        I=I+1
   10   FORMAT(' ',E13.6,E16.6,3E19.6/)
        DEL=0.9
        IF(U(1).LT.DEL) STOP
        RETURN
        END
```

C.5

```
        SUBROUTINE OUTPUT(XSOL,U)
        REAL*8 XSOL,U(4),DX,X,GAM
        REAL*8 DELREF,XREF,TX(400),TH(400)
        COMMON/ART/DELREF,XREF,TX,TH
        COMMON/OUT/DX,I
C
C
C       We need to get hhh*dpdx .
C
        GAM=( U(1)**3 ) * U(4)
        WRITE(6,10) XSOL,U(1),U(2),U(3),U(4),GAM
        TX(I)=XREF*XSOL
        TH(I)=DELREF*U(1)
C       WRITE(7,20) TX(I),TH(I)
   20   FORMAT(' ','TX= ',E13.6,'TH= ',E13.6)
        XSOL=    DX*I
        I=I+1
   10   FORMAT(' ',E13.6,E16.6,4E19.6/)
        DEL=0.9
        IF(U(1).LT.DEL) STOP
        RETURN
        END
```